The Astrophysical Journal, 989:110 (39pp), 2025 August 10 https://doi.org/10.3847/1538-4357/ade8f0
© 2025. The Author(s). Published by the American Astronomical Society.
OPEN ACCESS

A Systematic Search for MeV–GeV Pulsar Wind Nebulae without Gamma-Ray Detected Pulsars

The Fermi-LAT Collaboration,
A. Acharyya[1], A. Adelfio[2], M. Ajello[3], L. Baldini[4], J. Ballet[5], C. Bartolini[6,7], J. Becerra Gonzalez[8], R. Bellazzini[9], E. Bissaldi[10,6], R. Bonino[11,12], P. Bruel[13], R. A. Cameron[14], P. A. Caraveo[15], F. Casaburo[16,17,18], F. Casini[19], D. Castro[20,21], E. Cavazzuti[22], S. Ciprini[16,17], G. Cozzolongo[23,24], P. Cristarella Orestano[2,19], F. Cuna[6], S. Cutini[2], F. D'Ammando[25], D. Depalo[6], N. Di Lalla[14], A. Dinesh[26], L. Di Venere[6], A. Domínguez[26], J. Eagle[21,27,28], A. Fiori[4], Y. Fukazawa[29], S. Funk[23], P. Fusco[6,10], F. Gargano[6], C. Gasbarra[16,30], D. Gasparrini[16,17], S. Germani[2,31], F. Giacchino[16,17], N. Giglietto[6,10], M. Giliberti[6,10], F. Giordano[6,10], M. Giroletti[25], D. Green[32], I. A. Grenier[33], M.-H. Grondin[34], S. Guiriec[21,35], R. Gupta[21], A. K. Harding[36], M. Hashizume[29], E. Hays[21], J. W. Hewitt[37], D. Horan[13], X. Hou[38], T. Kayanoki[29], M. Kuss[9], A. Laviron[13], M. Lemoine-Goumard[34], A. Liguori[6], J. Li[39,40], I. Liodakis[41], P. Loizzo[6,7], F. Longo[42,43], F. Loparco[6,10], L. Lorusso[6,10], M. N. Lovellette[44], P. Lubrano[2], S. Maldera[11], D. Malyshev[23], G. Martí-Devesa[42], M. N. Mazziotta[6], I. Mereu[2,19], P. F. Michelson[14], N. Mirabal[21,45], T. Mizuno[46], P. Monti-Guarnieri[42,43], M. E. Monzani[14,47], A. Morselli[16], I. V. Moskalenko[14], N. Omodei[14], E. Orlando[14,48], D. Paneque[32], G. Panzarini[6,10], M. Persic[43,49], M. Pesce-Rollins[9], R. Pillera[6,10], T. A. Porter[14], G. Principe[42,50], S. Rainò[6,10], R. Rando[51,52,53], M. Razzano[4], A. Reimer[54], O. Reimer[54], M. Sánchez-Conde[55,56], P. M. Saz Parkinson[57], D. Serini[6], C. Sgrò[9], E. J. Siskind[58], G. Spandre[9], P. Spinelli[6,10], A. W. Strong[59], H. Tajima[60,61], J. B. Thayer[14], L. Tibaldo[62], D. F. Torres[63,64,65], J. Valverde[21,45], K. Wood[66], G. Zaharijas[67], and W. Zhang[63,65]
[1] Center for Cosmology and Particle Physics Phenomenology, University of Southern Denmark, Campusvej 55, DK-5230 Odense M, Denmark
[2] Istituto Nazionale di Fisica Nucleare, Sezione di Perugia, I-06123 Perugia, Italy
[3] Department of Physics and Astronomy, Clemson University, Kinard Lab of Physics, Clemson, SC 29634-0978, USA
[4] Università di Pisa and Istituto Nazionale di Fisica Nucleare, Sezione di Pisa I-56127 Pisa, Italy
[5] Université Paris-Saclay, Université Paris Cité, CEA, CNRS, AIM, F-91191 Gif-sur-Yvette Cedex, France; jean.ballet@cea.fr
[6] Istituto Nazionale di Fisica Nucleare, Sezione di Bari, I-70126 Bari, Italy
[7] Università degli studi di Trento, via Calepina 14, 38122 Trento, Italy
[8] Instituto de Astrofísica de Canarias and Universidad de La Laguna, Dpto. Astrofísica, 38200 La Laguna, Tenerife, Spain
[9] Istituto Nazionale di Fisica Nucleare, Sezione di Pisa, I-56127 Pisa, Italy
[10] Dipartimento di Fisica "M. Merlin" dell'Università e del Politecnico di Bari, via Amendola 173, I-70126 Bari, Italy
[11] Istituto Nazionale di Fisica Nucleare, Sezione di Torino, I-10125 Torino, Italy
[12] Dipartimento di Fisica, Università degli Studi di Torino, I-10125 Torino, Italy
[13] Laboratoire Leprince-Ringuet, CNRS/IN2P3, École polytechnique, Institut Polytechnique de Paris, 91120 Palaiseau, France
[14] W. W. Hansen Experimental Physics Laboratory, Kavli Institute for Particle Astrophysics and Cosmology, Department of Physics and SLAC National Accelerator Laboratory, Stanford University, Stanford, CA 94305, USA
[15] INAF-Istituto di Astrofisica Spaziale e Fisica Cosmica Milano, via E. Bassini 15, I-20133 Milano, Italy
[16] Istituto Nazionale di Fisica Nucleare, Sezione di Roma "Tor Vergata," I-00133 Roma, Italy
[17] Space Science Data Center—Agenzia Spaziale Italiana, Via del Politecnico, snc, I-00133, Roma, Italy
[18] Dipartimento di Fisica, Università La Sapienza, Piazzale A. Moro, 2, I-00185 Roma, Italy
[19] Dipartimento di Fisica, Università degli Studi di Perugia, I-06123 Perugia, Italy
[20] Harvard-Smithsonian Center for Astrophysics, Cambridge, MA 02138, USA; daniel.castro@cfa.harvard.edu
[21] Astrophysics Science Division, NASA Goddard Space Flight Center, Greenbelt, MD 20771, USA; jordan.l.eagle@nasa.gov
[22] Italian Space Agency, Via del Politecnico snc, 00133 Roma, Italy
[23] Friedrich-Alexander Universität Erlangen-Nürnberg, Erlangen Centre for Astroparticle Physics, Erwin-Rommel-Str. 1, 91058 Erlangen, Germany
[24] Friedrich-Alexander-Universität, Erlangen-Nürnberg, Schlossplatz 4, 91054 Erlangen, Germany
[25] INAF Istituto di Radioastronomia, I-40129 Bologna, Italy
[26] Grupo de Altas Energías, Universidad Complutense de Madrid, E-28040 Madrid, Spain
[27] Department of Physics & Astronomy, Clemson University, Clemson, SC 29634, USA
[28] Harvard & Smithsonian—Center for Astrophysics, Cambridge, MA 02138, USA
[29] Department of Physical Sciences, Hiroshima University, Higashi-Hiroshima, Hiroshima 739-8526, Japan
[30] Dipartimento di Fisica, Università di Roma "Tor Vergata," I-00133 Roma, Italy
[31] Dipartimento di Fisica e Geologia, Università degli Studi di Perugia, via Pascoli snc, I-06123 Perugia, Italy
[32] Max-Planck-Institut für Physik, D-80805 München, Germany
[33] Université Paris Cité, Université Paris-Saclay, CEA, CNRS, AIM, F-91191 Gif-sur-Yvette, France
[34] Université Bordeaux, CNRS, LP2I Bordeaux, UMR 5797, F-33170 Gradignan, France
[35] The George Washington University, Department of Physics, 725 21st Street, NW, Washington, DC 20052, USA
[36] Los Alamos National Laboratory, Los Alamos, NM 87545, USA
[37] University of North Florida, Department of Physics, 1 UNF Drive, Jacksonville, FL 32224, USA
[38] Yunnan Observatories, Chinese Academy of Sciences, Kunming 650216, People's Republic of China
[39] CAS Key Laboratory for Research in Galaxies and Cosmology, Department of Astronomy, University of Science and Technology of China, Hefei 230026, People's Republic of China
[40] School of Astronomy and Space Science, University of Science and Technology of China, Hefei 230026, People's Republic of China
[41] NASA Marshall Space Flight Center, Huntsville, AL 35812, USA
[42] Dipartimento di Fisica, Università di Trieste, I-34127 Trieste, Italy
[43] Istituto Nazionale di Fisica Nucleare, Sezione di Trieste, I-34127 Trieste, Italy
[44] The Aerospace Corporation, 14745 Lee Road, Chantilly, VA 20151, USA
[45] Center for Space Science and Technology, University of Maryland Baltimore County, 1000 Hilltop Circle, Baltimore, MD 21250, USA

[46] Hiroshima Astrophysical Science Center, Hiroshima University, Higashi-Hiroshima, Hiroshima 739-8526, Japan
[47] Vatican Observatory, Castel Gandolfo, V-00120, Vatican City State
[48] Istituto Nazionale di Fisica Nucleare, Sezione di Trieste, and Università di Trieste, I-34127 Trieste, Italy
[49] INAF-Astronomical Observatory of Padova, Vicolo dell'Osservatorio 5, I-35122 Padova, Italy
[50] INAF Istituto di Radioastronomia, Via P. Gobetti, 101, I-40129 Bologna, Italy
[51] Dipartimento di Fisica e Astronomia "G. Galilei," Università di Padova, Via F. Marzolo, 8, I-35131 Padova, Italy
[52] Istituto Nazionale di Fisica Nucleare, Sezione di Padova, I-35131 Padova, Italy
[53] Center for Space Studies and Activities "G. Colombo," University of Padova, Via Venezia 15, I-35131 Padova, Italy
[54] Institut für Astro- und Teilchenphysik, Leopold-Franzens-Universität Innsbruck, A-6020 Innsbruck, Austria
[55] Instituto de Física Teórica UAM/CSIC, Universidad Autónoma de Madrid, E-28049 Madrid, Spain
[56] Departamento de Física Teórica, Universidad Autónoma de Madrid, 28049 Madrid, Spain
[57] Santa Cruz Institute for Particle Physics, Department of Physics and Department of Astronomy and Astrophysics, University of California at Santa Cruz, Santa Cruz, CA 95064, USA
[58] NYCB Real-Time Computing Inc., Lattingtown, NY 11560-1025, USA
[59] Max-Planck Institut für extraterrestrische Physik, D-85748 Garching, Germany
[60] Nagoya University, Institute for Space-Earth Environmental Research, Furo-cho, Chikusa-ku, Nagoya 464-8601, Japan
[61] Kobayashi-Maskawa Institute for the Origin of Particles and the Universe, Nagoya University, Furo-cho, Chikusa-ku, Nagoya, Japan
[62] IRAP, Université de Toulouse, CNRS, UPS, CNES, F-31028 Toulouse, France
[63] Institute of Space Sciences (ICE, CSIC), Campus UAB, Carrer de Magrans s/n, E-08193 Barcelona, Spain; dtorres@ice.csic.es, zhang@ice.csic.es
[64] Institució Catalana de Recerca i Estudis Avançats (ICREA), E-08010 Barcelona, Spain
[65] Institut d'Estudis Espacials de Catalunya (IEEC), E-08034 Barcelona, Spain
[66] Praxis Inc., Alexandria, VA 22303, Resident at Naval Research Laboratory, Washington, DC 20375, USA
[67] Center for Astrophysics and Cosmology, University of Nova Gorica, Nova Gorica, Slovenia
Received 2025 April 4; revised 2025 June 5; accepted 2025 June 18; published 2025 August 7

Abstract

An increasing number of pulsar wind nebulae (PWNe) are being identified in the TeV band by ground-based Imaging Air Cherenkov Telescopes such that they constitute the dominant source class of Galactic TeV emitters. However, MeV–GeV PWN counterparts are still largely lacking. To date, only a dozen PWNe are identified by the Fermi–Large Area Telescope (LAT) in the MeV–GeV band. Most PWNe are located along the Galactic plane embedded within the prominent, diffuse Galactic γ-ray emission, which makes these sources difficult to disentangle from the bright diffuse background. We present a systematic search for γ-ray counterparts to known PWNe in the 300 MeV–2 TeV energy band using the Fermi–LAT. We target the locations of previously identified PWNe that lack detected Fermi–LAT pulsars to minimize associated pulsar contamination. The sample includes six previously identified Fermi PWNe and eight Fermi–LAT sources associated with PWNe. We report the analysis of 58 regions of interest and classify Fermi–LAT detected sources as either a likely PWN or a candidate PWN counterpart based on their morphological and spectral characteristics across the broadband spectrum. There are nine unidentified Fermi–LAT sources that we consider as likely PWN counterparts, which, if confirmed to be PWNe, would greatly increase the PWN population detected by the Fermi–LAT from 12 to 21. The remaining Fermi–LAT detected sources are considered weaker PWN candidates. A second approach in the systematic search for γ-ray emitting PWNe will involve studying the off-pulse phases of Fermi–LAT detected pulsars for the presence of an obscured PWN and will be reported in a subsequent paper.

Unified Astronomy Thesaurus concepts: Gamma-ray astronomy (628); Pulsar wind nebulae (2215); High energy astrophysics (739); Core-collapse supernovae (304)

Materials only available in the online version of record: figure set

1. Introduction

A pulsar wind nebula (PWN) is composed of a highly magnetized, relativistic plasma powered by an energetic, rapidly rotating neutron star descending from a core collapse supernova (CC SN). The neutron star loses angular momentum as rotational energy is converted to a relativistic particle wind made up of mostly electrons and positrons. Particles are injected by the central pulsar and accelerated at the termination shock, where the ram pressure of the cold pulsar wind is balanced by the pressure of the relativistic plasma. Altogether, the nebula is confined by the surrounding supernova (SN) ejecta (e.g., M. J. Rees & J. E. Gunn 1974; C. F. Kennel & F. V. Coroniti 1984). Synchrotron emission from the relativistic leptons is observed from the majority of PWNe, from radio wavelengths to hard X-rays, while the same leptons scatter off local photon fields, resulting in Inverse Compton (IC) emission at γ-ray energies.

A PWN evolves together with its host supernova remnant (SNR) and is influenced by the properties of the central pulsar, the SNR, and the structure of the surrounding interstellar medium (ISM; B. M. Gaensler & P. O. Slane 2006). A variety of both magnetohydrodynamical and semianalytic radiative evolutionary models have been developed to explore the PWN evolution inside a nonradiative SNR (see, e.g., J. M. Blondin et al. 2001; E. van der Swaluw et al. 2004; J. D. Gelfand et al. 2009; J. Martín et al. 2012; R. Bandiera et al. 2023b). Constraining the physical properties of the particles is difficult, requiring a combination of simulation tools and observable properties over the entire electromagnetic spectrum. MeV–GeV measurements are therefore critical for characterizing accurately the particle spectrum at injection and its consequent evolution. Further, evolutionary studies of PWNe indicate that the γ-ray luminosity increases with time, suggesting that many evolved PWNe may be emitting brightly in the Fermi–Large Area Telescope (LAT) band. Indeed,

Original content from this work may be used under the terms of the Creative Commons Attribution 4.0 licence. Any further distribution of this work must maintain attribution to the author(s) and the title of the work, journal citation and DOI.

so far we have seen that several identified Fermi–LAT PWNe are old ($\tau \gtrsim 5$ kyr; see, e.g., H. E. S. S. Collaboration et al. 2012a; J. Devin et al. 2018; G. Principe et al. 2020).

The termination shock of the PWN is a potential site for efficient particle acceleration. As such, PWNe provide unique laboratories to study relativistic particle acceleration processes and the required environmental conditions, especially during the PWN interaction with its surroundings. Understanding the PWN population and the interactions that take place are crucial for identifying how the relativistic particles rejoin the ISM, how they contribute to replenishing the electron Galactic cosmic-ray (CR) population (M. Renaud 2009; O. Kargaltsev et al. 2013), and whether they are responsible for local enhancements in the $e^- e^+$ flux (D. Malyshev et al. 2009).

Historically, PWNe like the Crab were discovered in droves in the radio ($\gtrsim$30) and X-ray ($\gtrsim$60) wavelengths, and now γ-rays are becoming key to finding and characterizing PWNe (O. Kargaltsev et al. 2013; D. A. Green 2019). The H.E.S.S. Galactic Plane Survey (H. E. S. S. Collaboration et al. 2018) has been particularly impactful toward TeV PWN discovery, as well as earlier MAGIC and VERITAS observations, all of which are included in the TeVCat[68] ($\sim$36 listed as PWNe; S. P. Wakely & D. Horan 2008). Most recently, the LHAASO catalog reported 90 $E > 1$ TeV sources, 43 of them also detected as ultra-high-energy ($E > 100$ TeV), and many of them classified as PWNe or candidate PWNe (Z. Cao et al. 2024). The observed TeV γ-ray spectra from many of these sources indicate that the energy peak occurs in the MeV–GeV band, where the Fermi–LAT provides the best sensitivity and sky coverage. MeV–GeV observations are also effective in detecting PWNe that may peak in the γ-ray band, but appear faint in other wavelengths (e.g., M. Ackermann et al. 2011).

M. Ackermann et al. (2011) analyzed the off-pulse emission of 54 Fermi–LAT detected pulsars for $E > 100$ MeV and detected two PWNe: the Crab and Vela–X. The 2FGL catalog (P. L. Nolan et al. 2012) detected two more Fermi–LAT PWNe, and the second pulsar catalog (A. A. Abdo et al. 2013) reported the detection of PWN 3C 58, which is later characterized in detail by J. Li et al. (2018). Several PWNe with no associated γ-ray bright pulsar have been identified by the Fermi–LAT through spatial coincidence using observations in other wavelengths. An analysis was conducted in 58 regions around TeV PWNe and unidentified TeV sources within 5° of the Galactic plane using 45 months of Fermi–LAT data (F. Acero et al. 2013b) that resulted in the detection of 30 Fermi–LAT sources, three of which were clearly identified as PWNe and 11 as PWN candidates. The latest comprehensive Fermi–LAT source catalog, 4FGL (data release 4, DR4; J. Ballet et al. 2023) currently lists a total of 12 firm PWNe and nine PWN associations.

We expand the Fermi–LAT PWN search effort by analyzing 138 months of Fermi–LAT data in the direction of PWNe identified in radio, X-ray, GeV, and TeV observations. The systematic search reported here targets the locations of 58 PWNe and PWN candidates that lack an associated γ-ray detected pulsar (Section 2; see also D. A. Smith et al. 2023). The sample construction comprising the 58 regions of interest (ROIs) is described in the following section (Section 2). In Section 3, we describe the Fermi–LAT data selection, reduction, and analysis. In Section 4, we report the results of the 58 analyzed ROIs with detailed discussions. We provide an overview of the results and implications in Section 5 and conclude in Section 6.

[68] tevcat.uchicago.edu

2. Source Selection

There are $\sim$125 PWNe and PWN candidates[69] that have been discovered from radio to TeV γ-rays, the majority of which were first identified in radio or X-ray surveys[70] (G. Ferrand & S. Safi-Harb 2012) with an increasing number of discoveries in the TeV band. Indeed, the majority of the TeV Galactic source population is found to originate from PWNe as observed by Imaging Air Cherenkov Telescopes (H. E. S. S. Collaboration et al. 2018). However, Fermi–LAT PWN counterparts are still lacking even after 15 yr of observing the entire sky every 3 hr, with only 21 PWNe currently noted as associated with sources in the comprehensive 4FGL-DR4 catalog. (J. Ballet et al. 2023). Twelve are extended sources considered firm PWN associations, three are extended sources coincident with TeV PWN candidates, and six are pointlike sources spatially coincident with PWNe. Most of these objects are located along the Galactic plane embedded within the prominent Galactic diffuse γ-ray emission (e.g., Figure 1), which makes these sources difficult to find. Additionally, nearly 150 rotation-powered pulsars that are capable of generating a PWN also emit brightly in the Fermi–LAT energy range, potentially outshining and obscuring their fainter PWNe[71] (D. A. Smith et al. 2023).

Of the $\sim$125 PWNe and PWN candidates currently known, 62 of these have no detected γ-ray pulsar. To minimize associated pulsar contamination and the need to consider pulsar timing solutions, we remove the 63 PWNe that have detected Fermi–LAT γ-ray pulsars from the source selection. We note that removing systems with associated γ-ray detected pulsars does not necessarily avoid contamination of magnetospheric emission (i.e., pulsar). In the case of no detected γ-ray pulsar, intrinsic pulsed emission can be present but too faint to detect in a pulsation search, whether using a timing solution or not. For more details on this impact, see Section 4.2. A second approach in the systematic search for γ-ray emitting PWNe will involve studying the off-pulse phases of Fermi–LAT detected pulsars for the presence of a PWN and will be reported in a subsequent paper.

Four additional PWNe are omitted due to their proximity to the Galactic center (within 1° or less). The remaining 58 PWNe analyzed in this search are listed with relevant parameters in Table 1. Each ROI is indicated on the 12 yr Fermi–LAT all-sky map for $E > 1$ GeV in Figure 1. We note that two additional ROIs located in the Large Magellanic Cloud (LMC), see Figure 2, are included in the analysis, each with an identified PWN.

3. Fermi–LAT Data Analysis

3.1. Data Selection

We use 11.5 yr (from 2008 August to 2020 January) of Pass 8 SOURCE class data (W. B. Atwood et al. 2013; P. Bruel et al. 2018) between 300 MeV and 2 TeV. Photons detected at

[69] The estimate is from a compilation of plerionic SNRs and PWNe reported in M. S. E. Roberts (20042004), G. Ferrand & S. Safi-Harb (2012), and S. P. Wakely & D. Horan (2008).

[70] http://snrcat.physics.umanitoba.ca/index.php?

[71] A publicly available list that is continuously updated can be found here: https://confluence.slac.stanford.edu/display/GLAMCOG/Public+List+of+LAT-Detected+Gamma-Ray+Pulsars.

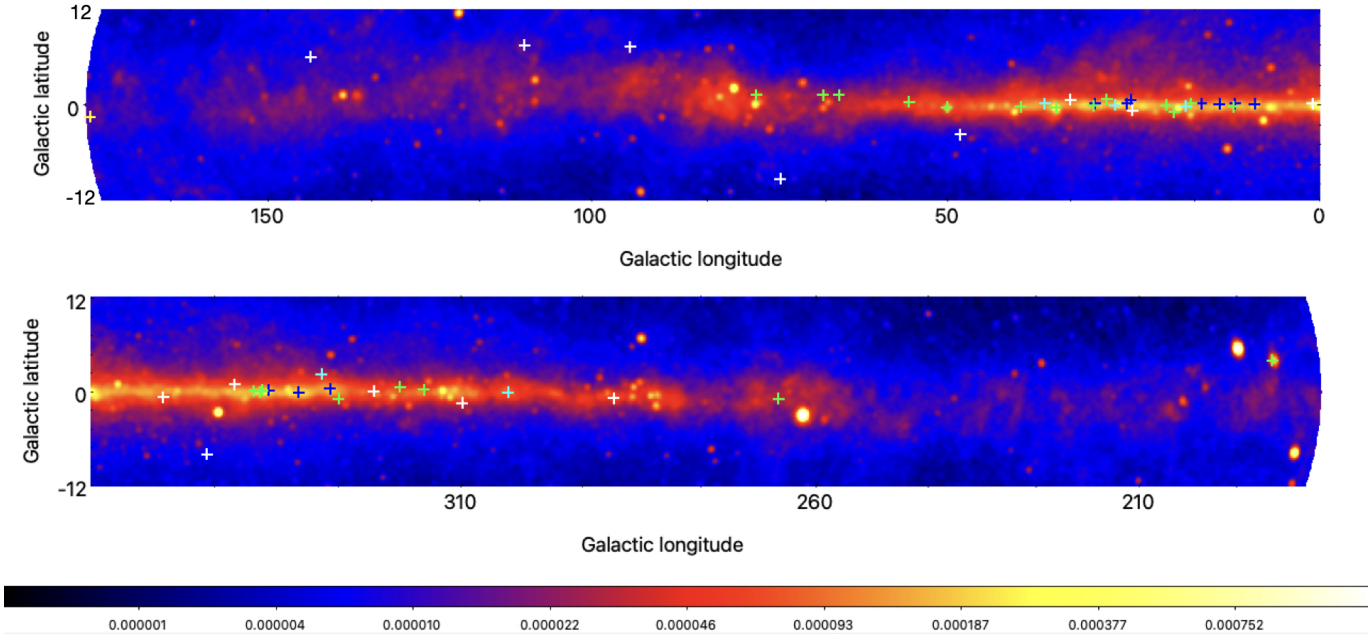

Figure 1. The Fermi–LAT intensity map of the Galactic plane for $|b| < 12^{\circ}$ using 12 yr of observational data with energies $E > 1$ GeV, based on `P8R3_SOURCE` class and `PSF3` event type. Note that 56 sources are indicated with crosses, and their color indicates whether the sources are detected (pointlike sources in green and extended in blue) and nondetections in white. Two sources are located in the Large Magellanic Cloud (LMC) and are not shown (see instead Figure 2). The units of the color scale are ph cm^{-2} s^{-1} sr^{-1}.

zenith angles larger than 100° were excluded to limit the contamination from γ-rays generated by CR interactions in the upper layers of Earth's atmosphere. We perform binned likelihood analyses with the Fermitools package[72] (v.2.0.8) and FermiPy Python 3 package (v.1.0.1, M. Wood et al. 2017), utilizing the `P8R3_SOURCE_V3` instrument response function (IRF) and account for energy dispersion, to perform data reduction and analysis. We organize the events by point-spread function (PSF) type, defined by the quality of their angular reconstruction,[73] using `evtype=4,8,16,32` to represent `PSF0`, `PSF1`, `PSF2`, and `PSF3` components. We consider separately all event types and then exclusively consider only `PSF3` events (`evtype=32`) for each ROI. The binned likelihood analyses are performed on each event type and, for the all event analyses, are then combined into a global likelihood function for the ROI to represent all events.[74] Performing a separate binned likelihood analysis for each event type increases the sensitivity of the joint likelihood fit and optimizes the spatial resolution of the LAT, a useful tool in resolving faint and/or extended structures in crowded regions. The γ-ray data are binned using a pixel bin size $0.^{\circ}1$ and 10 bins per decade in energy (38 total bins).

The maximum likelihood technique and the resulting test statistic (TS) are used to analyze the γ-ray data compared to the best-fit source model (see Section 3.2 for details on source model construction). The TS value is defined to be twice the natural logarithm of the ratio between the likelihood of one hypothesis $\mathcal{L}_1$ (i.e., presence of one additional source) and the likelihood for the null hypothesis $\mathcal{L}_0$ (i.e., absence of source):

$$\mathrm{TS} = 2 \times \log\left(\frac{\mathcal{L}_1}{\mathcal{L}_0}\right). \quad (1)$$

The TS quantifies the significance of a source detection for a given set of location and spectral parameters, and the significance of such a detection can be estimated by taking the square root of the TS (J. R. Mattox et al. 1996). For the analysis of coincident residual emission that is pointlike and faint (TS $\lesssim 25$ in `PSF3`), we must consider all events. For the analysis of coincident residual emission that is significantly detected and/or exhibits extension, we consider only events of `PSF3` type. This choice is motivated first and foremost by the source confusion and complexity of the majority of regions as observed by Fermi–LAT, with the added benefit of preserving computing time. The largest drawback of removing 75% of the photon events is the uncertainties in the spectral measurements for each source, which are estimated to improve by a factor of 2 when including all event types. Of the 58 ROIs, four have faint (TS $\lesssim 25$ in `PSF3`), pointlike detections that instead make use of all events: G54.10+0.27, B0453–685, G327.15–1.04, and G318.90+0.40 (see Section 4). The remaining ROIs utilize `PSF3` events only.

This analysis is complex and time intensive, during which Fermi–LAT continues to accumulate data. We have checked explicitly that additional integration time does not yield a change of conclusions for five of the ROIs using more of the available Fermi–LAT data (14 yr) and considering the 4FGL–DR4 catalog (J. Ballet et al. 2023). Event weighting is also explored for both 14 and 11.5 yr data sets, showing that the results reported in this work are in good agreement (in the Appendix A).

[72] https://fermi.gsfc.nasa.gov/ssc/data/analysis/software/
[73] https://www.slac.stanford.edu/exp/glast/groups/canda/lat_Performance.htm
[74] See FermiPy documentation for details: https://fermipy.readthedocs.io/en/0.6.8/config.html.

Table 1
All PWNe and PWN Candidate ROIs (Marked with "c" at the End of Their Galactic Name) Analyzed in This Paper

ROI	Galactic PWN Name	4FGL Name (CLASS1)	R.A.	Decl.	Extent	λ
1	G0.87+0.08	⋯	266.84	−28.15	0.04	Radio
2	G8.40+0.15	J1804.7–2144e (spp)	271.18	−21.74	0.25	TeV
3	G11.03–0.05c	J1810.3–1925e (spp)	272.52	−19.41	0.05	Radio
4	G11.09+0.08c	J1810.3–1925e (spp)	272.46	−19.21	0.05	Radio
5	G11.18–0.35	J1811.5–1925 (psr)	272.87	−19.43	0.04	Radio
6	G12.82–0.02	J1813.1–1737e (spp)	273.40	−17.83	0.05	TeV
7	G15.40+0.10c	J1818.6–1533 (spp)	274.50	−15.47	<0.04	TeV
8	G16.73+0.08	J1821.1–1422 (spp)	275.24	−14.33	0.015	Radio
9	G18.00–0.69	J1824.5–1351e (PWN)	276.26	−13.97	0.46	TeV
10	G18.90–1.10c	J1829.4–1256 (spp)	277.36	−12.97	0.15	Radio
11	G20.20–0.20c	J1828.0–1133 (spp)	277.03	−11.59	0.05	Radio
12	G23.50+0.10c	⋯	278.41	−8.454	0.017	X-ray
13	G24.70+0.60c	J1834.1–0706e (SNR)	278.55	−7.04	0.12	Radio
14	G25.10+0.02c	J1838.9–0704e (pwn)	279.51	−6.93	0.02	X-ray
15	G25.24–0.19	J1836.5–0651e (pwn)	279.34	−6.87	0.02	X-ray
16	G26.60–0.10	J1840.9–0532e (PWN)	280.14	−5.72	0.4	TeV
17	G27.80+0.60c	J1840.0–0411 (spp)	279.98	−4.29	0.11	Radio
18	G29.40+0.10c	J1844.4–0306 (unk)	281.14	−3.12	0.06	Radio
19	G29.70–0.30	J1846.4–0258 (pwn, DR4)	281.60	−2.97	<0.03	TeV
20	G32.64+0.53c	⋯	282.24	−0.04	0.09	TeV
21	G34.56–0.50	⋯	284.04	1.22	0.05	X-ray
22	G36.01+0.10	J1857.7+0246e (PWN)	284.34	2.76	0.26	TeV
23	G39.22–0.32	J1903.8+0531 (spp)	286.02	5.45	0.01	X-ray
24	G47.38–3.88	⋯	293.03	10.92	0.08	X-ray
25	G49.20–0.30c	J1922.7+1428c (unk/blank)	290.70	14.27	0.02	X-ray
26	G49.20–0.70c	⋯	290.83	14.06	0.02	X-ray
27	G54.10+0.27	J1930.5+1853 (DR3) (pwn)	292.61	18.84	<0.05	TeV
28	G63.70+1.10	J1947.7+2744 (pwn)	296.99	27.74	0.05	Radio
29	G65.73+1.18	J1952.8+2924 (spp)	298.21	29.48	0.1	TeV
30	G74.00–8.50c	⋯	312.33	29.02	0.05	X-ray
31	G74.94+1.11	J2016.2+3712 (snr)	304.04	37.19	0.13	Radio
32	G93.30+6.90c	⋯	313.06	55.29	0.01	X-ray
33	G108.60+6.80	⋯	336.42	65.60	0.05	X-ray
34	G141.20+5.00	⋯	54.30	61.89	0.03	Radio
35	G179.72–1.69	⋯	84.60	28.28	0.05	X-ray
36	G189.10+3.00	⋯	94.28	22.37	0.02	X-ray
37	G266.97–1.00	⋯	133.90	−46.74	0.04	Radio
38	G279.60–31.70	J0537.8–6909 (pwn)	84.45	−69.17	0.01	TeV
39	G279.80–35.80	⋯	73.41	−68.49	0.01	Radio
40	G290.00–0.93	⋯	165.44	−61.02	0.08	Radio
41	G304.10–0.24	J1303.0–6312e (PWN)	195.76	−63.19	0.18	TeV
42	G310.60–1.60	⋯	210.19	−63.43	0.02	Radio
43	G315.78–0.23	J1435.8–6018 (spp)	219.34	−60.02	0.07	Radio
44	G318.90+0.40c	J1459.0–5819 (unk)	224.71	−58.41	0.05	Radio
45	G322.50–0.10c	⋯	230.80	−57.10	0.08	Radio
46	G326.12–1.81	J1552.4–5612e (PWN)	238.11	−56.21	0.08	Radio
47	G327.15–1.04	J1554.4–5506 (DR3) (pwn)	238.67	−55.08	0.05	Radio
48	G328.40+0.20	J1553.8–5325e (blank)	238.89	−53.28	0.04	Radio
49	G332.50–0.30	J1616.2–5054e (PWN)	244.40	−50.94	0.02	X-ray
50	G332.50–0.28c	J1616.2–5054e (PWN)	244.41	−51.04	0.02	X-ray
51	G336.40+0.10	J1631.6-4756e (pwn)	247.98	−47.77	0.18	TeV
52	G337.20+0.10c	⋯	248.98	−47.32	0.03	X-ray
53	G337.50–0.10c	J1638.4–4715c (DR3) (blank)	249.51	−47.23	0.01	X-ray
54	G338.20–0.00	J1640.6–4632 (DR1), J1640.7–4631e (DR3) (spp)	250.19	−46.52	0.04	X-ray
55	G341.20+0.90	⋯	251.75	−43.77	0.06	Radio
56	G350.20–0.80c	⋯	260.91	−37.58	0.01	X-ray
57	G358.29+0.24c	⋯	265.32	−30.38	<0.07	TeV
58	G358.60–17.20c	⋯	284.15	−37.91	<0.01	X-ray

Note. Coincident 4FGL sources and their classifications are listed in the third column, considering the 4FGL–DR3 and DR4 catalogs (S. Abdollahi et al. 2022; J. Ballet et al. 2023). The 4FGL–DR3 and DR4 include new or updated sources from DR1 or DR2 and are indicated using the appropriate data release in parentheses. "PWN" = firm PWN counterpart, "pwn" = association with known PWN, "psr" = association with known pulsar, "SNR" = firm SNR counterpart, "snr" = association with known SNR, "spp" = association with known SNR or PWN, and "unk" or "blank" = unknown/unassociated. The observed R.A. and decl. in J2000 equatorial degrees are listed in the fourth and fifth columns as well as the observed extent (radius) in degrees in the sixth column. The last column specifies the wavelength of the observed positions and extents. TeV data are taken from http://tevcat.uchicago.edu/ (S. P. Wakely & D. Horan 2008) and radio or X-ray data from http://snrcat.physics.umanitoba.ca/SNRtable.php (G. Ferrand & S. Safi-Harb 2012).

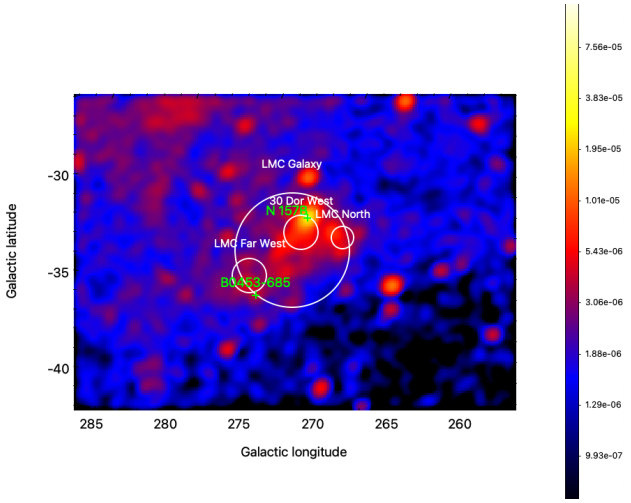

Figure 2. The Fermi–LAT intensity map for $E > 1$ GeV of the LMC centered on $(l,b) = (278.^{\circ}76, -33.^{\circ}46)$. The two sources analyzed in the LMC are indicated as green crosses. The four extended source components representing the diffuse LMC emission (following the *emissivity model* developed in M. Ackermann et al. 2016) are indicated in white. Based on `P8R3_SOURCE` class and `PSF3` event type. The units of the color scale are ph cm^{-2} s^{-1} sr^{-1}.

3.2. Building the Source Models

We model each ROI considering the comprehensive Fermi–LAT source catalog based on 10 yr of data, 4FGL-DR2 (J. Ballet et al. 2020), for point and extended sources[75] and the latest Galactic diffuse template to model the Galactic interstellar emission (`gll_iem_v07.fits`). For the four ROIs that require consideration of all events, we employ the isotropic diffuse template `iso_P8R3_SOURCE_V3_v1.txt`. For the remainder of ROIs that only consider `PSF3` events, the isotropic diffuse template employed is `iso_P8R3_SOURCE_V3_PSF3_v1.txt`.[76]

For most sources, a $10^{\circ} \times 10^{\circ}$ ROI is used to construct the source model considering 4FGL sources and backgrounds within 15° of the ROI center, which is always chosen to be the PWN position. The only sources that require larger ROIs (15°–20° while considering sources within 20°–25° of ROI center) are the PWNe that overlap with SNR S 147 (G179.72–1.69) and the Cygnus Loop (SNR G74.00–8.50). We instead consider events within 20° for G179.72–1.69 and within 15° for G74.00–8.50 due to the uniquely large SNR radii and the extended 4FGL counterparts. The shell of SNR S147 is nearly 5° in diameter and is an identified γ-ray emitter, 4FGL J0540.3+2756e, characterized best using the Hα SNR shell morphology that has radius $r \sim 2.^{\circ}5$. SNR G74.00–8.50 is nearly 8° in diameter and has a large extended source, 4FGL J2051.0+3049e (outer annulus radius $\sim 1.^{\circ}6$; H. Katagiri et al. 2011; A. Tutone et al. 2021), overlapping in location that may be associated with the SNR shell.

Two of the 58 ROIs are located within the LMC (see Figure 2): N 157B (G279.60–31.70, 4FGL J0537.8–6909) and newly detected B0453–685 (G279.80–35.80). Their location requires accounting for a third diffuse emission component from the LMC. The source models include four extended source components to reconstruct the *emissivity model* developed in M. Ackermann et al. (2016) to represent the diffuse LMC emission. The four additional sources are 4FGL J0500.9–6945e (LMC Far West), 4FGL J0519.9–6845e (LMC Galaxy), 4FGL J0530.0-6900e (30 Dor West), and 4FGL J0531.8–6639e (LMC North).

3.3. Detection Method

With the source models described above, we allow the isotropic and Galactic diffuse background components and sources with TS $\geqslant 25$ and a distance from the ROI center $\leqslant 3.^{\circ}0$ to vary in normalization and in spectral index (except for the isotropic background, which has no spectral index parameter). Sources that have TS < 25 are removed from the source model. We compute a series of diagnostic TS and count maps in order to search for and understand any residual γ-ray emission. We generate the counts and TS maps in the following energy ranges: 300 MeV–2 TeV, 1–10 GeV, 10–100 GeV, and 100 GeV–2 TeV. The motivation for increasing energy cuts stems from the improving PSF of the Fermi–LAT instrument with increasing energies.[77] We inspect the TS maps for any significant residuals (TS $\geqslant 25$) in the ROI, and point sources are added to the source model to account for these.

In most cases, unassociated, unknown, or plausibly PWN/SNR-related (i.e., "spp" class) 4FGL sources are already found to be coincident and likely counterparts to sources in the selected sample (Table 1). We consider any 4FGL sources as coincident if their centroid, extent, or uncertainty in position (95% confidence level, C.L.) overlap with the position of the PWN. For the majority of ROIs, the total number of coincident 4FGL sources is one. Other crowded regions may have an overlapping unidentified extended 4FGL source (e.g., G8.40+0.15, G11.18–0.35, G25.10+0.02, G25.24–0.19, G336.40+0.10, and G337.20+0.10). In either case, the sources falling on the PWN position are re-characterized when finding the best source model. The ROIs where the latter becomes relevant are explicitly described in Section 4.3. In the final source model of each ROI, there is only one source (whether pointlike or extended) that is associated with the PWN.

3.4. Localization and Extension

To model residual γ-ray emission that meets the Fermi–LAT significance threshold (TS = 25 for 4 DOF), we first add a fixed point source characterized by a power-law spectrum and index $\Gamma = 2$ to the 300 MeV–2 TeV global source model, after removing any unidentified 4FGL sources coincident with the source position. We localize the point source executing `GTAnalysis.localize` to find the best-fit position. If no better position is found, it remains fixed to the PWN location. Table 2 reports the results of detected point sources fixed to the PWN locations, and Table 3 provides the 95% positional uncertainty when the position is freed. Those without any positional uncertainty are fixed to the PWN location.

For all detected PWNe, we run extension tests in FermiPy utilizing `GTAnalysis.extension` and the two spatial templates supported in the FermiPy framework, radial disk and radial Gaussian. Both of these extended templates assume a symmetric 2D shape with width parameters radius, r, and sigma, σ, respectively. We allow the position to remain free when

[75] https://fermi.gsfc.nasa.gov/ssc/data/access/lat/10yr_catalog/.

[76] LAT background models and appropriate IRFs: https://fermi.gsfc.nasa.gov/ssc/data/access/lat/BackgroundModels.html.

[77] See https://www.slac.stanford.edu/exp/glast/groups/canda/lat_Performance.htm for a review on the dependence of the PSF with energy for Pass 8 data.

Table 2
Detected Point Sources Considered Likely PWNe (Top) or Candidate PWNe (Bottom)

Galactic PWN Name	4FGL Name	TS	Refs.[a]
G29.70–0.30 (Kes 75)	J1846.4–0258 (DR4)	20.7	S. M. Straal et al. (2023)
G54.10+0.27	J1930.5+1853 (DR3)	31.1	A. U. Abeysekara et al. (2018)
G279.60–31.70 (N 157B)	J0537.8–6909	168.3	M. Ackermann et al. (2016), S. Saito et al. (2017)
G279.80–35.80 (B0453–685)	…	18.4	J. Eagle et al. (2023)
G315.78–0.23 (Frying Pan)	J1435.8–6018	37.4	…
G327.15–1.04	J1554.4–5506 (DR3)	34.1	J. Eagle et al. (2022)
G11.18–0.35	J1811.5–1925	53.9	…
G16.73+0.08	J1821.1–1422	142.5	…
G18.90–1.10	J1829.4–1256	101.8	…
G20.20–0.20	J1828.0–1133	153.9	…
G27.80+0.60	J1840.0–0411	131	…
G39.22–0.32	J1903.8+0531	129.7	…
G49.20–0.30 (in W 51C)	J1922.7+1428c	157.2	…
G49.20–0.70 (in W 51C)	…	28.0	…
G63.70+1.10	J1947.7+2744	93.9	…
G65.73+1.18	J1952.8+2924	123.3	…
G74.94+1.11	J2016.2+3712	66.3	…
G318.90+0.40	J1459.0–5819	55.6	…
G337.20+0.10	…	18.4	…
G337.50–0.10	J1638.4–4715c (DR3)	42.7	…
G338.20–0.00	J1640.6–4632 (DR1), J1640.7–4631e (DR3)	174.8	…

Note. Results of the maximum likelihood fits along with the Galactic PWN name, 4FGL counterpart, and the TS for a fixed position at the PWN location (2 DOF). The final column lists the prior reports of broadband investigations that support a PWN origin.

finding the best-fit spatial extension of both templates. We measure the significance for extension to be $\mathrm{TS}_{\mathrm{ext}} = 2 \times \log\left(\frac{\mathcal{L}_{\mathrm{ext}}}{\mathcal{L}_{\mathrm{ps}}}\right)$, where $\mathcal{L}_{\mathrm{ext}}$ is the hypothesis for an extended source, and $\mathcal{L}_{\mathrm{ps}}$ is the point source hypothesis, following J. Lande et al. (2012) and M. Ackermann et al. (2017). We consider the source as extended when $\mathrm{TS}_{\mathrm{ext}} > 16$. The results of extended sources are provided in Table 4. Of the 15 extended sources, 13 were already extended in the 4FGL catalogs. The extensions found for these 13 sources are comparable to the sizes reported in the 4FGL, where the only differences are in the best-fit template used (see also Figure B1 in Appendix B). For all extended sources in this paper except for MSH 15–56, we find a radial Gaussian can better fit or fit just as well the γ-ray emission as the radial disk template. MSH 15–56 is the only extended source that is best fit with a custom spatial template, a template already adopted by the 4FGL catalogs and based on the PWN shape in radio (J. Devin et al. 2018).

The new best fit for 4FGL J1836.5–0651e can model well the extended emission coincident with the TeV PWN HESS J1837–069 ($r = 0.^{\circ}36$; H. E. S. S. Collaboration et al. 2018) such that the TS of the nearby extended source 4FGL J1838.9–0704e, a second possible PWN associated with HESS J1837–069, subsequently declines to TS = 0. We therefore suggest that there is only one extended source associated with HESS J1837–069, and it is most likely to be 4FGL J1836.5–0651e, though two X-ray PWNe are coincident in location with this extended source; see Section 4.3.1. There are two new extended sources in Table 4 that are not considered extended in the 4FGL catalogs: 4FGL J1818.6–1533 (PWN candidate G15.40+0.10) and 4FGL J1844.4–0306 (PWN candidate G29.40+0.10). Furthermore, we find that the detection for PWN G338.20–0.00 is pointlike, whereas the 4FGL–DR3 characterizes the emission with extension $r \sim 0.^{\circ}1$, based on the extension of its probable TeV counterpart HESS J1640–465 (A. Mares et al. 2021). Our results for G338.20–0.00 are in line with what is reported in the 4FGL–DR3, finding a 2D Gaussian yields the best fit with $r = 0.^{\circ}08$ and $\mathrm{TS}_{\mathrm{ext}} = 7.6$.

The smallest extended source is MSH 15–56 with a radius $r \sim 0.^{\circ}08$ and the largest extended source is 4FGL J1824.5–1351e (HESS J1825–137) with $r = 0.^{\circ}83$. The average extension

Table 3
Best-fit Positions of Detected Point Sources Considered Likely PWNe (Top) or Candidate PWNe (Bottom)

Galactic PWN Name	R.A.	Decl.	R95
G29.70–0.30 (Kes 75)	281.60	−2.96	0.09
G54.10+0.27	292.65	+18.90	0.10
G279.60–31.70 (N 157B)	84.40	−69.18	0.04
G279.80–35.80 (B0453–685)	73.46	−68.47	0.15
G315.78–0.23 (Frying Pan)	219.36	−60.11	0.14
G327.15–1.04	238.59	−55.11	0.08
G11.18–0.35	272.88	−19.44	0.05
G16.73+0.08	275.29	−14.35	0.05
G18.90–1.10	277.34	−12.88	0.06
G20.20–0.20	277.02	−11.57	0.06
G27.80+0.60	279.97	−4.27	0.04
G39.22–0.32	285.97	+5.50	0.05
G49.20–0.30 (in W 51C)	290.70	+14.27	…
G49.20–0.70 (in W 51C)	290.74	+14.09	0.03
G63.70+1.10	296.96	+27.73	0.07
G65.73+1.18	298.13	+29.46	0.05
G74.94+1.11	304.04	+37.20	0.04
G318.90+0.40	224.69	–58.38	0.10
G337.20+0.10	248.88	−47.19	0.06
G337.50–0.10	249.67	−47.28	0.09
G338.20–0.00	250.19	−46.57	0.19

Note. Same as Table 2, listing R.A. and Dec. in J2000 equatorial degrees and the 95% uncertainty radius in degrees of the best-fit position. G49.20–0.30 remains fixed to the PWN location (see text for details).

Table 4
Detected Extended Sources of Previously Identified PWNe (Top), Likely PWNe (Middle), and Candidate PWNe (Bottom)

Galactic PWN Name	4FGL Name	R.A.	Decl.	TS	TS_{ext}	r (°)	95% U.L. r[a] (°)	References
G18.00–0.69 (HESS J1825–137)	J1824.5–1351e	275.93	−13.88	151.5	88.29	0.83 ± 0.07 ± 0.10	1.01	M. H. Grondin et al. (2011)
G26.60–0.10	J1840.9–0532e	280.18	−5.52	288.6	74.32	0.36 ± 0.03 ± 0.04	0.41	F. Aharonian et al. (2008)
G36.01+0.10	J1857.7+0246e	284.22	+2.65	227.8	93.71	0.45 ± 0.05 ± 0.16	0.55	F. Aharonian et al. (2008)
G304.10–0.24 (HESS J1303–631)	J1303.0–6312e	195.81	−63.16	142.6	79.45	0.35 ± 0.03 ± 0.12	0.40	H. E. S. S. Collaboration et al. (2012a)
G326.12–1.81 (MSH 15–56)	J1552.4–5612e	238.11	−56.21	53.3	…	…	…	J. Devin et al. (2018)
G8.40+0.15	J1804.7–2144e	271.11	−21.74	104.8	59.65	0.29 ± 0.02 ± 0.11	0.34	B. Liu et al. (2019)
G25.10+0.02 (HESS J1837–069)	J1836.5–0651e	279.24	−6.91	1174	616.2	0.53 ± 0.02 ± 0.06	0.56	…
G25.24–0.19 (HESS J1837–069)	…	…	…		…	…	…	J. Lande et al. (2012)
G332.50–0.28	J1616.2–5054e[b]	244.20	−50.99	485.1	187.3	0.31 ± 0.02 ± 0.03	0.35	…
G332.50–0.30 (RCW 103)	…	…	…	…	…	…	…	M. Ackermann et al. (2017)
G336.40+0.10	J1631.6–4756e	248.14	−47.91	94.5	24.56	0.19 ± 0.03 ± 0.83	0.23	M. Ackermann et al. (2017)
G11.03–0.05	J1810.3–1925e	272.39	−19.42	84.0	25.88	0.41 ± 0.05 ± 0.05	0.49	…
G11.09+0.08	…	…	…	…	…	…	…	…
G12.82–0.02	J1813.1–1737e	273.47	−17.65	854.6	195.6	0.41 ± 0.02 ± 0.03	0.45	…
G15.40+0.10	J1818.6–1533	274.60	−15.56	394.5	20.60	0.19 ± 0.03 ± 0.10	0.24	…
G24.70+0.60	J1834.1–0706e	278.53	−7.12	290.8	72.57	0.19 ± 0.02 ± 0.02	0.22	M. Ackermann et al. (2017)
G29.40+0.10	J1844.4–0306	281.15	−3.12	195.7	18.77	0.27 ± 0.04 ± 0.17	0.34	…
G328.40+0.20 (MSH 15–57)	J1553.8–5325e	238.61	−53.38	1070	436.5	0.43 ± 0.02 ± 0.03	0.46	…

Notes. Results of the maximum likelihood fits along with the Galactic PWN name, 4FGL counterpart, R.A. and Dec. in J2000 equatorial degrees, the TS of the best fit and the TSext using the radial Gaussian spatial template (see Section 3.4 for details). The seventh and eighth columns quote the best-fit extension using the radial Gaussian template and the 95% upper limit. The first quoted error on the extension r corresponds to the symmetric 1σ statistical error and the latter corresponds to the systematic error. The final column lists the prior reports of broadband investigations that support a PWN origin. G326.12–1.81 uses the custom spatial template from the 4FGL (see also J. Devin et al. 2018).

[a] In all cases, $r = r_{68}$ such that $\sigma = \frac{r}{1.51}$ (J. Lande et al. 2012).

[b] RCW 103 is a known Fermi PWN, but may have contamination from a nearby PWN, G332.50–0.28, overlapping in location; see Section 4.3.1.

assuming a radial Gaussian for the sample of 15 extended sources is $r = 0.^{\circ}35$. Of the 36 total detections, 15 are found to be extended, which make up ∼40% of the entire sample analyzed here (see Appendix B for more discussion on extension). We explore the systematics on the extension in Section 3.6.

3.5. Spectral Shapes, Fluxes, and Upper Limits

We assume the source spectrum can be characterized as a power law for the full energy range[78]:

$$\frac{dN}{dE} = N_0\left(\frac{E}{E_0}\right)^{-\Gamma} \quad (2)$$

allowing the index and normalization to vary. The scale E_0 is fixed to 1 GeV for simplicity for all sources except N 157B and G304.10–0.24, where we use their catalog values E_0 of 5.3 and 11 GeV, respectively. We additionally perform curvature tests for all sources testing a log parabola spectrum,

$$\frac{dN}{dE} = N_0\left(\frac{E}{E_b}\right)^{-(\alpha+\beta\log E/E_b)} \quad (3)$$

fixing $E_b = 1$ GeV except for G318.90+0.40 and G326.12–1.81, which use their catalog values E_b of 2.2 and 5.5 GeV, respectively. In 4FGL-DR3 and later, $\mathrm{TS}_{\mathrm{Log}P} = 2\log\left(\frac{\mathcal{L}_{\mathrm{Log}P}}{\mathcal{L}_{\mathrm{PL}}}\right) > 4$ ($>2\sigma$) are considered preferentially curved spectra. To follow this method, we model the sources with $\mathrm{TS}_{\mathrm{Log}P} > 4$ using the best-fit log parabola spectrum that we measure. The remainder of sources are characterized by a power-law spectrum. The spectral and spatial properties are summarized in Table 5 alongside the properties of TeV counterparts for all detected sources. We provide the curvature metric in the second to last column. The MeV–GeV spectral values are in good agreement with those in the 4FGL catalogs.

For detected sources, we measure the energy flux from 300 MeV–1 TeV in seven energy bins using `GTAnalysis.sed`, where only the background components and the source of interest are left free to vary. Other sources are fixed to their values from the best-fit source model. We measure the systematic errors on the flux for all 36 source detections and describe the method and results in Section 3.6. The systematic errors for the spectral fluxes $E^2\frac{dN}{dE}$ per energy bin are listed in Appendix C, Table C1.

For nondetections, we place a point source characterized by a power-law spectrum at the location of the PWN, a spatial

[78] For a review of Fermi source spectral models, see https://fermi.gsfc.nasa.gov/ssc/data/analysis/scitools/source_models.html.

choice that corresponds to the size of the systems from multiwavelength observations (see Table 1) and perform a global fit with only the spectral parameters of the backgrounds and the point source free to vary. If the point source has TS < 25 for 4 DOF, we measure the 95% C.L. upper-limit spectral fluxes for the 300 MeV–2 TeV energy range and list them in the final column of Table 6, which lists the sources not detected in this analysis. We also calculate the 95% C.L. upper-limit spectral flux values for 300 MeV–2 TeV across nine energy bins. All upper-limit flux values for the 19 undetected sources are listed in Appendix C, Table C2.

3.6. Sources of Systematic Errors

We account for systematic uncertainties introduced by the choice of the interstellar emission model (IEM) and the IRFs, which mainly affect the spectrum of the measured γ-ray emission. We have followed the prescription developed by F. de Palma et al. (2013) and F. Acero et al. (2016), who generated eight alternative IEMs using a different approach than the standard IEM. For this analysis, we employ the eight alternative IEMs (aIEMs) that were generated for use on Pass 8 data in the Fermi–LAT Galactic Extended Source Catalog (FGES; M. Ackermann et al. 2017). We re-generate the best-fit model and perform independent fits for each ROI using the eight aIEMs for a total of nine fits per ROI including the standard model fit. We then compare the flux values to the standard model following Equation (5) in F. Acero et al. (2016).

We estimate the systematic uncertainties introduced by the uncertainty in the effective area[79] while enabling energy dispersion as follows: $\pm 3\%$ for $E < 100$ GeV, $\pm 4.5\%$ for $E = 175$ GeV, and $\pm 8\%$ for $E = 556$ GeV. Since the IEM and IRF systematic errors are taken to be independent, we can evaluate both and perform the quadratic sum for the total systematic error. This method has been applied in two prior catalogs and both reported systematic errors on the same order as the 1σ statistical errors in flux (see Figure 29 in F. Acero et al. 2016), which is consistent with our results (see Table C1 in Appendix C). In general, it is found that the systematics introduced by the uncertainty in the IEMs and IRFs are most important for sources that lie along the Galactic plane ($|b| < 1\overset{\circ}{.}0$) and for energies $E < 5$ GeV, largely dominated by the uncertainty in the IEMs.

For the two sources located in the LMC (Figure 2), N 157B (4FGL J0537.8–6909) and newly detected B0453–685, we find that the systematic errors are negligible for all energy bins, which is not surprising given the location of the LMC with respect to the bright, diffuse γ-ray emission along the Galactic plane. However, we must also account for the systematic error that is introduced by having an additional diffuse background component for the two LMC ROIs. We can probe these effects by employing the method described in M. Ackermann et al. (2016). This requires replacing the four extended sources that represent the diffuse LMC in this analysis (the *emissivity model*; M. Ackermann et al. 2016) with four different extended sources to represent an alternative template for the diffuse LMC (the *analytic model*; M. Ackermann et al. 2016). N 157B and B0453–685 are both refit with the alternative diffuse LMC template using the same approach as for the aIEMs described above. The uncertainty in the choice of the diffuse LMC template is similar in impact to the standard IEM, where the systematic errors are on the same order as the 1σ statistical errors in flux. Similarly, we find the errors are largest in the energy bins below 5 GeV, but are negligible for higher-energy bins.

Finally, we consider the use of weights particularly for the lowest-energies $E < 1$ GeV where the Galactic ridge is most prominent (S. Abdollahi et al. 2020). The effect from Galactic ridge emission decreases with increasing energy, becoming small above 1 GeV. The choice to use PSF3 events minimizes this effect, but it can still be noticeable in the softest sources as a systematic effect on the spectral index if the lowest-energy bin in the spectral fit has the largest influence. For PSF3 events, the weights increase the lowest-energy bin statistical errors at 316 MeV by a factor of $\sim$3. For all events, the effect is larger ($\sim$8). To further explore this, we look at the spectral index of all sources, comparing their values to those of the 4FGL counterparts for both 300 MeV–2 TeV and $E > 1$ GeV energy bands. No discrepancy is found in the spectral index. However, we still account for the potential bias effect without event weighting. This is accounted for in the systematic uncertainty of the flux in Table C1 in the lowest-energy bin for all sources. The LMC ROIs are not located in the Galactic ridge and thus do not suffer from this bias, having weights $\sim$0.5 below 1 GeV and $\sim$0.9 above 1 GeV. Nevertheless, the systematic uncertainty includes the conservative estimate ($\sim$0.12).

To explore the uncertainties on the extension influenced by the IEM and effective area, we follow the same method outlined for the spectral flux above: we re-generate the best-fit point-source model for all extended sources and perform extension tests. Each PWN is tested for extension considering the eight aIEMs for a total of nine extension tests per ROI including the standard model fit. We then compare the best-fit extension and symmetric error values to the standard model following Equation (5) in F. Acero et al. (2016). This method has been similarly applied in prior catalogs (F. Acero et al. 2016; M. Ackermann et al. 2017) and reported similar trends on the systematic error on extension as was found on the flux. The systematic errors for extension are generally also on the same order as the 1σ statistical errors (e.g., F. Acero et al. 2016), which is generally consistent with our results that are displayed in Table 4. For crowded regions, a larger error on both the flux and the extension is expected (see Tables 4 and C1, as well as M. Ackermann et al. 2017).

We note that the systematic uncertainties on extension for 4FGL J1631.6–4756e and 4FGL J1824.5–1351e are incompatible to prior systematic studies. For 4FGL J1631.6–4756e, we find this source is best fit as a radial Gaussian with $r = 0\overset{\circ}{.}19 \pm 0\overset{\circ}{.}027 \pm 0\overset{\circ}{.}83$, where the first quoted error represents the 1σ statistical error, and the latter is the systematic error. For comparison, the FGES catalog (M. Ackermann et al. 2017) found an extension using a radial disk template $r = 0\overset{\circ}{.}26 \pm 0\overset{\circ}{.}02 \pm 0\overset{\circ}{.}08$ for 4FGL J1631.6–4756e. However, this source lies in a crowded region among several other extended sources, including a larger, unknown extended 4FGL source (J1633.0–4746e) coincident in location, and therefore, the large systematic errors are not unexpected. 4FGL J1824.5–1351e, which we find is better fit as a radial Gaussian with $r = 0\overset{\circ}{.}83 \pm 0\overset{\circ}{.}074 \pm 0\overset{\circ}{.}10$, has a smaller systematic error than what is reported in the FGES catalog by 40%, but this is likely due to the larger radius found for the extension of 4FGL

[79] https://fermi.gsfc.nasa.gov/ssc/data/analysis/LAT_caveats.html

Table 5
Spectral and Spatial Properties Measured from This Work Compared to the TeV Counterparts (if Present) for Both Likely (Top) and Weak Candidates (Bottom)

PWN Name Likely	GeV Template	GeV Spectrum	GeV Flux ($eV\ cm^{-2}\ s^{-1}$)	GeV Index or α (at 1 GeV)	β	TeV ID	TeV Class	TeV Template	TeV Extension	TeV Index	TS_{LogP}	PSR?
G8.40+0.15	Gaussian	PowerLaw	79.9 ± 10.3	1.96 ± 0.04	⋯	HESS J1804–216	UNID	2-Gaussian	0.24 ± 0.03	2.69 ± 0.04	2.4	N
G18.00-0.69	Gaussian	LogParabola	139.0 ± 23.2	1.58 ± 0.06	0.04 ± 0.01	HESS J1825–137	PWN/TeV halo	3-Gaussian	0.46 ± 0.03	2.15 ± 0.06	32.0	N
G25.24−0.19	Gaussian	PowerLaw	285.0 ± 16.6	1.97 ± 0.02	⋯	HESS J1837–069	PWN	3-Gaussian	0.36 ± 0.03	2.54 ± 0.04	–0.5	N
G25.10+0.02	⋯	⋯	⋯	⋯	⋯	⋯	⋯	⋯	⋯	⋯	⋯	⋯
G26.60-0.10	Gaussian	PowerLaw	72.3 ± 6.98	2.15 ± 0.01	⋯	HESS J1841–055	PWN	2-Gaussian	0.41 ± 0.03	2.21 ± 0.07	0.32	N
G29.70–0.30	PointSource	PowerLaw	7.29 ± 1.65	2.41 ± 0.15	⋯	HESS J1846–029	PWN	PointSource	0.01	2.41 ± 0.09	−0.03	Y
G36.01+0.10	Gaussian	PowerLaw	65.1 ± 6.94	2.15 ± 0.05	⋯	HESS J1857+026	UNID	2-Gaussian	0.26 ± 0.06	2.57 ± 0.06	0.23	N
G54.10+0.27	PointSource	PowerLaw	3.82 ± 0.92	2.09 ± 0.12	⋯	HESS J1930+188	PWN	PointSource	0.03	2.59 ± 0.26	0.70	N
N157B	PointSource	PowerLaw	10.1 ± 1.61	2.11 ± 0.07	⋯	LHA 120–N157B	PWN	PointSource	0.01	2.80 ± 0.10	0.5	Y
B0453–685	PointSource	PowerLaw	0.75 ± 0.22	2.27 ± 0.18	⋯	⋯	⋯	⋯	⋯	⋯	3.7	Y
G304.10–0.24	Gaussian	PowerLaw	32.8 ± 6.03	1.88 ± 0.06	⋯	HESS J1303–631	PWN	2-Gaussian	0.18 ± 0.01	2.04 ± 0.06	−0.2	N
G315.78–0.23	PointSource	PowerLaw	5.66 ± 0.99	2.76 ± 0.16	⋯	⋯	⋯	⋯	⋯	⋯	2.1	Y
G326.12-1.81	SpatialTemplate	LogParabola	9.70 ± 2.03	1.23 ± 0.14	0.16± 0.04	⋯	⋯	⋯	⋯	⋯	6.7	N
G327.15–1.04	PointSource	LogParabola	2.48 ± 0.49	1.73 ± 0.28	0.41± 0.15	HESS J1554–550	PWN	PointSource	0.02	2.19 ± 0.17	5.0	Y
RCW 103	Gaussian	PowerLaw	117.5 ± 9.61	1.98 ± 0.03	⋯	HESS J1616–508	PWN	2-Gaussian	0.23 ± 0.03	2.32 ± 0.06	–0.4	N
G332.50–0.28	⋯	⋯	⋯	⋯	⋯	⋯	⋯	⋯	⋯	⋯	⋯	⋯
G336.40+0.10	Gaussian	PowerLaw	44.7 ± 6.04	2.05 ± 0.04	⋯	HESS J1632–478	PWN	Gaussian	0.18 ± 0.02	2.52 ± 0.06	1.2	Y
Weaker	⋯	⋯	⋯	⋯	⋯	⋯	⋯	⋯	⋯	⋯	⋯	⋯
G11.03–0.05	Gaussian	LogParabola	20.9 ± 3.24	1.88 ± 0.23	0.40 ± 0.19	HESS J1809–193	UNID	3-Gaussian	0.40 ± 0.05	2.38 ± 0.07	11.9	N
G11.09+0.08	⋯	⋯	⋯	⋯	⋯	⋯	⋯	⋯	⋯	⋯	⋯	⋯
G11.18–0.35	PointSource	PowerLaw	13.3 ± 2.90	2.03 ± 0.01	⋯	⋯	⋯	⋯	⋯	⋯	2.9	Y
G12.82–0.02	Gaussian	LogParabola	74.1 ± 3.30	2.24 ± 0.04	0.10 ± 0.03	HESS J1813–178	PWN	2-Gaussian	0.05 ± 0.004	2.07 ± 0.05	10.9	Y
G15.40+0.10	Gaussian	LogParabola	29.7 ± 1.69	2.65 ± 0.07	0.18 ± 0.08	2HWC J1819–150*	UNID	PointSource	0.09	2.21 ± 0.15	8.8	Y
G16.73+0.08	PointSource	PowerLaw	16.5 ± 1.55	2.72 ± 0.09	⋯	⋯	⋯	⋯	⋯	⋯	2.5	Y
G18.90–1.10	PointSource	LogParabola	8.26 ± 0.97	1.46 ± 0.24	0.66 ± 0.16	⋯	⋯	⋯	⋯	⋯	25.7	Y
G20.20–0.20	PointSource	LogParabola	15.4 ± 1.35	2.27 ± 0.13	0.50 ± 0.16	⋯	⋯	⋯	⋯	⋯	21.2	N
G24.70+0.60	Gaussian	PowerLaw	56.5 ± 6.37	2.02 ± 0.04	⋯	⋯	⋯	⋯	⋯	⋯	2.9	N
G27.80+0.60	PointSource	LogParabola	9.65 ± 1.13	1.62 ± 0.16	0.34 ± 0.07	⋯	⋯	⋯	⋯	⋯	12.3	Y
G29.40+0.10	Gaussian	PowerLaw	35.9 ± 2.71	2.55 ± 0.06	⋯	HESS J1844–030	UNID	PointSource	0.02	2.48 ± 0.12	3.8	Y
G39.22–0.32	PointSource	PowerLaw	15.5 ± 1.63	2.53 ± 0.09	⋯	⋯	⋯	⋯	⋯	⋯	1.5	N
G49.20–0.30	PointSource	LogParabola	37.2 ± 1.86	2.35 ± 0.06	0.26 ± 0.07	⋯	⋯	⋯	⋯	⋯	8.8	N
G49.20–0.70	PointSource	PowerLaw	18.5 ± 2.41	2.38 ± 0.09	⋯	⋯	⋯	⋯	⋯	⋯	2.4	N
G63.70+1.10	PointSource	LogParabola	4.38 ± 0.60	1.84 ± 0.22	0.37 ± 0.14	⋯	⋯	⋯	⋯	⋯	11.0	Y
G65.73+1.18	PointSource	LogParabola	5.63 ± 0.63	2.13 ± 0.19	0.58 ± 0.20	2HWC J1953+294	PWN	PointSource	0.24	2.78 ± 0.15	9.6	Y
G74.94+1.11	PointSource	PowerLaw	13.0 ± 1.75	2.24 ± 0.09	⋯	VER J2016+371	UNID	PointSource	0.08	2.30 ± 0.30	0.3	Y
G318.90+0.40	PointSource	LogParabola	2.47 ± 0.41	0.24 ± 0.83	1.16 ± 0.44	⋯	⋯	⋯	⋯	⋯	21.9	N
G328.40+0.20	Gaussian	LogParabola	103.0 ± 6.79	2.00 ± 0.06	0.05 ± 0.01	⋯	⋯	⋯	⋯	⋯	15.5	N
G338.20–0.00	PointSource	PowerLaw	37.6 ± 6.73	1.82 ± 0.06	⋯	HESS J1640–465	Composite SNR	2-Gaussian	0.11 ± 0.03	2.57 ± 0.04	−0.02	Y
G337.20+0.10	PointSource	PowerLaw	9.03 ± 2.04	2.26 ± 0.12	⋯	HESS J1634–472	UNID	Gaussian	0.11± 0.03	2.31 ± 0.05	0.2	N
G337.50–0.10	PointSource	PowerLaw	15.4 ± 1.67	2.69 ± 0.10	⋯	⋯	⋯	⋯	⋯	⋯	−1.23	N

Note. The quoted errors are the 68% C.L. values. TeV extension is in degrees. For pointlike TeV sources, we quote the 68% containment radius. All TeV values are taken from the TeVCat catalog (S. P. Wakely & D. Horan 2008). Those listed as X-Gaussian refer to multiple Gaussian components (see H. E. S. S. Collaboration et al. 2018, for details). The next-to-last column provides the curvature metric (see Section 3.5 for details). The final column provides the sources that have a possible additional low-energy spectral component such as the central pulsar (yes or no, Y/N). See Section 4.2 for details.

Table 6
Sources Not Detected by the LAT

Galactic PWN Name	4FGL Name	TeV Name	R.A.	Decl.	TS	Flux Upper Limit (MeV cm^{-2} s^{-1})
G0.87+0.08	⋯	HESS J1747–281	266.84	−28.15	0.05	1.62×10^{-7}
G23.50+0.10	⋯	⋯	278.42	−8.46	10.4	9.30×10^{-7}
G25.10+0.02	J1838.0–0704e	HESS J1837–069	279.37	−6.96	2.48[a]	3.83×10^{-7}
G32.64+0.53	⋯	IGR J18490–0000	282.25	−0.02	11.16	5.13×10^{-7}
G34.56–0.50 (in W44)	⋯	⋯	284.04	+1.22	4.58	1.12×10^{-6}
G47.38–3.88	⋯	⋯	293.03	+10.92	7.85	1.85×10^{-7}
G74.00–8.50 (in the Cygnus Loop)	⋯	⋯	312.33	+29.02	0.05	8.09×10^{-8}
G93.30+6.90	⋯	⋯	313.06	+55.29	7.43	1.77×10^{-7}
G108.60+6.80	⋯	⋯	336.42	+65.60	3.74	4.48×10^{-8}
G141.20+5.00	⋯	⋯	54.29	+61.89	0.00	4.34×10^{-8}
G179.72–1.69 (in S 147)	⋯	⋯	84.60	+28.28	10.3	9.91×10^{-8}
G189.10+3.00 (in IC 443)	⋯	⋯	94.28	+22.37	25.9[b]	1.26×10^{-6}
G266.97–1.00	⋯	⋯	133.90	−46.74	16.7	2.58×10^{-7}
G290.00–0.93 (IGR J11014-6103)	⋯	⋯	165.44	−61.02	0.00	9.91×10^{-8}
G310.60–1.60	⋯	⋯	210.19	−63.42	0.01	2.02×10^{-8}
G322.50–0.10	⋯	⋯	230.86	−57.10	8.62	2.40×10^{-7}
G341.20+0.90	⋯	⋯	251.87	−43.75	0.00	4.24×10^{-8}
G350.20–0.80	⋯	⋯	260.85	−37.61	14.9	4.96×10^{-7}
G358.29+0.24	⋯	HESS J1741–302	265.32	−30.38	0.00	1.85×10^{-7}
G358.60–17.20	⋯	⋯	284.15	−37.91	0.00	2.18×10^{-8}

Notes. Results of the maximum likelihood fits for PWNe and PWN candidates not detected by the LAT along with the Galactic PWN Name, TeV name if applicable, R.A. and declination in J2000 equatorial degrees, and the detection significance (TS) of a point source at the specified location. The last column provides the 95% C. L.flux upper limit for the 300 MeV–2TeV energy range.
[a] This source is classified as a potential PWN in the 4FGL–DR2 catalog associated with TeV PWN HESS J1837–069, but a detailed analysis of this region shows that only one extended source (4FGL J1836.5–0651e) is required to model residual emission here (see Sections 4.3.1 and 4.3.3 for details).
[b] Interpreted as a nondetection. See Section 4.3.3 for details.

J1824.5–1351e, a radial disk with $r = 1.^{\circ}05$ in the FGES catalog. For the remainder of the extended sources, we find compatible systematic uncertainties on the extension as those reported in the FGES catalog (see Table 4).

4. Comprehensive Results

Six of the 12 Fermi–LAT sources classified as PWNe, each detected as extended, are included in this sample (Table 1):

1. G18.00–0.69 (4FGL J1824.5–1351e)
2. G26.60–0.10 (4FGL J1840.9–0532e)
3. G36.01+0.10 (4FGL J1857.7+0246e)
4. G304.10–0.24 (4FGL J1303.0–6312e)
5. G326.12–1.81 (4FGL J1552.4–5612e)
6. HESS J1616–508 (4FGL J1616.2–5054e)

and eight Fermi–LAT PWN associations are also analyzed here:

1. N 157B (4FGL J0537–6909)
2. G29.70–0.3 (Kes 75, 4FGL J1846.4–0258, DR4)
3. G54.10+0.27 (4FGL J1930.5+1853, DR3)
4. G63.70+1.10 (4FGL J1947.7+2744)
5. G327.15–1.04 (4FGL J1554.4–5506, DR3)
6. G336.40+0.10 (4FGL J1631.6–4756e)
7. HESS J1837–069 (4FGL J1836.5–0651e and 4FGL J1838.9-0704e)

The ninth known PWN association, G0.13–0.11 (4FGL J1746.4–2852), is not considered here due to its proximity to the Galactic center. The remainder of known Fermi–LAT PWNe: 4FGL J0205.6+6449e (3C 58 powered by PSR J0205+6449; J. Li et al. 2018), 4FGL J0534.5+2201e (Crab), 4FGL J0833.1–4511e (Vela), 4FGL J1355.2–6420e, 4FGL J1420.3–6046e, and 4FGL J1514.2–5909e are all powered by Fermi–LAT detected pulsars and are not included in this search.

4.1. Source Classification

We consider three different properties to analyze the likelihood of our associations, with the notable caveat that the criteria do not provide an unambiguous PWN classification (see below):

1. Positional overlap with a PWN identified in radio, X-ray or TeV surveys,
2. Source extent as observed by the Fermi–LAT and the observed extent in radio, X-ray, or TeV surveys,
3. The energetics of the central pulsar, PWN, and host SNR.

The first criterion is positional coincidence, though alone it does not achieve a confident classification. For many Galactic sources detected by the Fermi–LAT, positional coincidence may include multiple sources. We must also consider the evolution and hence age of PWNe, since the broadband spectrum and morphology can change significantly depending on the evolutionary phase of the PWN. The physical consequences can become dramatic for PWNe believed to be in the reverberation phase, where the SNR reverse shock is crushing the PWN. The influences and conditions of this phase are not well known, though they are a current focus of ongoing studies (e.g., S. P. Reynolds & R. A. Chevalier 1984; D. Torres 2017; R. Bandiera et al. 2023a, 2023b). The findings

of current studies suggest that radiative losses dominate once the PWN is crushed by the reverse shock, which can result in the generation of a compact nebula of high-energy electrons separate from a diffuse nebula of low-energy electrons. The components can have different spectral and spatial characteristics, a reflection of the different particle energy losses. Therefore, the observed morphology is not necessarily a rigorous indicator for the dominant γ-ray origin. In general, evolved PWNe should have comparable extent in radio and GeV bands, often being larger than the X-ray and TeV extents.

Confidently classifying Fermi–LAT sources as PWNe is one of the biggest challenges, since it requires a combination of available multiwavelength observations and constraints on the energetics of the system. It is often the case that the central pulsar and(or) the SNR shell are not identified, which prevents reliable source classification. Given the challenge around understanding PWNe and their environments together with the energy-dependent angular resolution of Fermi–LAT, no robust classification method currently exists that is free of reasonable doubt, especially when considering the possibility that the central pulsar and(or) host SNR may contribute to the observed γ-rays or may even dominate the γ-ray signal. In fact, pulsars make up the largest Galactic source population in the 4FGL catalogs (J. Ballet et al. 2023; D. A. Smith et al. 2023) and SNRs outnumber the PWN population by a factor of 2, with 24 detected by the Fermi–LAT and another 19 listed as SNR candidates in the 4FGL (J. Ballet et al. 2023). Because source classification for high-energy PWNe is so difficult, we can only consider a small number of γ-ray sources here as likely PWNe, while the remainder require in-depth multiwavelength analyses to determine a likely origin. These are considered weaker PWN candidates.

We discuss the implications of pulsar contributions for the detected sources, particularly for energies $E < 10$ GeV where the spectral energy distributions (SEDs) for several of the sources indicate the possible presence of a lower spectral component, such as a pulsar, in the following section.

4.2. Pulsar Contributions

The presence of pulsar contributions particularly at lower energies ($E < 10$ GeV) is indicated by the 300 MeV–2 TeV SED for a number of likely PWNe and candidate PWNe (see Table 5, the final column). The possible pulsar contributions are listed as either a Y (yes) or N (no). The pulsar contribution possibility is assessed by the presence of any one of three features: (1) if the best-fit flux data points suggest more than one spectral component when compared to the best-fit spectral model, (2) if the source emission is primarily detected at low energies, similar to pulsars, and (3) if an energetic pulsar is known to the system. See Appendix C for a sample of source spectra regarding features (1) and (2).

Of course, the key features we consider are not fully representative of the possibility for pulsar contributions. We are limited in evaluating many of the γ-ray sources (statistics will not yield reliable pulsation search results) and their associations (not all central pulsars have been identified), and the problem is also compounded by the complexity of the nature of γ-ray pulsars (unpulsed emission may be present but would not be detected in a pulsation search; e.g., M. Dormody et al. 2011). As a final note, the presence of two spectral components does not confirm the presence of a pulsar contribution. Many PWNe, such as Vela–X (e.g., L. Tibaldo et al. 2018), have multiple emission components in the Fermi–LAT band.

G29.70–0.3, B0453–685, and G327.15–1.04 have been independently analyzed in separate reports (see S. M. Straal et al. 2023; J. Eagle et al. 2022, 2023), where a pulsar contribution is explored or questioned. In these cases, the PWN is expected to dominate above a few GeV. Many of the sources reported here are significantly detected above 10 GeV and/or have significant extension. Despite the possible presence of a low-energy spectral contribution, a dominant PWN contribution at higher energies is indicated.

The likely PWNe with possible pulsar components include: G29.70–0.30 (Kes 75), G315.78–0.23, G327.15–1.04, G336.40+0.10, N 157B, and B0453–685, which is the majority of likely PWNe (six out of nine). Similarly for the other Fermi–LAT PWN candidates: G11.18–0.35, G12.82–0.02, G15.40+0.10, G16.73+0.08, G18.90–1.10, G27.80+0.60, G29.40+0.10, G63.70+1.10, G65.73+1.18, G74.94+1.11, and G338.20–0.00 have possible additional spectral components arising in the lower energy band ($E < 10$ GeV), which correspond to 11/21 candidate PWNe. This brings the total number of sources with a possible pulsar component in this sample to 17. We attempt to characterize any additional spectral component, described below.

The six likely Fermi–LAT PWNe with a potential second component are tested with two different additional spectral shapes to the source spectrum: (1) a simple power law and (2) a power law with an exponential cutoff (PLEC4 from the 4FGL-DR3 catalog[80]). Likely due to low statistics in most of the PWNe, however, no secondary contributions could be detected, except for G29.70–0.30, which has a likely MeV pulsar (L. Kuiper et al. 2018; S. M. Straal et al. 2023), and yields a 3σ detection for a second source at the pulsar location (TS $\sim$ 13). The pulsar contribution tests for G327.15–1.04 and B0453–685 imply that a single PLEC4 source can marginally improve the fit over a source assuming a simple power law, which may indicate PWN entanglement with any present pulsar contribution. Both PWNe lack the statistics, and the detection of a central pulsar to explore this possibility further.

A second test for a possible low-energy spectral component is to split the energy range into two: 300 MeV–3 GeV and 3 GeV–2 TeV. If a pulsar or low-energy contribution exists, one would expect the spectral index $E < 3$ GeV to be softer than above 3 GeV. No significant differences in the spectral indices are found for the sources that are fit using a power law. The sources that are better fit using a log parabola spectrum tend to indicate slightly softer spectral indices for 3 GeV–2 TeV, than for 300 MeV–3 GeV, as expected for curved spectra.

As a final check, we also compare our best-fit spectral index for each source to the 4FGL values for those that have associated 4FGL counterparts. We do this for two different data sets of each ROI: `ALL` event types and then again for just the `PSF3` event type. We verify that no source deviates from the 4FGL spectral index value unless dramatic changes were adopted in this work with respect to the 4FGL catalogs aside from the different energy range (changes to location, spatial templates, size, etc.). We also inspect the spatial count profiles in both Galactic latitude and longitude around each source. These checks reasonably rule out the presence of systematic

[80] https://fermi.gsfc.nasa.gov/ssc/data/analysis/scitools/source_models.html

contamination such as the Galactic background. All sources reported here have a distinct spatial separation from the diffuse background. While we cannot rule out or confirm the presence of a lower-energy component such as a contributing pulsar, we can rule out systematic contamination.

4.3. Results by ROI

We discuss the results of a majority of the new source detections and classifications along with their morphological and spectral characteristics in this section. In Section 4.3.1, we describe each of the likely PWN classifications. In Section 4.3.2, we discuss the majority (15/21) of the weaker PWN candidates, chosen by either (i) the multiwavelength evidence supporting follow-up investigations to constrain the origin or (ii) the unclear nature of the GeV emission due to being in complex regions of the γ-ray sky. The latter motivates follow-up analysis in the high-energy regime. For the sources where there is significant source emission between 1 and 10 GeV or $E > 10$ GeV, we display TS images in these energy ranges. This choice avoids the declining angular resolution below these energies. For sources where this is not possible, TS maps from the full energy range 300 MeV–2 TeV are displayed.

4.3.1. Likely PWNe

G8.40+0.15. First detected in the TeV band (F. Aharonian et al. 2005), HESS J1804–216 is an extended unidentified source with semimajor and semiminor axes $0.^{\circ}24$ and $0.^{\circ}16$, respectively. In B. Liu et al. (2019), the corresponding extended GeV emission is found to most likely originate from two unrelated sources: PWN G8.40+0.15 and SNR G8.7–1.4. 4FGL J1805.6-2136e is plausibly the SNR G8.7–1.4, and 4FGL J1804.7-2144e (coincident with TeV source HESS J1804–213) is argued to be the PWN G8.40+0.15. B. Liu et al. (2019) and the 4FGL catalogs characterize the GeV PWN counterpart as a radial disk with $r = 0.^{\circ}38$ (M. Ackermann et al. 2017). A careful analysis of the Fermi–LAT data in this region confirms that the two extended sources reported in B. Liu et al. (2019) provide the best-fit spatial model, with a small adjustment on the likely PWN 4FGL J1804.7-2144e. We find that a smaller extension using the radial Gaussian template $r = 0.^{\circ}29$ characterizes the emission just as well (see Table 4). The best-fit spectrum is a power law, and the spectral index is softer than the spectrum measured in B. Liu et al. (2019), but is consistent with what is reported in the 4FGL catalogs: $\Gamma = 1.96 \pm 0.04$ (M. Ackermann et al. 2017; J. Ballet et al. 2023). We plot the best-fit log parabola spectral model from B. Liu et al. (2019) alongside the Fermi–LAT and HESS flux data points in Figure 3 (right panel), showing that the spectral measurements, overall, agree well. The TeV emission is characterized as a power law with $\Gamma = 2.69 \pm 0.04$ (H. E. S. S. Collaboration et al. 2018), indicating that the peak of γ-ray emission is likely occurring in the Fermi–LAT band. Given the broadband results of B. Liu et al. (2019), the agreement between the H.E.S.S. and Fermi–LAT extensions, spectral properties, and the positional coincidence with an identified PWN that extends $12''$ from the pulsar PSR J1803–2137 as observed by Chandra (O. Kargaltsev et al. 2007), we classify 4FGL J1804.7–2144e as a likely PWN (see Figure 3, left panel). This does not preclude, however, that contamination from other sources in the complex (SNR, PSR) contribute to the γ-ray data.

G29.70–0.30 (Kes 75). G29.70–0.30 is the youngest known PWN in the Milky Way with an estimated age $\tau \sim 500$ yr (S. P. Reynolds et al. 2018). It is powered by a very energetic pulsar that may be a magnetar based on its high surface magnetic field strength and having emitted several magnetar-like short X-ray bursts (S. P. Reynolds et al. 2018). The magnetar-like pulsar is detected in 30–100 MeV Fermi–LAT data at the 4.2σ significance level (L. Kuiper et al. 2018) with a peak energy at $E \sim 3$ MeV. The $E < 100$ MeV pulsed emission is characterized as a superexponential cutoff power law with a hard photon index before the break $\Gamma \sim 0.9$ and a cutoff energy at $E_c \sim 0.009$ MeV. Pulsations disappear before $E = 100$ MeV (L. Kuiper et al. 2018). Combined with a faint source detection, this prevents a pulsation search from being feasible above this energy. S. M. Straal et al. (2023) characterized a pulsar component $\Gamma \sim 1.5 \pm 0.4$ and $E_c \sim 1$ GeV for 100 MeV $< E <$ 5 GeV. The PWN is visible in radio ($\sim 0.'6$ in size) and X-ray as a bright, compact nebula encompassed by an incomplete radio SNR shell ($\sim 4'$ in size).

The PWN is a known TeV emitter HESS J1846–029. There is a nearby unknown source 4FGL J1846.9–0247c that is plausibly associated with Kes 75; however, the diffuse residuals are improved when this source remains in the model; thus, it is not the likely counterpart. A significant detection for an additional point source at the position of Kes 75 is found. In 4FGL-DR4 (J. Ballet et al. 2023), this corresponds to the new source 4FGL J1846.4–0258. A detailed broadband investigation was performed in S. M. Straal et al. (2023), who argued 4FGL J1846.9–0247c is indeed the PWN from Kes 75. Despite slight differences in the source model they use, we measure consistent spectral results for the PWN as in S. M. Straal et al. (2023), who found a photon index for the PWN above $E > 5$ GeV of $\Gamma_\gamma = 2.49 \pm 0.38$. The best-fit photon index measured between 300 MeV and 2 TeV is $\Gamma = 2.41 \pm 0.15$, and is also in agreement with the H.E.S.S. spectral index $\Gamma = 2.41 \pm 0.09$; see Figure 4. We classify Kes 75 as a likely Fermi–LAT PWN, although it is probable that both the pulsar and the PWN contribute to the observed Fermi–LAT signal.

HESS J1837–069. First detected as an unidentified TeV source (F. Aharonian et al. 2005), it was investigated as a PWN candidate after the discovery of two compact ($\lesssim 1'$) X-ray PWNe inside the extended H.E.S.S. source ($r \sim 0.^{\circ}36$; E. V. Gotthelf & J. P. Halpern 2008; H. E. S. S. Collaboration et al. 2018). The subsequent detection of an extended Fermi–LAT counterpart (F. Acero et al. 2013b) further supported HESS J1837–069 as a strong TeV PWN candidate. The investigation into the local environment solidified the PWN origin as the most probable source class (Y. Fujita et al. 2014). Displayed in Figure 5 (left panel) is the HESS J1837–069 TS map and all potential counterparts indicated. Two X-ray PWNe are coincident in location with both the extended TeV and GeV sources: PWN AX J1837.3–0652 ("AX PWN" or G25.24–0.19) and the close by compact PWN G25.10+0.02 powered by PSR J1838–0655 (O. Kargaltsev et al. 2012). PSR J1838–0655 has a spin-down power $\dot{E} \sim 5 \times 10^{36}$ erg s^{-1} and characteristic age $\sim$23 kyr. AX J1837.3–0652, while much fainter in X-ray than PSR J1838–0655, may have similar characteristics (E. V. Gotthelf & J. P. Halpern 2008), making both plausible contributors to the TeV emission. There are two extended sources associated with HESS J1837–069 in the

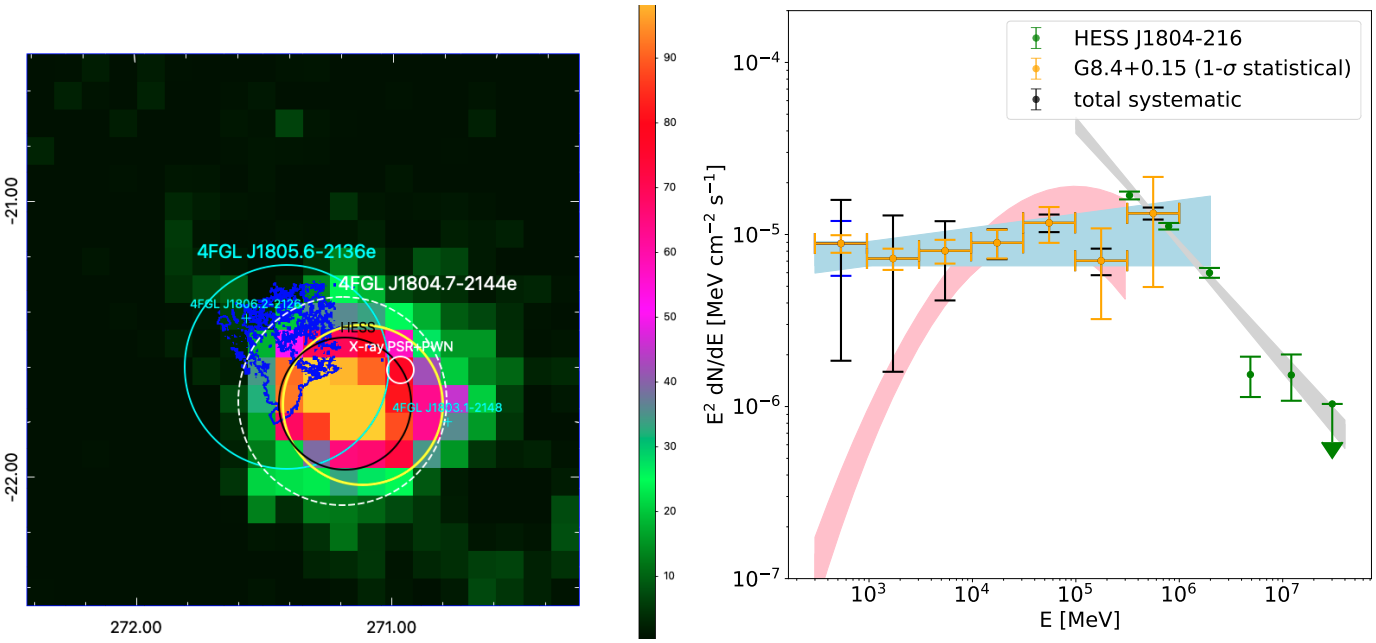

Figure 3. Left panel: a 2° × 2° 300 MeV–2 TeV TS map of PSF3 events for PWN G8.40+0.15. The color scale reflects the TS value. The TeV PWN HESS J1804–216 is displayed as a black circle, $r = 0.^{\circ}24$. The position of PSR J1803–2137 and the size of the extended nebula observed in X-ray are marked and labeled as the white circle. The blue contours represent the SNR G8.7–1.4 in radio. The 4FGL J1804.7–2144e position and extent are indicated by the white dashed circle but are not included in the source model. The best-fit position and extent of the radial Gaussian template are indicated by the yellow circle. The maximum TS is ∼122. Note that 4FGL sources in the field of view are labeled in cyan. The coordinates are in J2000 equatorial degrees. Right panel: the best-fit Fermi–LAT spectral model (blue band) and data (yellow points) for PWN G8.40+0.15 are plotted beside the best-fit spectral model of its TeV counterpart HESS J1804–216 in gray from H. E. S. S. Collaboration et al. (2018). The blue flux error for $E < 1$ GeV is the additional systematic error, as discussed in Section 3.6. The log parabola model from B. Liu et al. (2019) is plotted in pink.

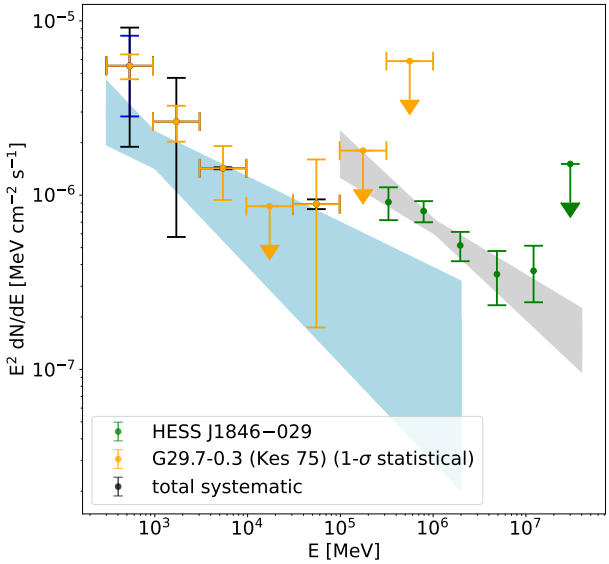

Figure 4. The best-fit Fermi–LAT spectral model (blue band) and data in yellow for PWN G29.70–0.30 (Kes 75) are plotted beside the best-fit spectral model (gray band) and data in green of its TeV counterpart HESS J1846–029 from H. E. S. S. Collaboration et al. (2018). The blue flux error for $E < 1$ GeV is the additional systematic error, as discussed in Section 3.6.

4FGL: 4FGL J1838.9–0704e and 4FGL J1836.5–0651e. 4FGL J1836.5–0651e is modeled with $r = 0.^{\circ}53$, and 4FGL J1838.9–0704e is similarly fit as $r = 0.^{\circ}52$, both as a radial disk in the 4FGL (M. Ackermann et al. 2017; J. Ballet et al. 2023). We find that there is only one extended source required for the observed emission, and it corresponds to 4FGL J1836.5–0651e; however, it is significantly better fit as a radial Gaussian with extension $r = 0.^{\circ}53$. The GeV spectral index $\Gamma = 1.97 \pm 0.02$ is harder than the TeV PWN spectral index $\Gamma = 2.54 \pm 0.04$ (see Figure 5, right panel), connecting the GeV and TeV spectra.

Given the PWN classification of the TeV source HESS J1837–069 and the positional coincidence of the TeV and GeV emission with two compact X-ray PWNe, it seems likely the GeV counterpart is a PWN. It is possible that one or both X-ray nebulae contribute. Therefore, we classify the extended emission modeled by 4FGL J1836.5–0651e as a likely PWN, but multiwavelength investigations are needed to determine the X-ray counterpart(s).

G54.10+0.27. G54.10+0.27 is a young, Crab-like SNR (i.e., presence of pulsar and diffuse PWN emission, but lacks an SNR shell) powered by pulsar J1930+1852 and is roughly ∼2′ in size as observed by Chandra (T. Temim et al. 2010). The central pulsar and PWN have been studied in detail in both radio and X-ray (e.g., F. Camilo et al. 2002; T. Temim et al. 2010; J. D. Gelfand et al. 2015). Pointlike TeV emission HESS J1930+188 is identified as the TeV counterpart to the PWN (H. E. S. S. Collaboration et al. 2018). 4FGL J1930.5+1853 is probably the PWN G54.10+0.27 considering the positional coincidence. The agreement in position and spectral index between the GeV and TeV emission ($\Gamma = 2.09 \pm 0.12$ in GeV and $\Gamma = 2.59 \pm 0.26$ in TeV; see also both panels of Figure 6 and H. E. S. S. Collaboration et al. 2018) classifies the source as a likely PWN. Confirmation of the true source class will require an in-depth multiwavelength investigation to rule out source contamination, whether related (pulsar, PWN, or SNR) or unrelated (nearby source).

N 157B. N 157B is a young PWN powered by PSR J0537–6910 (characteristic age $\tau_c \sim 4.9$ kyr) located within the

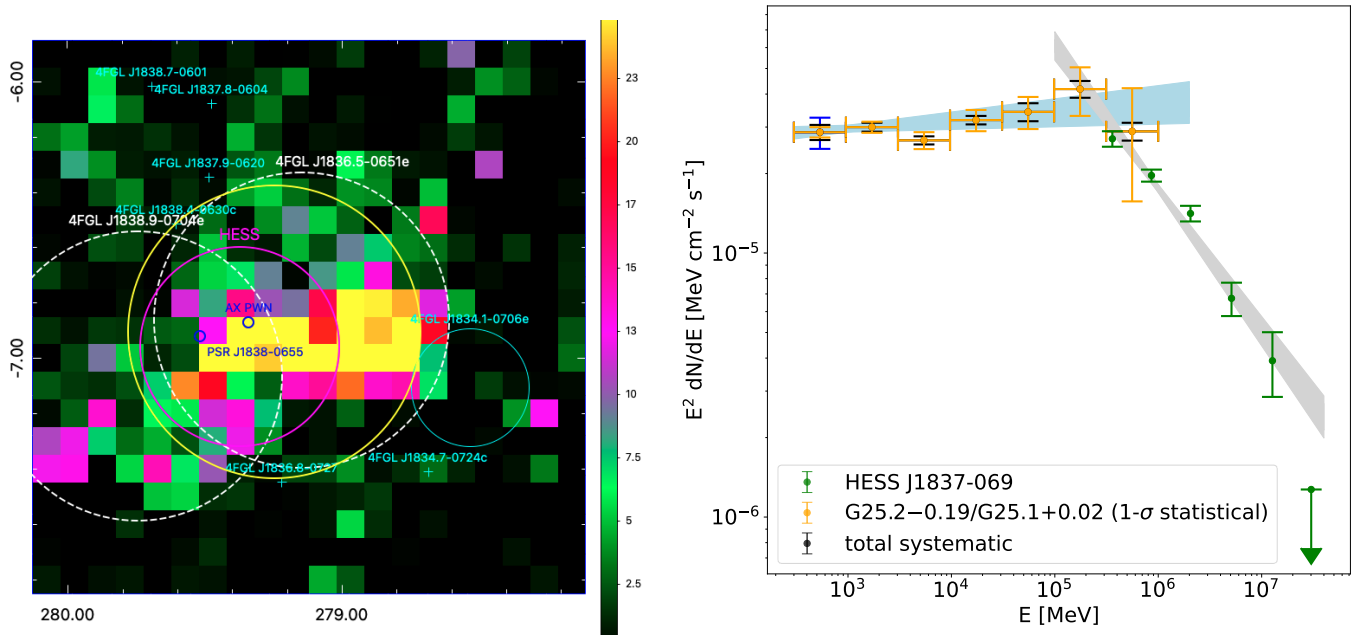

Figure 5. Left panel: a 2° × 2° TS map for $E > 10$ GeV of the TeV PWN HESS J1837–069 (magenta circle). The 4FGL J1836.5–0651e and 4FGL J1838.9–0704e positions and extents are indicated by the white dashed circles but are not included in the source model. The best-fit position and extent of the radial Gaussian template are indicated by the yellow circle. The blue circles correspond to the location and size of the X-ray nebulae G25.24–0.19 ("AX PWN") and G25.10+0.02 powered by PSR J1838–0655. The maximum TS at the PWN positions is ∼46. Unrelated 4FGL sources are indicated in cyan. Right panel: the best-fit Fermi–LAT spectral model (blue band) and data in yellow for the extended source coincident with both PWN G25.10+0.02 and G25.24–0.19 (J1836.5–0651e) as well as the best-fit spectral model (gray band) and data in green of its TeV counterpart HESS J1837–069 from H. E. S. S. Collaboration et al. (2018). The blue flux error for $E < 1$ GeV is the additional systematic error, as discussed in Section 3.6.

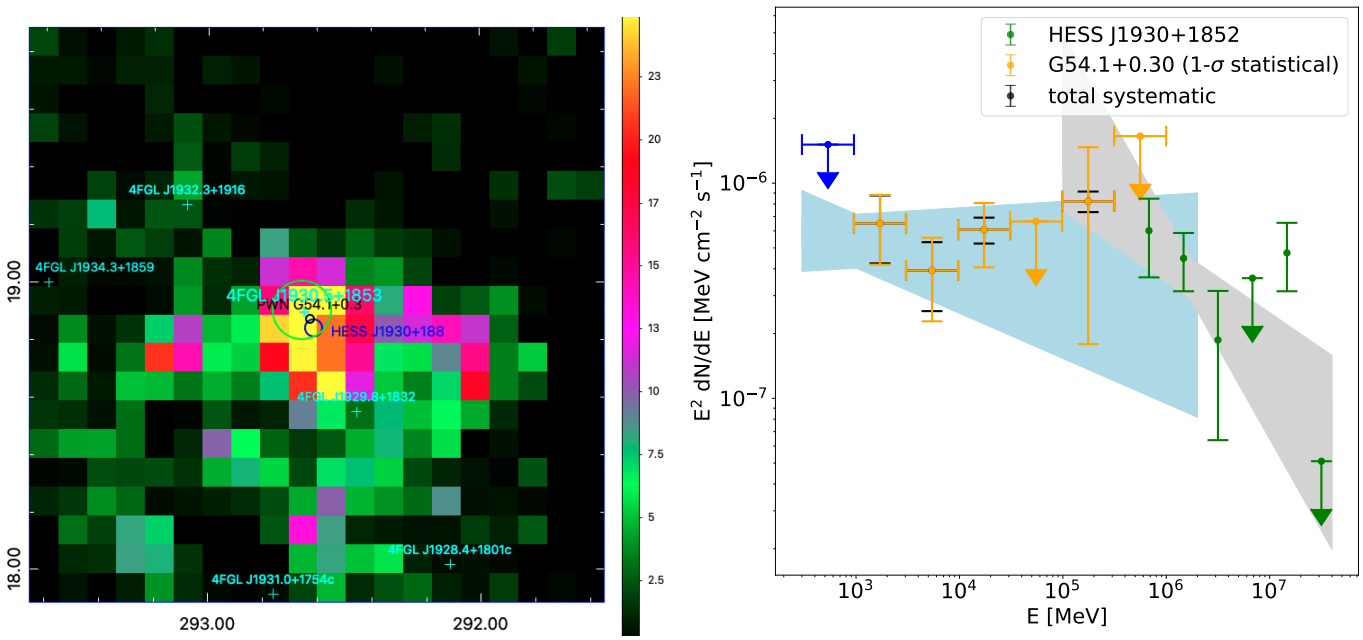

Figure 6. Left panel: a 2° × 2° 300 MeV–2 TeV TS map of ALL events for PWN G54.10+0.27. The green circle represents the 95% positional uncertainty of a point source at the PWN position and corresponds to the DR3 source 4FGL J1930.5+1853. The black circle represents the size and location of the X-ray PWN. The 68% uncertainty region for the TeV PWN HESS J1930+188 is indicated in blue. The maximum TS at the PWN position is ∼32. Unrelated 4FGL sources are indicated in cyan. Right panel: the best-fit spectral model (blue band) and data in yellow of J1930.5+1853 as well as the best-fit spectral model (gray band) and data in green of its TeV counterpart HESS J1930+188 from H. E. S. S. Collaboration et al. (2018). The blue flux upper limit for $E < 1$ GeV is from the additional systematic error, as discussed in Section 3.6.

LMC and is the first MeV–GeV (M. Ackermann et al. 2016; S. Saito et al. 2017) and TeV (H. E. S. S. Collaboration et al. 2012b) detection for γ-ray emission associated with a PWN outside of the Milky Way. The pulsar has a spin-down luminosity even larger than that of the Crab pulsar ($L \sim 5 \times 10^{38}$ erg s^{-1}), making it the most rapidly spinning and most powerful young pulsar known, with a spin period ∼16 ms (F. E. Marshall et al. 2004). The γ-ray detection of N 157B is possible given the central pulsar's enormous power output, in addition to potentially rich local photon fields that

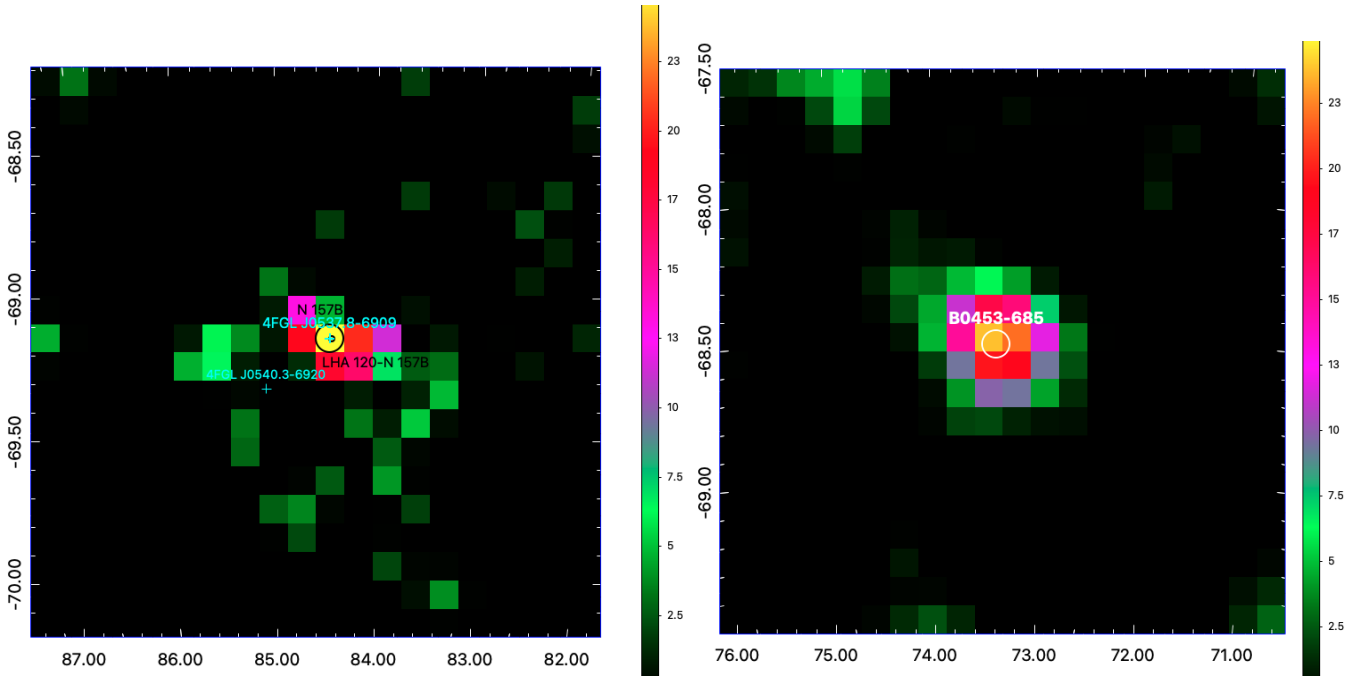

Figure 7. Left panel: a $2^\circ \times 2^\circ$ 10 GeV–2 TeV TS map of `PSF3` events for PWN N 157B. The 4FGL counterpart is 4FGL J0537.8–6909, indicated in cyan with the 95% positional uncertainty (outer black circle). The TeV PWN "LHA 120–N 157B" (inner black circle) is indicated. Unrelated nearby 4FGL sources are labeled in cyan. The maximum TS at the PWN/SNR position is ∼35 for $E > 10$ GeV. Right panel: a $2^\circ \times 2^\circ$ TS map of `ALL` events centered on B0453–685 (white circle) between 1 and 10 GeV. The maximum TS at the PWN/SNR position is ∼24 in the 1–10 GeV energy range.

facilitate a large IC flux. Pointlike GeV emission coincident with the system could plausibly be from the energetic pulsar, the PWN, or the SNR (M. Ackermann et al. 2016). The morphology of the PWN/SNR is not clear: the lack of thermal X-rays and the missing limb-brightened outer SNR shell imply a Crab-like morphology, but the diffuse X-rays beyond the cometary nebula have a weak thermal component, implying possible re-heated SN ejecta from the passage of the reverse shock (Y. Chen et al. 2006). Even though the observed Fermi–LAT emission cannot firmly rule out an SNR scenario when considered alone, it seems unlikely given the lack of observational evidence for an energetic SNR shell in other wave bands. Pulsations from the central pulsar were searched for in the observed γ-ray emission, but none were evident above a 1σ C.L. (M. Ackermann et al. 2016). The identified TeV counterpart of the PWN combined with no detectable pulses in the Fermi–LAT signal and a photon index similar to other Fermi–LAT PWNe ($\Gamma = 2.11 \pm 0.07$) guide us to classify this source as a likely PWN (see also Figure 7, left panel).

B0453–685. SNR B0453–685 is a middle-aged ($\tau \sim 14$ kyr) composite SNR located in the LMC, on the opposite (western) side from PWN N 157B (e.g., Figure 2; see also B. M. Gaensler et al. 2003). Fermi–LAT γ-ray emission coincident with SNR B0453–685 is detected at a significance level $>4\sigma$ (see Figure 7, right panel). The γ-ray emission displays no evidence for extension, and the best-fit spectral index $\Gamma = 2.27 \pm 0.18$ characterizes a power-law spectrum. There is no known TeV counterpart for this system. While the central pulsar has not been detected, a detailed multiwavelength investigation described in J. Eagle et al. (2023) found the most likely origin to be the PWN with a possible pulsar contribution below 5 GeV. The host SNR displays energetics that are inconsistent if the SNR is the γ-ray origin, such as no detectable nonthermal emission in X-ray nor any indication of an interaction with ambient media. However, this does not rule out possible SNR contamination to the γ-ray data. The position, extent, and energetics favor a PWN dominant origin.

G315.78–0.23. Also known as the Frying Pan, this ancient system features a radio SNR shell and an exiting supersonic pulsar that powers a trailing PWN in its wake (C. Y. Ng et al. 2012). An unidentified point source 4FGL J1435.8–6018 is in close proximity to the radio position of the bow-shock PWN and pulsar. We investigate the possible association with PWN G315.78–0.23 by replacing 4FGL J1435.8–6018 with a point source at the PWN position, in addition to two point sources to the southwest of the SNR shell in order to model unrelated, persisting diffuse residual γ-ray emission. Localizing 4FGL J1435.8–6018 to the "handle" of the Frying Pan SNR morphology, which is where the supersonic pulsar and its bow-shock nebula are located (see Figure 8, left panel), can provide a better global fit to the data. The TS for a point source at the PWN/PSR position is TS = 39 with no evidence for extension. The placement of the γ-ray source with the bow-shock nebula, its spectral index $\Gamma = 2.76 \pm 0.16$ being similar to other Fermi–LAT PWNe, as well as considering the energetic nature of the bow-shock nebula (C. Y. Ng et al. 2012), all support a PWN classification, despite the lack of an identified TeV counterpart. An SNR component seems least likely considering the age of the system and the lack of molecular material observed in the region (C. Y. Ng et al. 2012). We consider this a likely PWN, but we cannot rule out a pulsar contribution.

G327.15–1.04. The first MeV–GeV detection of this source was reported in Y. Xiang et al. (2021). The γ-ray emission is detected at $>4\sigma$ significance with the Fermi–LAT between 300 MeV and 2 TeV and is best characterized with photon index $\Gamma = 2.45 \pm 0.13$ (J. Eagle et al. 2022). There is $>2\sigma$ significance for curvature, consistent to both J. Eagle et al. (2022) and the

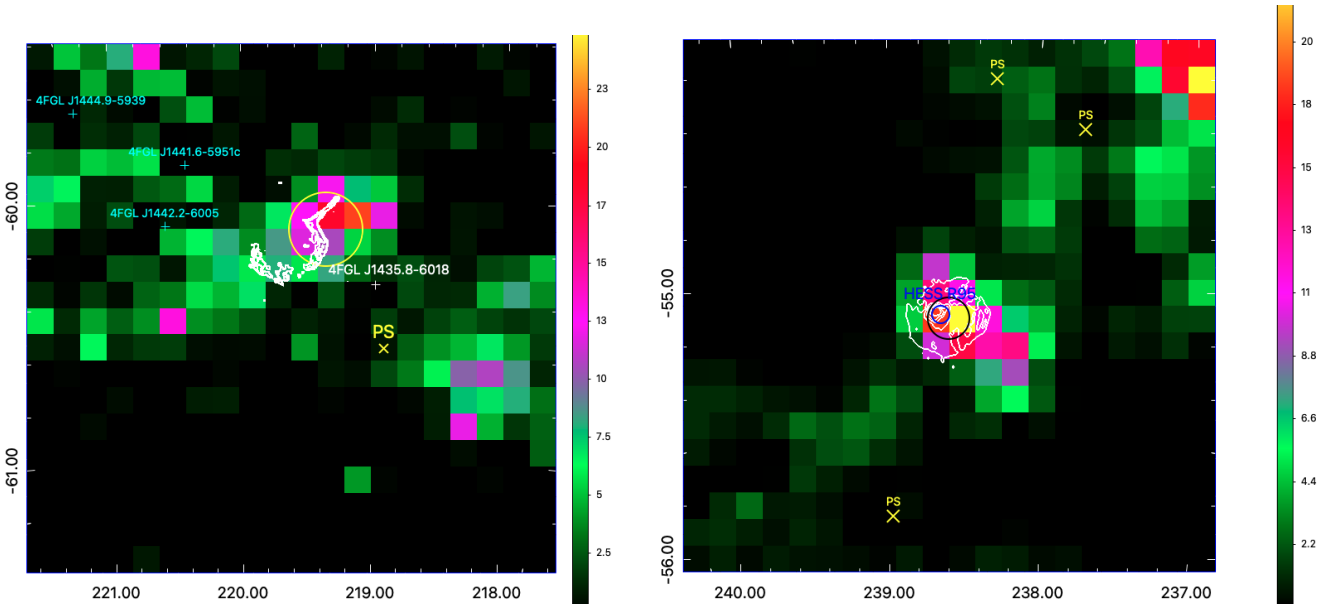

Figure 8. Left panel: a 2° × 2° 300 MeV–2 TeV TS map of PSF3 events for PWN G315.78–0.23. There is one possibly associated Fermi–LAT source, 4FGL J1435.8–6018. The 95% uncertainty region of the new best-fit position of 4FGL J1435.8–6018 is the yellow circle, which coincides with the "handle" of the Frying Pan radio morphology. The "handle" consists of the supersonic pulsar and the trailing PWN. The yellow cross labeled "PS" represents the addition of a point source to model residual emission unrelated to the SNR. The second unrelated point source (see the text) is just out of view to the west. Unrelated nearby 4FGL sources are labeled in cyan. The maximum TS at the PWN/SNR position is ∼21. Right panel: a 2° × 2° 1–10 GeV TS map of ALL events centered on SNR G327.15–1.04 (denoted by 843 MHz radio contours in white) accompanied by the 95% confidence regions for the TeV PWN HESS J1554–550 (blue) and for a point source modeling the residual MeV–GeV emission (black). The maximum TS at the PWN/SNR position is ∼23 in the 1–10 GeV energy range.

4FGL–DR3. A detailed multiwavelength investigation of the associated emission was carried out (J. Eagle et al. 2022), where the pointlike MeV–GeV γ-ray emission is consistent with a PWN origin from G327.15–1.04, supported by its TeV counterpart HESS J1554–550. The position, extent, and energetics of the system favor a PWN origin. A 1–10 GeV TS map demonstrating the source detection is displayed in Figure 8 (right panel). While the current IC model predictions (J. Eagle et al. 2022) can characterize well the MeV–TeV emission for PWN G327.15–1.04, there remains uncertainty in the properties of ambient photon fields in addition to physical properties of the system (i.e., true age, maximum particle energy, energy break in particle spectrum, etc.) that influence the IC shape. Moreover, the central pulsar remains undetected at any wavelength, such that a MeV–GeV pulsar contribution cannot be reliably ruled out, but the TeV PWN counterpart supports a high-energy PWN contribution to the Fermi–LAT data.

G332.50–0.30 (RCW 103) and G332.50–0.28. RCW 103 is observed as a ∼5′ X-ray SNR shell with an inner PWN by Chandra (K. A. Frank et al. 2015). A second X-ray PWN powered by the pulsar J1617–5055 is positionally coincident with the Fermi–LAT source, 4FGL J1616.2–5054e, which is characterized as a radial disk with $r = 0.^{\circ}32$ in the 4FGL (J. Lande et al. 2012; S. Abdollahi et al. 2022). We report extension results for this source using a radial Gaussian template with $r = 0.^{\circ}31$ and an offset position that is closer to both PWNe (see Figure 9, left panel). The PWN associated with PSR J1617–5055 is ∼1′ in length observed in X-rays (O. Kargaltsev et al. 2009), while RCW 103 is ∼10′ in size (K. A. Frank et al. 2015). The two systems are only $0.^{\circ}02$ from one another in location, making it impossible to distinguish the more likely γ-ray emitter. The TeV counterpart, HESS J1616–508, is notably smaller and closer to PSR J1617–5055 than to RCW 103. The best-fit spectral index for the GeV source is $\Gamma = 1.98 \pm 0.03$, which is comparable to the TeV index $\Gamma = 2.32 \pm 0.06$ (H. E. S. S. Collaboration et al. 2018; see also Figure 9, right panel). It seems probable that the origin of the GeV and TeV emission is from one or both PWNe (M. Ackermann et al. 2017), in which case we still consider the extended source 4FGL J1616.2–5054e a likely Fermi–LAT PWN, while noting that there is potentially more than one X-ray counterpart. Future high-energy studies should explore this region further.

G336.40+0.10. HESS J1632–478 was first discovered as an extended (∼12′) unidentified TeV source (F. Aharonian et al. 2006). An X-ray PWN was subsequently identified by XMM-Newton observations as a point source accompanied by faint, diffuse nonthermal X-ray emission extending outward ∼32″ in size (M. Balbo et al. 2010). The X-ray nebula is in positional coincidence with the H.E.S.S. emission in addition to possible extended GeV emission. The X-ray, GeV, and TeV extended emission favor a PWN scenario. In the Fermi–LAT catalogs, the extended GeV emission corresponding to 4FGL J1631.6–4756e is fit as a radial disk with $r = 0.^{\circ}25$ (M. Ackermann et al. 2017; J. Ballet et al. 2020). Reanalysis of the Fermi–LAT emission concludes that a radial Gaussian template of size $r = 0.^{\circ}19$ can significantly improve the fit. HESS J1632–478 is $\sim 0.^{\circ}21$ in size (H. E. S. S. Collaboration et al. 2018), in good agreement with the extension we find. The TeV spectral index $\Gamma = 2.52 \pm 0.06$ and the spectral index measured by Fermi–LAT $\Gamma = 2.05 \pm 0.04$ also connect well, encouraging a single origin (see Figure 10, left panel). Since it is highly likely the GeV source is the counterpart of the TeV PWN, we classify 4FGL J1631.6–4756e as a likely Fermi–LAT PWN.

4.3.2. New PWN Candidates

G11.03–0.05, G11.09+0.08, and G11.18–0.35. G11.03–0.05 and G11.09+0.08 are two uncertain SNR/PWN candidates. Both were first identified in C. L. Brogan et al. (2004) using Very Large

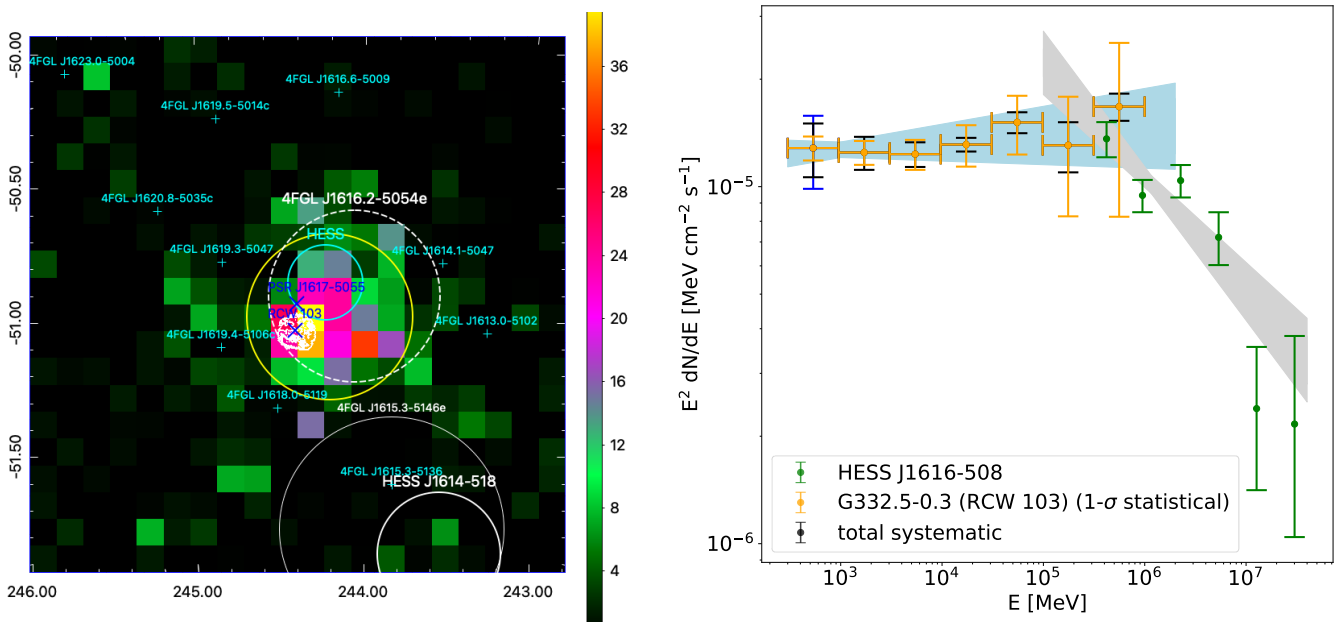

Figure 9. Left panel: a 2° × 2° 10 GeV–2 TeV TS map of PSF3 events for both X-ray PWNe coincident with the Fermi–LAT PWN 4FGL J1616.2–5054e: G332.50–0.30 (RCW 103, with Chandra X-ray contours in white) and G332.50–0.28 (PSR J1617–5055). 4FGL J1616.2–5054e is indicated as the white dashed circle but is not included in the source model. The best fit for the extended emission is marked as a yellow circle. HESS J1616–518 is the cyan circle. The maximum TS occurs between the two X-ray PWNe with value ∼50 for energies between 1 and 10 GeV. Right panel: the best-fit Fermi–LAT spectral model (blue band) and data in yellow for the extended source coincident with both PWN G332.50–0.30 (RCW 103) and G332.50–0.28 (J1616.2–5054e) beside the best-fit spectral model (gray band) and data in green of its TeV counterpart HESS J1616–508 from H. E. S. S. Collaboration et al. (2018). The blue flux error for $E < 1$ GeV is the additional systematic error as discussed in Section 3.6.

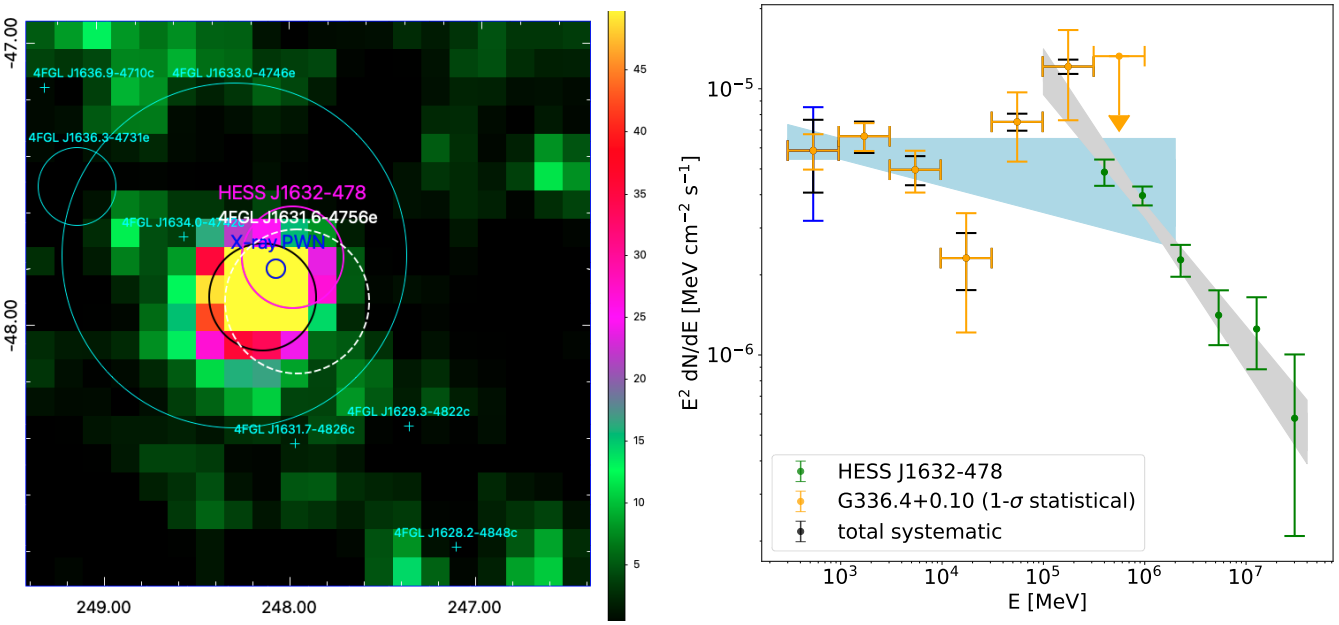

Figure 10. Left panel: a 2° × 2° 1–10 GeV TS map of PSF3 events for PWN G336.40+0.10. Note that 4FGL J1631.6–4756e is indicated but not included in the source model. The best-fit radial Gaussian template for the extended emission is the black circle. The X-ray PWN location and extent are marked with a blue circle, and the TeV PWN counterpart HESS J1632–478 is in magenta. The maximum TS at the PWN position is ∼109 for energies between 1 and 10 GeV. Unrelated 4FGL sources are labeled in cyan. Right panel: the best-fit spectral model (blue band) and data in yellow for J1631.6–4756e (PWN G336.40+0.10) beside the best-fit spectral model (gray band) and data in green for its TeV counterpart HESS J1632–478 from H. E. S. S. Collaboration et al. (2018). The blue flux error for $E < 1$ GeV is the additional systematic error, as discussed in Section 3.6.

Array (VLA) observations at 1465 MHz along with the Giant Metrewave Radio Telescope (GMRT) at 235 MHz. G11.18–0.35 belongs to the composite SNR G11.2–0.3 (the "Turtle") and is powered by pulsar PSR J1811–1925. The two SNR candidates, G11.03–0.05 and G11.09+0.08, in addition to their neighbor, SNR G11.2–0.3, are indicated by plotting their VLA radio contours in both panels of Figure 11. All three plerionic SNRs are coincident in location with an unidentified extended 4FGL source J1810.3–1925e. A second point source is additionally coincident with G11.2–0.35 (see Figure 11, right panel). In our analysis of the

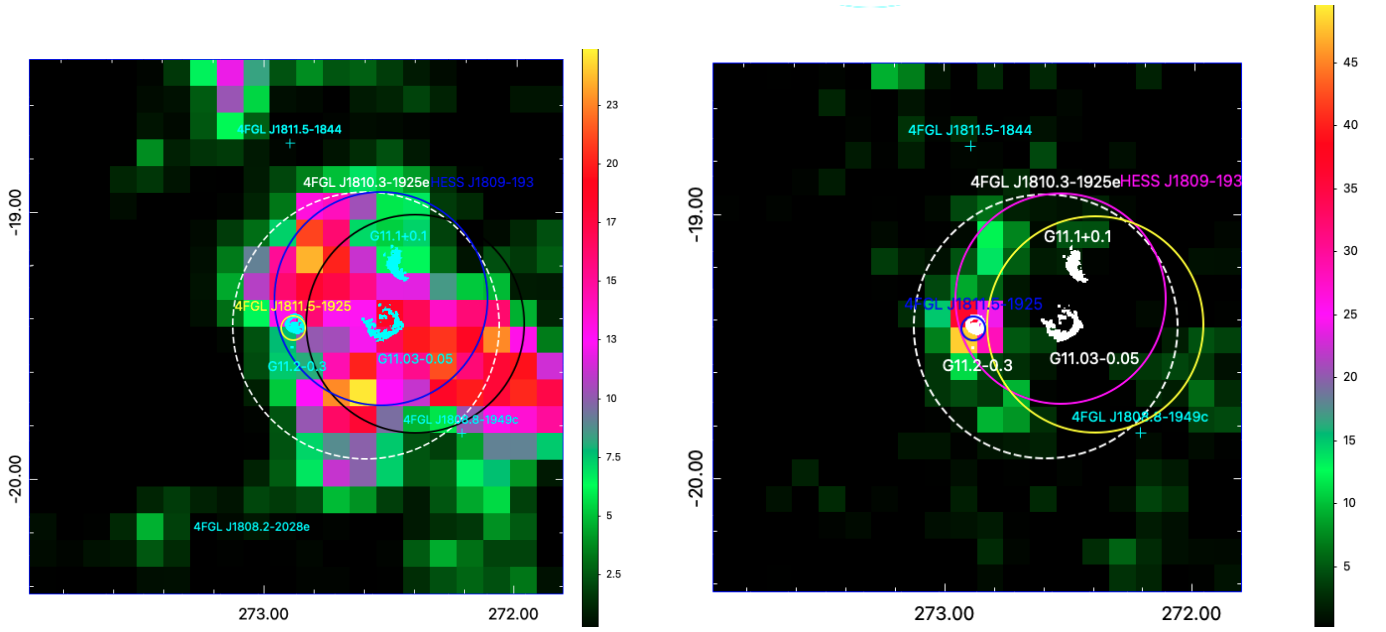

Figure 11. Left panel: a 2° × 2° 1–10 GeV TS map of PSF3 events for plerionic SNRs G11.03–0.05 and G11.09+0.08 (denoted by radio contours in cyan). G11.2–0.3 is also plotted with its radio contours and is coincident with 4FGL J1811.5–1925. An unidentified, extended TeV source HESS J1809–193 is coincident with all three PWNe, displayed in blue. Note that 4FGL J1810.3–1925e is indicated but not included in the source model. The best-fit radial Gaussian template for the extended emission is the black circle (yellow in the right panel). The maximum TS is ∼25 in the 1–10 GeV energy range. Right panel: a 2° × 2° 300 MeV–2 TeV TS map for PWN G11.18–0.35. The 95% uncertainty region for 4FGL J1811.5–1925 (blue circle) is coincident with the radio position of SNR G11.2–0.3 (radio contours in white). Unidentified HESS J1809–193 is displayed as the magenta circle with radius $r = 0.^{\circ}4$. The maximum TS at the PWN/SNR position is TS ∼48. In both panels, unrelated 4FGL sources in the field of view are labeled in cyan.

Fermi–LAT data, we tested for multiple point sources replacing 4FGL J1810.3–1925e, but one extended Fermi–LAT source is clearly required with only one additional point source, 4FGL J1811.5–1925. The extended source is required to model significant extended γ-ray emission, though with a location offset from 4FGL J1811.5–1925 and G11.2–0.35, and is fit as a radial Gaussian, $r = 0.^{\circ}41$. For comparison, the 4FGL catalogs model the extended emission as a radial disk with $r = 0.^{\circ}5$, such that the extension encapsulates all three SNRs (M. Araya 2018). With the new template and location, 4FGL J1810.3–1925e is found to overlap with the PWN candidates G11.09+0.08 and G11.03–0.05, and the unidentified TeV source HESS J1809–193 that has a Gaussian extension $r = 0.^{\circ}40$ (H. E. S. S. Collaboration et al. 2018).

It is possible that the coincident Fermi–LAT and TeV extended emission originate from one or both G11.03–0.05 and G11.09+0.08 PWN candidates. It is probable that 4FGL J1811.5–1925 is associated with G11.18–0.35. HESS J1809–193 may be unidentified, but it has spectral properties consistent with a PWN origin ($\Gamma = 2.38 \pm 0.07$; H. E. S. S. Collaboration et al. 2018). Both G11.03–0.05 and G11.09 +0.08 are therefore considered possible PWN radio counterparts to the extended GeV emission reported here.

Due to the crowded region, it is difficult to systematically characterize the J1810.3–1925e spectrum (see Figure 2). The uncertain nature of 4FGL J1810.3–1925e is indicated with the flags 3, 5, and 6 in the 4FGL (J. Ballet et al. 2023). Flag 3 corresponds to the source flux changing with another model or analysis by more than 3σ. Flag 5 indicates that the region is confused with a nearby brighter neighbor. Flag 6 indicates an interstellar gas clump may be coincident, and thus is labeled with the "c" identifier, signifying that the 4FGL source is a candidate in nature, and may actually be part of the Galactic diffuse background. For this reason, the systematic study performed in this work cannot be applied to this source, as it relies on the use of alternative background models. Understanding the true nature of the Fermi–LAT extended source emission with respect to the background is required.

4FGL J1811.5–1925 is best fit as a power law with $\Gamma = 2.03 \pm 0.01$ and is coincident with the position of the young and energetic SNR G11.2–0.3. The radio-quiet central pulsar, PWN, and host SNR are detected in X-ray (K. K. Madsen et al. 2020). The SNR shell exhibits nonthermal X-ray emission, which suggests evidence for efficient particle acceleration of electrons to multi-TeV energies (K. K. Madsen et al. 2020). Both the 4FGL catalogs (J. Ballet et al. 2023) and H. E. S. S. Collaboration et al. (2018) classify the 4FGL source a pulsar candidate. The 4FGL finds significant curvature of the source spectrum, but this may depend on the location of J1810.3–1925e with respect to J1811.5–1925. The young age and the energetic nature of the pulsar, PWN, and SNR shell require a broadband investigation to determine the most probable scenario of the observed γ-ray emission.

G12.82–0.02. G12.82–0.02 is a composite SNR housing the central pulsar J1813–1749 that powers the nebula. The source was first detected in the TeV band as HESS J1813–178 (F. Aharonian et al. 2005) and later identified as a PWN after being identified in radio and X-ray (C. L. Brogan et al. 2005). The TeV PWN is extended $r = 0.^{\circ}04$ and is consistent with the full extent of the SNR shell $r \sim 0.^{\circ}025$ in radio (H. E. S. S. Collaboration et al. 2018). An extended Fermi–LAT source, 4FGL J1813.1–1737e overlaps in location, but exhibits a much larger extension $r = 0.^{\circ}6$ as a radial disk in the 4FGL catalogs (M. Araya 2018; J. Ballet et al. 2023). The extended emission can be better fit with a source closer to the SNR position and modeled as a radial Gaussian and similar extent ($r = 0.^{\circ}41$; see Figure 12, left panel). The larger extension in the GeV band

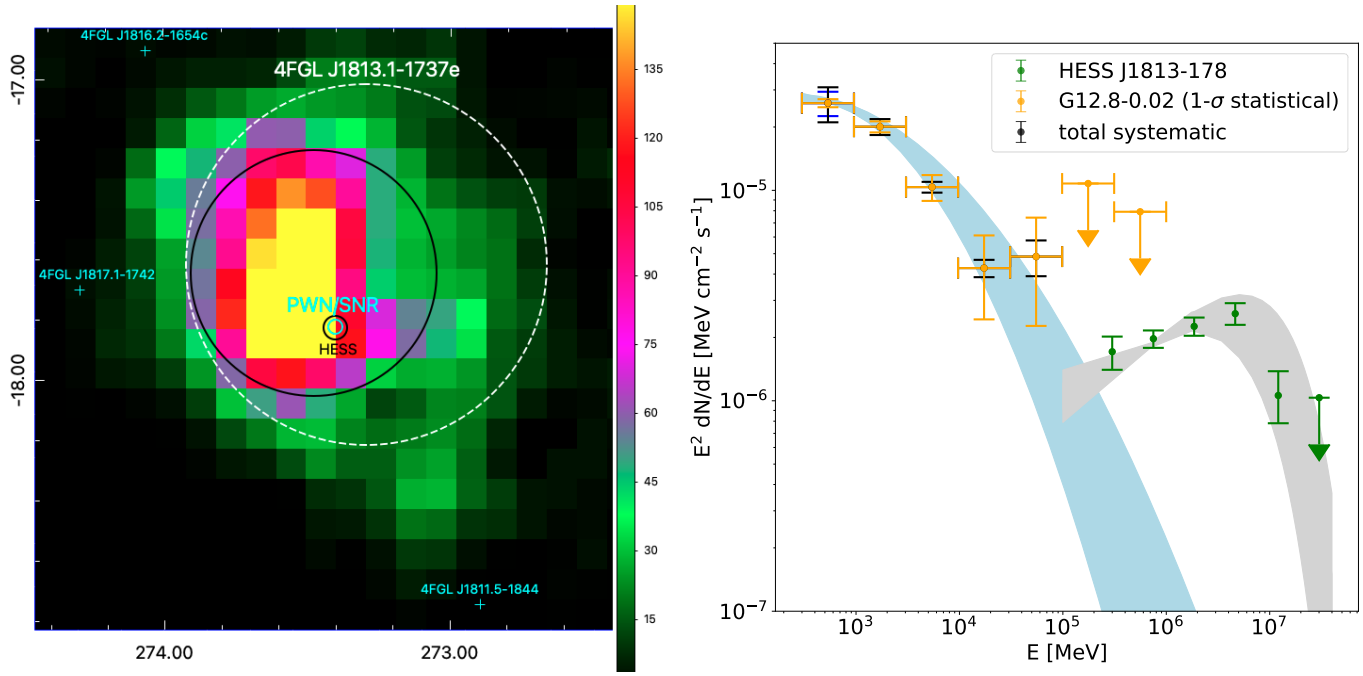

Figure 12. Left panel: a 2° × 2° 1–10 GeV TS map of PSF3 events for PWN G12.82–0.02. The SNR shell is ∼3′ in diameter (cyan circle), which embodies PSR J1813–1749 and the X-ray PWN. The TeV PWN HESS J1813–178 location and size are marked in black. The 4FGL J1813.1–1737e position and extent are indicated by the white dashed circle but are not included in the source model. The best-fit position and extent of the radial Gaussian template are indicated by the larger black circle. The maximum TS is ∼194. Right panel: the best-fit Fermi–LAT spectral model (blue band) and data are shown in yellow for the extended source coincident with PWN G12.82–0.2 (J1813.1–1737e) beside the best-fit spectral model (gray band) and data in green of its TeV counterpart HESS J1813–178 from H. E. S. S. Collaboration et al. (2018). The blue flux error for $E < 1$ GeV is the additional systematic error, as discussed in Section 3.6.

compared to the X-ray and TeV morphologies is notably different, as well as the GeV and TeV spectral shapes (see Figure 12, right panel), indicating multiple source contributions are present. Recently, T. Wach et al. (2023) found compelling evidence that the H.E.S.S. emission has more than one contributing component, such that it can be decomposed into a compact Gaussian component (*A*) and a halo-like diffuse component (*B*). The authors concluded that the compact source should be the TeV PWN counterpart, while the halo-like diffuse component is reasonably associated with 4FGL J1813.1–1737e.

G15.40+0.10. The radio shell of SNR G15.40+0.10 is coincident with the X-ray position and size (∼0.°1) of a PWN, making it a composite SNR. The source is also detected in TeV as pointlike HESS J1818–154 and HAWC J1819–150.[81] The H.E.S.S. emission is classified as a composite SNR and may have contribution from both the SNR shell and the PWN (L. Supan et al. 2015). An unknown 4FGL source J1818.6–1533 is coincident with G15.40+0.10. A reanalysis of the γ-ray emission finds evidence for extension $TS_{ext} = 20.6$ using a radial Gaussian template, $r = 0.°19$ (see Figure 13, left panel). The TeV spectral index $\Gamma = 2.21 \pm 0.15$ is similar to the GeV spectral index 2.65 ± 0.07 (H. E. S. S. Collaboration et al. 2018), though the GeV spectrum indicates a softer spectrum with curvature (Table 5). No pulsar is yet identified, but there is observational evidence suggesting molecular interactions with the SNR shell that may at least partially explain the high-energy emission (H. E. S. S. Collaboration et al. 2014; L. Supan et al. 2015).

G18.90–1.10. G18.90–1.10 is a likely PWN based on Chandra X-ray observations of a possible point source accompanied by an extended nebula that is ∼8′ in size (R. Tüllmann et al. 2010). The central pulsar has not been detected. The larger SNR shell is nearly 0.°5 in size in radio (R. Tüllmann et al. 2010). An unidentified source 4FGL J1829.4–1256 is coincident in position to the X-ray PWN (see Figure 13, right panel). Given the observed γ-ray emission is pointlike, localized well within the SNR radio shell, and has a log parabola spectral index $\Gamma = 1.46 \pm 0.24$, we classify this source as a PWN candidate, depending on confirming the X-ray counterpart as a PWN, though it is possible the central pulsar may have some contribution to the observed γ-ray emission.

G20.20–0.20. While the central pulsar has not been identified, the SNR shell and PWN are detected in X-ray, where the SNR morphology is probably the result of the shell interacting with ambient molecular clouds (MCs; A. Petriella et al. 2013). A thermal component to the diffuse X-ray emission in the center of the SNR shell is not identified; instead, the overlapping nonthermal radio nebula favors a synchrotron origin such as a PWN (R. H. Becker & D. J. Helfand 1985; A. Petriella et al. 2013). An unidentified 4FGL source 4FGL J1828–1133 coincides with the entire SNR system (see Figure 14, left panel). It is likely the source is associated with the PWN/SNR system in some way, but because the SNR may be interacting with its surroundings, a detailed analysis considering the broadband properties will be required to determine the most likely origin between the central pulsar, PWN, and SNR. The best-fit spectrum is curved with a spectral index $\Gamma = 2.27 \pm 0.13$ at 1 GeV, favoring an SNR or pulsar origin.

[81] The HAWC counterpart is possibly contaminated by a close neighbor; see A. U. Abeysekara et al. (2017).

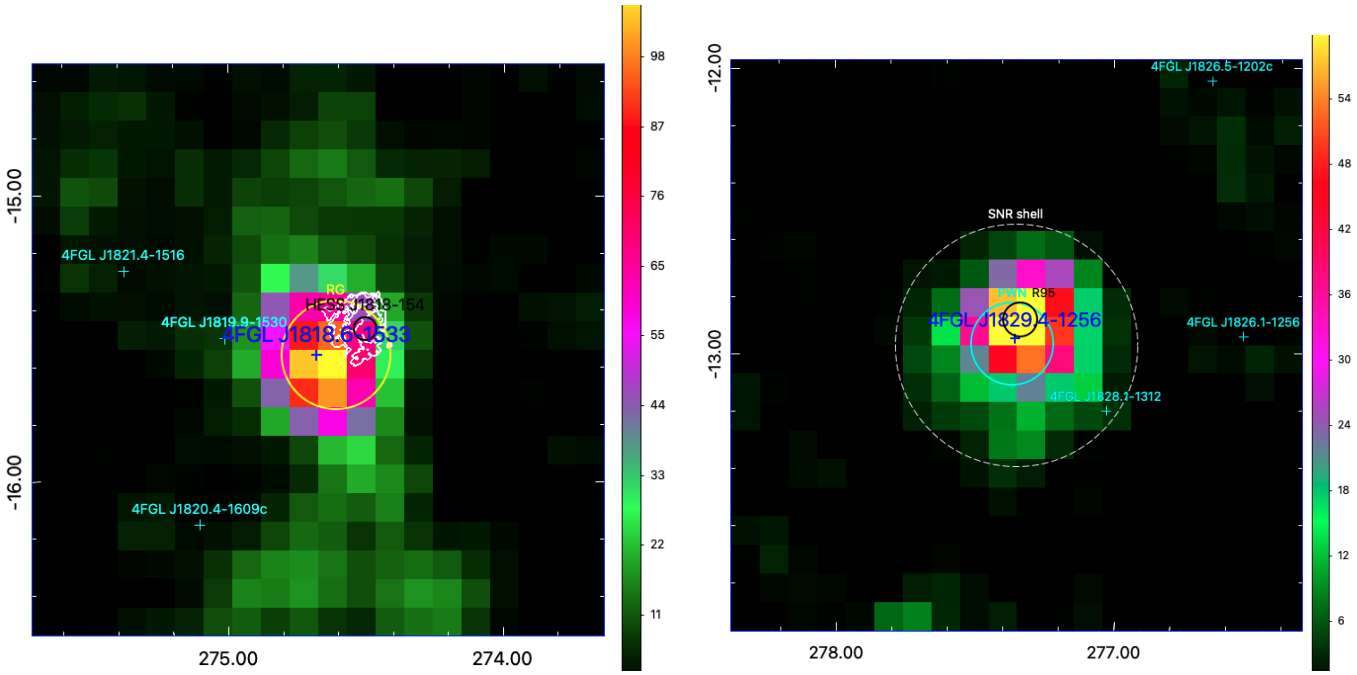

Figure 13. Left panel: a 2° × 2° 1–10 GeV TS map of PSF3 events for PWN G15.40+0.10. The Gaussian extent of 4FGL J1818.6–1533 is in yellow. The white contours represent the radio SNR. HESS J1818–154 is located at the PWN near the core of the SNR shell in black. The maximum TS at the PWN/SNR position is ∼110. Right panel: a 2° × 2° 1–10 GeV TS map for PWN G18.90–1.10. The location and size of the radio PWN are represented as a cyan circle. The white dashed circle corresponds to the size of the SNR shell in radio. The 95% positional uncertainty region for a point-source modeling emission associated with 4FGL J1829.4–1256 is marked as a black circle. The maximum TS at the PWN position is ∼78. Unrelated 4FGL sources are indicated in cyan.

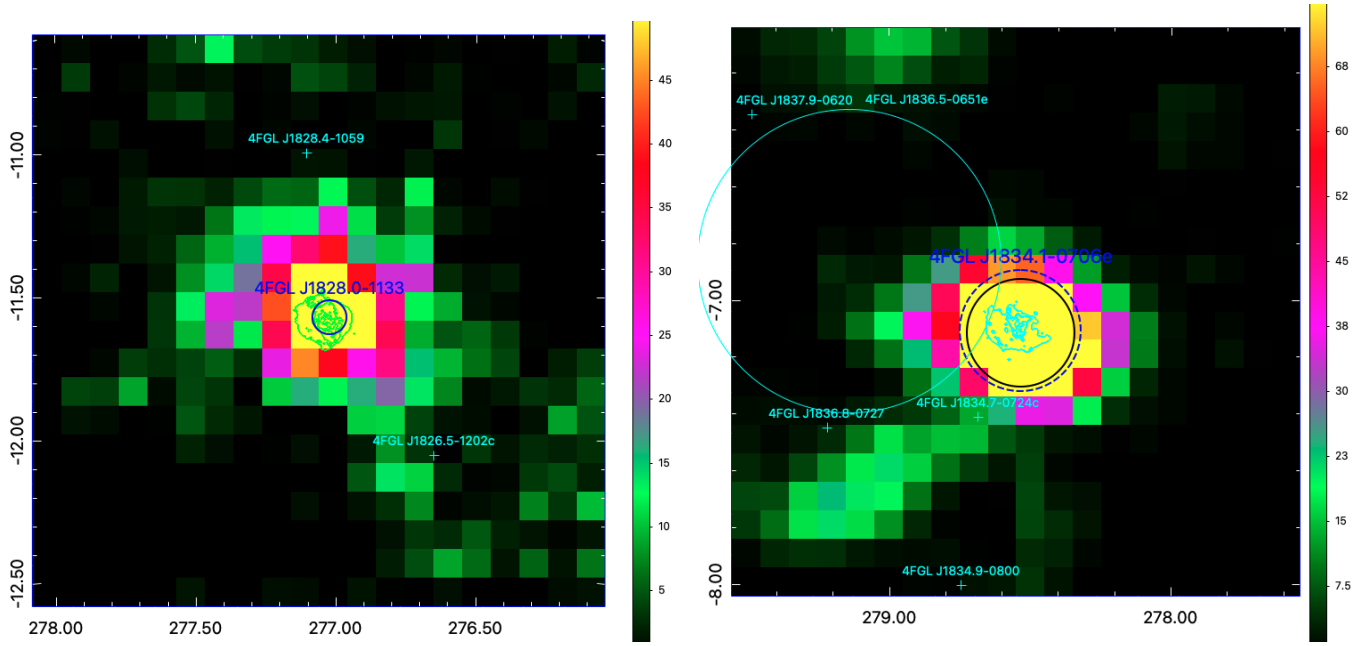

Figure 14. Left panel: a 2° × 2° 300 MeV–2 TeV TS map of PSF3 events for PWN G20.20–0.20. The 95% uncertainty region for the coincident source 4FGL J1828.0–1133 is in blue. The green contours represent the radio SNR, and the central peak corresponds to the PWN. The maximum TS at the PWN/SNR position is ∼88. Right panel: a 2° × 2° 1–10 GeV TS map for PWN G24.70+0.60. The 4FGL J1834.1–0706e position and extent are indicated by the blue dashed circle but are not included in the source model. The best-fit position and extent of the radial Gaussian template are indicated by the black circle. The cyan contours represent the Crab-like SNR in radio. The maximum TS at the PWN/SNR position is ∼204. Unrelated 4FGL sources are indicated in cyan.

G24.70+0.60. This Crab-like SNR is observed as a bright, centrally peaked core roughly ∼3′ in size and is encompassed by an incomplete shell with size ∼30′ in radio at 20 cm (R. H. Becker & D. J. Helfand 1987). The central pulsar is not known, but the radio morphology and spectral properties strongly suggest a PWN origin given the flat radio spectrum and linear polarization from the core (R. H. Becker & D. J. Helfand 1987). A Fermi–LAT source 4FGL J1834.1–0706e is positionally coincident with G24.70+0.60 of similar size and is classified as an SNR in the 4FGL catalogs (J. Ballet et al. 2023). Prior work has argued an SNR origin based on the possible association of a nearby extended TeV

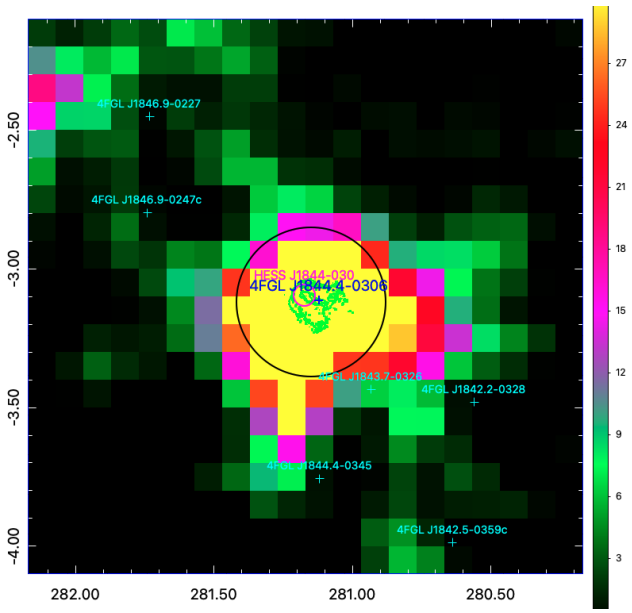

Figure 15. A 2° × 2° 1–10 GeV TS map of PSF3 events for PWN G29.40 +0.10. The best-fit position and extent of the Gaussian source 4FGL J1844.4–0306 are shown in black. The green contours represent the SNR in radio. The UNID HESS J1844–030 is marked in magenta. The maximum TS at the PWN/SNR position is ∼67. Unrelated 4FGL sources are indicated in cyan.

source, MAGIC J1835–069 (M. Ackermann et al. 2017; MAGIC Collaboration et al. 2019), motivated by similar spectral indices and the possibility of the SNR shell interacting with denser material. The best-fit spectral index characterizing the γ-ray emission is $\Gamma = 2.02 \pm 0.04$ for 4FGL J1834.1–0706e and $\Gamma \sim 2.75$ for MAGIC J1835–069 (MAGIC Collaboration et al. 2019). It is argued that CRs accelerated by the SNR shell diffuse and illuminate a nearby cloud coincident with the TeV emission. Other investigations into the region favor a star-forming region origin (e.g., J. Katsuta et al. 2017). While it is possible the GeV and TeV sources are associated, we question an SNR origin since the SNR shell is not firmly detected at any wavelength, whereas the polarized, centrally peaked radio core is and possibly suggests a PWN origin instead. The source 4FGL J1834.1–0706e is modeled as a radial disk with $r = 0.^{\circ}21$ in 4FGL, and we find the extended emission is fit marginally better as a radial Gaussian with $r = 0.^{\circ}19$ (see Figure 14, right panel). The region is complex in more than just the Fermi–LAT band, which prevents a reliable classification of this source. It seems plausible that the PWN is at least partially contributing to the observed γ-ray emission, but a deeper analysis considering multiwavelength data of the region is needed.

G29.40+0.10. This is a possible composite SNR identified in radio, X-ray, GeV, and TeV energies (A. Petriella 2019). The radio observations suggest the SNR is expanding into a nonuniform medium and the X-ray observations show a morphology and spectrum suggestive of a PWN origin with an embedded point source that may be the central pulsar. An unknown 4FGL source J1844.4–0306 is found in the location of the SNR and PWN. We find evidence for extension $TS_{ext} = 18.8$ for a Gaussian template with $r = 0.^{\circ}27$ (see Figure 15). The TeV counterpart HESS J1844–030 is unidentified and pointlike, having a spectral index $\Gamma = 2.48 \pm 0.12$ (H. E. S. S. Collaboration et al. 2018). The GeV spectral index is similarly soft, $\Gamma = 2.55 \pm 0.06$, indicating a common origin. A PWN scenario can plausibly explain the TeV emission. Recent work (D. Zheng et al. 2023) reports either a hadronic or a leptonic scenario for the TeV emission is possible, while a hadronic component is most likely for the GeV.

G49.20–0.30 and G49.20–0.70 (W51 C). The SNR W51 C or G49.2–0.7 is located near a star-forming region and houses a pulsar candidate CXO J192318.5+140335 with compact X-ray emission observed by Chandra (core ∼1′; B.-C. Koo et al. 2005). Observations performed by XMM-Newton reveal a second PWN candidate in the SNR, which has a similar extent to the other PWN, G49.20–0.30 (M. Sasaki et al. 2014). The W51 C SNR has a radio diameter $\sim 1.^{\circ}0$ and is the basis for modeling Fermi–LAT extended γ-ray emission in the region coincident with this system. It was shown that the SNR is likely the γ-ray emitter with compelling evidence for hadronic CR acceleration and an extension roughly consistent to the radio SNR size (T. Jogler & S. Funk 2016). 4FGL J1923.2 +1408e represents the SNR emission as an elliptical disk with radii $0.^{\circ}375$ and $0.^{\circ}26$ (see the left panel of Figure 16; A. A. Abdo et al. 2009; J. Ballet et al. 2020). The extended TeV source first discovered by H.E.S.S. (F. Feinstein et al. 2009) and subsequently detected by MAGIC (J. Aleksić et al. 2012) is identified as an interaction between the SNR and the surrounding MCs, similar to the GeV emission (T. Jogler & S. Funk 2016). The spectra for the Fermi–LAT and MAGIC SNR counterparts show agreement above ∼3 GeV, with a spectral index $\Gamma_\gamma \sim 2.5$. The spectral index below ∼3 GeV is harder: $\Gamma_\gamma \sim 2.1$. In the 4FGL–DR4, the SNR is characterized with a log parabola spectrum with an index ∼2.2 at 2.7 GeV.

Based on the smaller TeV extension $0.^{\circ}12$ compared to the SNR size observed in the GeV and radio bands, as well as its compelling overlap with both of the PWN candidates G49.20–0.70 ("PWNc 1") and G49.20–0.30 ("PWNc 2"), a PWN contribution is plausible. Furthermore, as shown in the left panel of Figure 16, there is significant TS ∼2 5 residual emission coincident with both PWN candidates not accounted for by 4FGL J1923.2+1408e or the background components. We find that 4FGL J1923.2+1408e is required to model extended emission in the region, but that 4FGL J1922.7 +1428c is the likely counterpart to G49.20–0.30, and is therefore removed from the global source model. Two point sources are tested, each fixed at the PWN X-ray positions. The addition of these two sources significantly improves the fit over the 4FGL model ($TS = 2 \log \frac{L_{2ps}}{L_{4FGL}} = 166$) and over a single additional extended source ($TS = 2 \log \frac{L_{2ps}}{L_{1ext}} = 99$) that is localized. G49.20–0.30 ("PWNc 2") results in a point source detection TS = 157.2 with a log parabola spectral index $\Gamma = 2.35 \pm 0.06$. "PWNc 1" or G49.20–0.70 is detected with TS = 28.0 and has a power-law spectral index $\Gamma = 2.38 \pm 0.09$. We therefore classify the two new point sources (replacing 4FGL J1922.7+1428c) as tentative PWN detections. A deeper analysis considering multiwavelength information is needed to determine the capacity for either PWN candidate to emit γ-rays, as it is possible that one or both sources may be components of the SNR.

G63.70+1.10. G63.70+1.10 is the central PWN to SNR G63.7+1.1, though the central pulsar remains unknown. X-ray observations revealed a point source embedded within a diffuse nonthermal X-ray nebula, which coincides with the

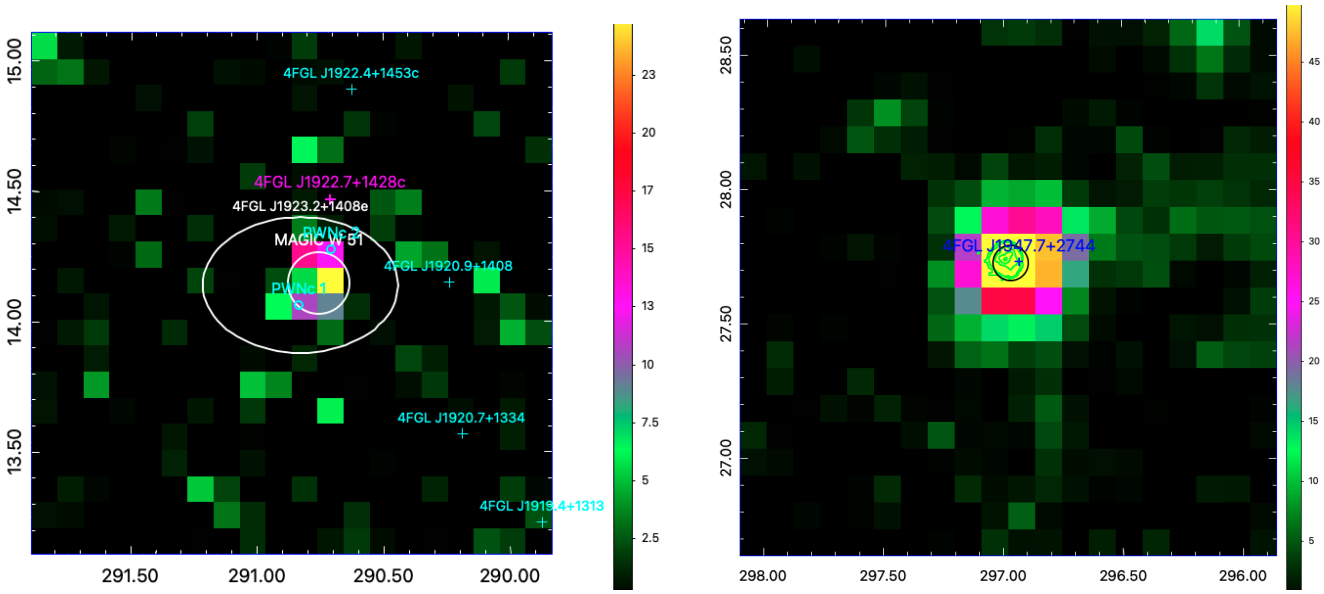

Figure 16. Left panel: a 2° × 2° 10 GeV–2 TeV TS map of PSF3 events for PWN candidates G49.20–0.70 ("PWNc 1") and G49.20–0.30 ("PWNc 2"), both overlapping SNR W 51C. The SNR is the GeV emitter 4FGL J1923.2+1408e. 4FGL J1922.7+1428c is the Fermi–LAT counterpart, replaced by the two point sources at the PWN locations. The TeV SNR is the inner white circle, which overlaps spatially with both PWN candidates. The maximum TS is ∼25 for $E > 10$ GeV. Right panel: a 2° × 2° 300 MeV–2 TeV TS map of PSF3 events for PWN G63.70+1.10. There is one associated Fermi–LAT source 4FGL J1947.7 +2744. Radio contours of the SNR shell and the central PWN are indicated in green. The 95% positional uncertainty for the point source is indicated in black. The maximum TS at the PWN/SNR position is ∼66.

bright radio core of the SNR ∼8′ in diameter (H. Matheson et al. 2016). The PWN has a possible Fermi–LAT association 4FGL J1947.7+2744. Reanalysis of the region confirms that there is pointlike γ-ray emission in the vicinity of the PWN/SNR system (see Figure 16, right panel). We consider the source association tentative for the PWN. This is motivated by the SNR being located among dense material and possibly interacting with local clouds (H. Matheson et al. 2016). Considering the spectral properties of the γ-ray source such as its best-fit photon index $\Gamma = 1.84 \pm 0.22$, and the age of the system ($\tau \gtrsim 8$ kyr; H. Matheson et al. 2016), it seems equally likely for the pulsar, PWN, or the SNR to be the Fermi–LAT counterpart.

G65.73+1.18. This source is another Crab-like PWN with an identified TeV counterpart. NuSTAR and Chandra observations revealed a presumed pulsar located at the emission peak of a compact X-ray nebula within a radius $r \sim 20''$, overlapping in location with the previously unknown TeV source 2HWC J1953+294 (shown in Figure 17, left panel; A. Coerver et al. 2019). A spectral index ∼2.0 characterizes X-ray emission from 2–20 keV with no apparent spectral cutoff, and the 2–10 keV luminosity is $\approx 10^{31}$ erg s^{-1}, similar to the 1–30 TeV luminosity. The TeV emission has no evidence for extension observed by HAWC, but the VERITAS counterpart VER J1952+293 has a Gaussian extension $r = 0.^{\circ}14$ (A. U. Abeysekara et al. 2018). The observed γ-rays from the Fermi–LAT, HAWC, and VERITAS suggest a PWN origin (A. U. Abeysekara et al. 2018). An unidentified Fermi–LAT source 4FGL J1952.8+2924 is plausibly the GeV counterpart due to positional coincidence (see Figure 17, left panel). The TeV counterpart's spectral index $\Gamma = 2.78 \pm 0.15$ (T. Linden et al. 2017) is somewhat softer than the log parabola GeV spectral index $\Gamma = 2.13 \pm 0.19$. VER J1952 +293 has a spectral index $\Gamma = 2.65 \pm 0.49$, but with fluxes that are lower than what is observed by HAWC (see Figure 18). This may be in part due to the different source sizes observed (for more details, see A. U. Abeysekara et al. 2018). We hence classify 4FGL J1952.8+2924 as a PWN candidate based on the similar position and energetics of the Crab-like SNR observed in each wave band; however, we cannot rule out a pulsar contribution.

G74.94+1.11. Also known as CTB 87, the SNR G74.9+1.2 has a filled center in X-ray with no identified shell, hosting PWN G74.94+1.11 and pulsar candidate CXOU J201609.2 +371110 (B. Guest et al. 2020). Note that 4FGL J2016.2 +3712 is coincident (see Figure 17, right panel). Pointlike TeV emission VER J2016+371 is a possible counterpart with a power-law spectral index $\Gamma_\gamma = 2.3 \pm 0.4$ (E. Aliu et al. 2014), similar to the Fermi–LAT index $\Gamma_\gamma = 2.24 \pm 0.41$. An SNR interaction with molecular material is possible (Q.-C. Liu et al. 2018) and recently, pulsations from CXOU J201609.2 +371110 (now PSR J2016+3711) are detected in radio (Q.-C. Liu et al. 2024). No pulsations in the γ-rays are found in Q.-C. Liu et al. (2024), but it is possible the Fermi–LAT emission may comprise contributions from both a pulsar at low energies and a PWN or SNR at high energies.

G328.40+0.20. This is a radio-bright Crab-like SNR that has a diameter ∼5′ (B. M. Gaensler et al. 2000). The PWN is also detected in X-ray with a size ∼1′ in diameter (J. D. Gelfand et al. 2007). Bright, extended GeV emission 4FGL J1553.8–5352e overlaps with the source region (M. Ackermann et al. 2017), characterized as a Gaussian, $r = 0.^{\circ}43$ (see Figure 19, left panel). An additional point source at the PWN location is tested, yielding TS ∼9. The extension and significant emission present above 20 GeV favors a PWN origin. A pulsar contribution is possible but not dominant. The large GeV extension compared to the radio PWN/SNR size, however, prevents a confident classification.

G337.20+0.10. Another crowded region in the Fermi–LAT sky, the plerionic SNR G337.2+0.1 may be contributing to the observed γ-ray emission. In X-ray, the SNR appears Crab-like with nonthermal emission forming a central peak, presumably

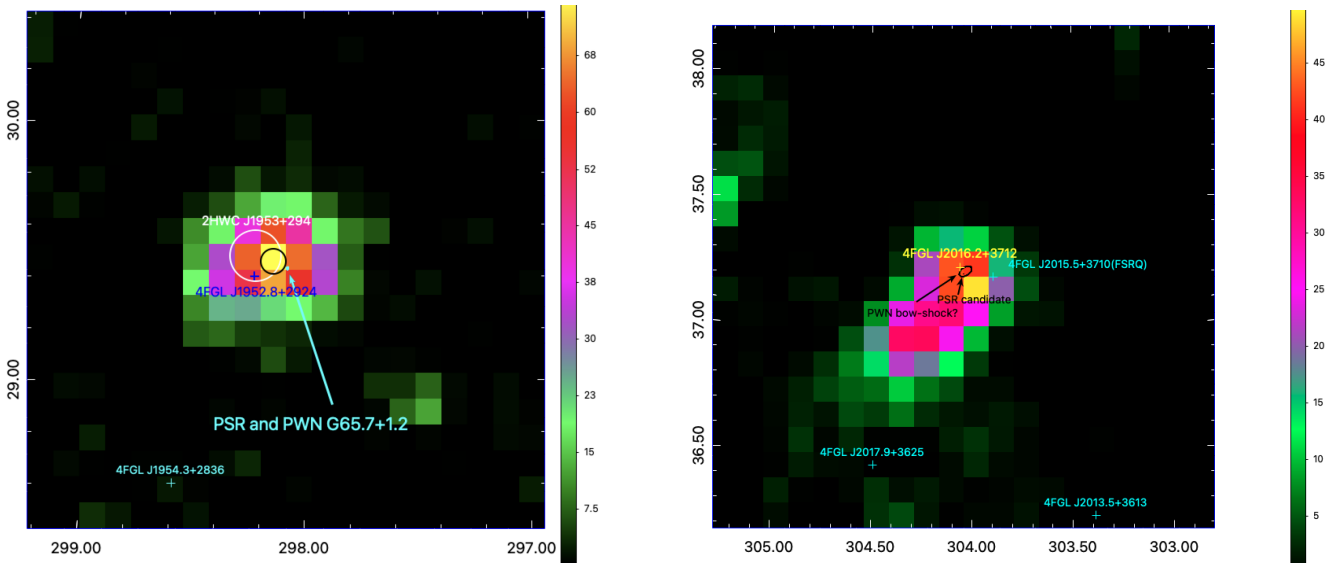

Figure 17. Left panel: a 2° × 2° 300 MeV–2 TeV TS map of PSF3 events for PWN G65.73+1.18. The pulsar and PWN in X-ray as observed by Chandra are denoted with cyan contours and are highlighted using the cyan arrow and label. The 95% uncertainty region of a point source at the PWN position is indicated in black and corresponds to the best-fit position of 4FGL J1952.8+2924. The maximum observed extension of the TeV PWN 2HWC J1953+294 is indicated in white. The maximum TS at the PSR/PWN position is ∼89. Right panel: a 2° × 2° 1–10 GeV TS map of PSF3 events for PWN G74.94+1.11. The Fermi–LAT counterpart 4FGL J2016.2+3712 is shown in yellow. The X-ray PSR and PWN position and extent are shown in black and highlighted using the black arrow. The maximum TS at the source position is ∼50. Unrelated 4FGL sources are indicated in cyan.

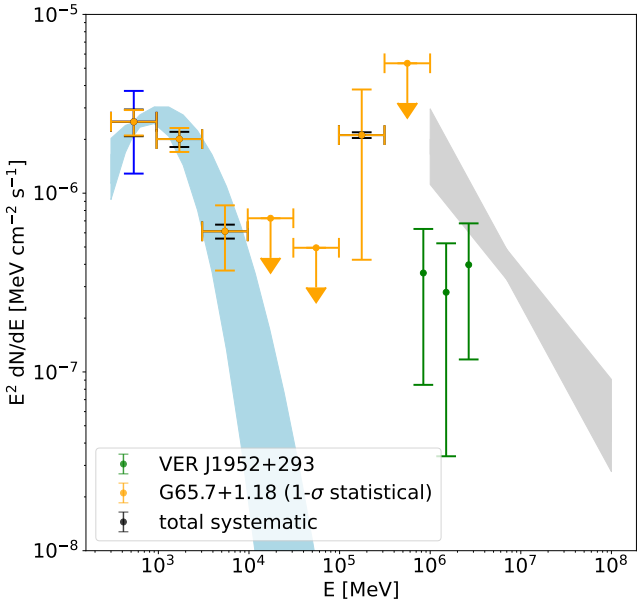

Figure 18. The best-fit Fermi–LAT spectral model (blue band) and data are shown in yellow for the source coincident with PWN G65.73+1.18 (J1952.8 +2924) beside the best-fit spectral model of 2HWC J1953+294 in gray, and the data of VER J1952+293 is in green (A. U. Abeysekara et al. 2018). The blue flux error for $E < 1$ GeV is the additional systematic error, as discussed in Section 3.6.

the pulsar and PWN, accompanied by an uncertain shell (J. A. Combi et al. 2006). The diffuse X-ray emission attributed to a nebula is ∼1.′5 in size. An unidentified extended TeV source HESS J1634–472 is in the vicinity and possibly associated (H. E. S. S. Collaboration et al. 2018; see Figure 19, right panel). A GeV extended source 4FGL J1636.3–4731e is also close by, but likely unrelated as the source coincides better to SNR G337.0–0.1, both in size and location (M. Ackermann et al. 2017). Adding an additional point source at the G337.20+0.10 position is detected at TS = 18.4 (see Figure 19, right panel). The best-fit photon index is $\Gamma = 2.26 \pm 0.12$. We note there is no 4FGL counterpart to this source in the 4FGL–DR4 catalog.

G337.50–0.10. The Chandra X-ray Survey unveiled a probable bow-shock PWN powered by central pulsar candidate CXOU J163802.6–471358 (S. J. Jakobsen et al. 2014). The X-ray nebula extends on the subarcminute scale (∼40″). The position and approximate size of the nebula is displayed in Figure 19 (right panel). There is a close candidate source in the 4FGL–DR3, 4FGL J1638.4–4715c, which we find is the likely GeV counterpart to this system and yields TS = 42.7 and power-law spectral index $\Gamma = 2.69 \pm 0.10$ when localized to the PWN, a significant improvement to the 4FGL–DR2 fit. We consider the γ-ray source 4FGL J1638.4–4715c a possible counterpart to G337.50–0.10, but it is a tentative detection due to it being a heavily crowded region in the Galactic plane that is among uncertain diffuse residual γ-ray emission.

4.3.3. Nondetections of PWNe

There are 19 PWNe and PWN candidates that have been identified at radio, X-ray, and TeV bands that are not significantly detected in the Fermi–LAT data. All of the undetected PWNe are listed in Table 6 along with their measured TS and the 95% C.L. flux upper limit for the 300 MeV–2TeV energy range. Another source is listed in Table 6: G25.10+0.02. The reported nondetection refers to the removal of a second extended PWN candidate (4FGL J1838.0–0704e) in the region associated with TeV PWN HESS J1837–069 (see also HESS J1837–069 in Section 4.3.1).

Identifying and characterizing PWNe inside γ-ray bright SNRs is challenging. The PWN G266.97–1.00 is powered by the pulsar PSR J0855–4644, and together, they lie on the SW edge of the Vela Jr. SNR (F. Acero et al. 2013a). The Vela Jr. SNR is a GeV emitter, 4FGL J0851.9–4620e, and is nearly 1° in radius. A TS signal is exclusively detected at $E < 1$ GeV in

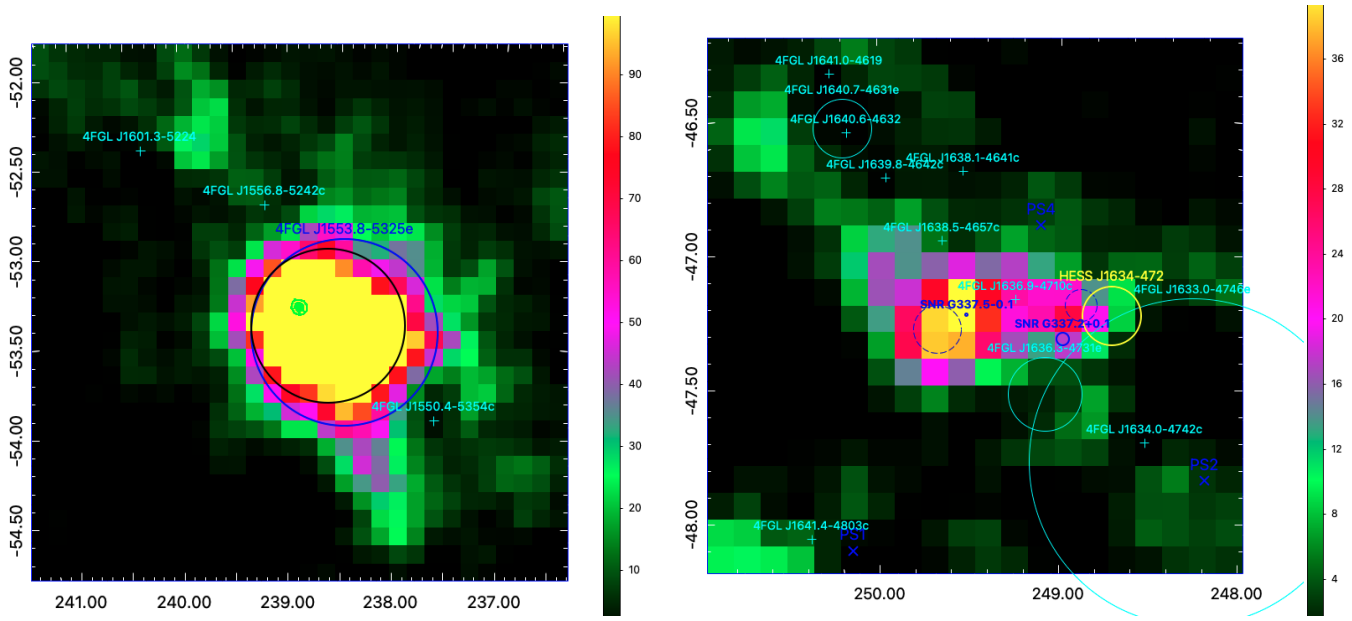

Figure 19. Left panel: a 2° × 2° 1–10 GeV TS map of PSF3 events for PWN G328.40+0.20. The Crab-like radio SNR is shown as the green contours. 4FGL J1553.8–5352e is shown in blue but is not included in the source model. The best-fit Gaussian source is marked in black. The maximum TS at the PWN/SNR position is ∼300. Right panel: a 2° × 2° 1–10 GeV TS map of PSF3 events for PWN candidates G337.20+0.10 and G337.50–0.10. The PWN positions and approximate sizes are indicated with solid blue circles. The best-fit positions with 95% positional uncertainty are shown as the dashed blue circles. Note that 4FGL J1636.3–4731e is the unrelated SNR G337.1–0.1. The unidentified TeV source HESS J1634–472 corresponds to the yellow circle. The maximum TS at the PWN position is TS ∼45 for 1–10 GeV. Unrelated 4FGL sources are labeled in cyan.

the nearby region of G266.97–1.00. This would not be unusual for Fermi–LAT pulsars, but may also be explained as structure associated with the Galactic diffuse emission that is not being accounted for properly by the background. The extended TeV counterpart RX J0852.0–4622 to the SNR was investigated for a PWN or pulsar contribution, but disentangling TeV emission components was not feasible (M. P. Arribas et al. 2012). A deeper analysis exploring both the GeV and TeV extended emission may provide better insight to any additional significant emission in the region (e.g., A. Donath et al. 2024).

A similar case is seen in the ROI for IC 443. There is a PWN candidate G189.10+3.00 observed in X-ray that overlaps with two SNRs including IC 443 and the unconfirmed SNR candidate G189.60+3.30 (D. A. Leahy 2004; S. Zhang et al. 2018). We place an additional point source at the PWN position, which yields TS = 26 and spectral index $\Gamma = 2.02 \pm 0.09$ for energies 300 MeV–2 TeV, but we do not attempt to analyze this region further due to the complexity. A dedicated study is required to reliably determine any potential PWN presence within IC 443 in the Fermi–LAT data.

Fermi–LAT data analysis is even more complicated within $\sim 1.^{\circ}0$ of the Galactic center, where at least four PWN candidates are located: SNR G00.00+0.00, PWN G0.13–0.11, PWN G359.90–0.04, and PWN G358.50–0.96. The last source may have a possible extended GeV counterpart 4FGL J1745.8–3028e (S. Marchesi et al. 2024). The ROIs are heavily crowded due to the proximity to the Galactic center, introducing convergence problems in the global fits as well as making source identification extremely difficult if not impossible. Hence, we do not analyze or discuss any of the PWN candidates located within $\sim 1.^{\circ}0$ from the Galactic center.

Aside from the uncertainties in the ROIs just described, the regions for undetected PWNe and PWN candidates are relatively sparse, making any source detection fairly straightforward. In all cases, a point source is added to the PWN position assuming a power-law spectrum. The TS results for each source are provided in Table 6. In Appendix C (Table C2), we provide the 95% C.L. upper limits on the flux for nine energy bins of each undetected PWN.

4.4. Summary of Results

In the 58 regions analyzed, we detect nine unidentified γ-ray sources that we classify as likely PWNe and present them in the top panel of Table 2 (six pointlike detections) and in the middle panel of Table 4 (three extended detections, excluding RCW 103). These sources likely have a PWN contribution, particularly at high energies ($E > 10$ GeV), but need follow-up multiwavelength studies in order to determine and characterize the γ-ray origin. The three likely extended γ-ray PWNe would bring the total number of extended Fermi–LAT PWNe with no detectable γ-ray pulsar from six to nine, and the entire extended Fermi–LAT PWN population from 12 to 15.[82] There are currently no identified pointlike Fermi–LAT PWNe in the 4FGL catalogs (J. Ballet et al. 2023).

We classify another 21 γ-ray sources as PWN candidates and list them in the bottom panels of Tables 2 and 4 based on whether they are observed as pointlike (15/21) or extended (six out of 21). The dominant γ-ray origin for the 21 weaker PWN candidates is less clear, either due to the lack of a TeV PWN counterpart and(or) being associated with a PWN/SNR system that is energetic in nature, where the pulsar, PWN, or SNR shell could plausibly explain the high-energy emission. The most interesting cases in both the likely and weak PWN candidate classes are described in more detail in Section 4.3. There are 19 PWNe where no significant residual emission is detected. They are listed in Table 6 and discussed in

[82] The Fermi–LAT PWN 3C 58 is extended in the 4FGL–DR4 catalog, based on the work of J. Li et al. (2018).

Table 7
Summary of Classification Criteria

Criterion	Likely PWN (Total = 9)	Candidate PWN (Total = 21)
TeV counterpart present	7	8
TeV source identified as PWN	6	2
MWL[a] study favors PWN origin	9	∼3
Confirmed MWL PWN counterpart	9	8
Location in LAT sky	Generally not complex	Some in complex or uncertain regions
…		

Notes. The numbers indicate how many sources meet each criterion within the classification group. Because a single source can satisfy multiple criteria, the values do not sum to the total number of sources.
[a] Multiwavelength (MWL).

Section 4.3.3. In total, there are 36 detected γ-ray sources of which three coincide with two lower-energy PWN counterparts each (see Table 4).

We point out three important distinctions that separate the likely from the weak candidate class. The first distinction is that the majority of likely PWNe are coincident with TeV counterparts that are classified as PWNe based on multiwavelength investigations of the lower-energy counterparts known to be PWNe (six out of nine; see Table 5). The second applies to the Fermi–LAT sources (two out of nine) that do not have identified TeV counterparts (G8.40+0.15 and B0453–685), but that have prior detailed multiwavelength analyses where a PWN origin of the Fermi–LAT γ-ray emission is preferred. The third is for the final likely PWN, G315.78–0.23, an energetic bow-shock PWN fully displaced from its SNR shell and powered by the pulsar now traveling supersonically in the ISM beyond the SNR. These distinctions are summarized in Table 7. An identified multiwavelength counterpart with a detailed broadband study is the primary qualifier for a likely PWN. As a final note, in general, a confident PWN classification requires either a morphological study showing compelling correspondence (e.g., J. Li et al. 2018) or correlated variability, verified only by the flaring Crab Nebula.

5. Discussion

We have systematically characterized the 300 MeV–2 TeV emission from 11.5 yr of Fermi–LAT data in 58 ROIs containing known PWNe and PWN candidates identified at other wavelengths, and the source sample analyzed includes six previously identified Fermi–LAT PWNe and eight PWN associations.

Approximately ∼40% of the source detections reported here are found to be extended. Two sources are reported as extended that are not considered extended in previous Fermi–LAT catalogs: 4FGL J1818.6–1533 and 4FGL J1844.4–0306. One new γ-ray source considered a likely PWN is reported here that was not reported in any previous Fermi–LAT catalogs, corresponding to the PWN in the LMC, B0453–685 (Figure 7, right panel). If a PWN origin can be identified, B0453–685 would represent the second extragalactic γ-ray PWN to be detected at such high energies after N 157B, noting that the PWN origin of N 157B still needs to be confidently known as well. Only one candidate γ-ray source is first reported here that has no prior Fermi–LAT counterpart: G337.20+0.10.

In Figure 20 (left panel), the 300 MeV–2 TeV GeV luminosity is shown as a function of the associated pulsar's spin-down power $\dot{E}$ (if known). The properties of firm pulsar associations are listed in Appendix B, Table B1. The GeV luminosity accounts for the uncertainty on the 300 MeV–2 TeV flux in addition to assuming 20% uncertainty on the pulsar distance, following F. Acero et al. (2013b), which we collect from the Australia Telescope National Facility (ATNF) pulsar catalog,[83] adopting the distances measured from dispersion measure. As reported in F. Acero et al. (2013b), there is no clear correlation between the GeV luminosity and the pulsar spin-down power. In the right panel of Figure 20, we plot the GeV luminosity as a function of pulsar characteristic age, which we also gather from the ATNF pulsar catalog. No clear correlation is found between the two properties, similar to F. Acero et al. (2013b).

Finally, we measure the ratio between both the 300 MeV–2 TeV and 1–10 TeV γ-ray luminosity to the 2–10 keV X-ray luminosity for those in Tables 5 and 6 that have an X-ray and TeV counterpart and plot the ratio as a function of the pulsar spin-down power $\dot{E}$ to compare to the derived relation in F. Mattana et al. (2009). We find a similar trend as F. Mattana et al. (2009) with one outlier from the nondetected group, G358.3+0.24, which is explained by the low $\dot{E}$ of the associated pulsar, $\dot{E} \sim 10^{34}$ erg s^{-1}.

5.1. PWN Origin through Radiative Modeling

For some of the best candidates and a few more as examples of young PWNe, listed in Table 8, we investigate their possible multiband spectra in the context of a PWN evolutionary model, as outlined in D. F. Torres et al. (2014) and J. Martin & D. F. Torres (2022). The aim is not to fit the GeV data (for there is too scarce a number of data points) but rather to explore whether our data are consistent with model predictions using conservative ranges of free parameters. The predicted SEDs are obtained using the observational data detailed in Table 8 and a range of reasonable values for nine unknown parameters (W. Zhang et al. 2024). Assumed ranges to span possible theoretical PWNe spectra include the SN ejecta mass M_{ej} between 8 and 15 $M_\odot$, particle index before the break $\alpha_1 = [1.0,1.6]$, break $\gamma_b = [10^5,10^6]$, far-IR/near-IR energy density $U_{\rm FIR}$ = 1–3 times the GALPROP value, true age between [0.7–1.3] τ_c (except for G11.2–0.35 with a true age of about 1.6 kyr; D. H. Clark et al. 1977), braking index n = 2, 2.5, 3 (except for G29.70–0.30, which has measured values before/after the burst where we adopt the post-burst index = 2.16; M. A. Livingstone et al. 2011), magnetic energy fraction η_B = 0.02–0.04, particle index after the break energy α_2 = [2.2, 2.8], and ISM particle density $n_{\rm ISM} = [0.1, 1.0]\,{\rm cm}^{-3}$. The employed parameter ranges are motivated by the observed properties of several PWNe as well as predicted values of the properties from simulations (see J. Martin & D. F. Torres 2022, and references therein).

We have generated 712 possible models for each source by combining the minimum and maximum values of these nine parameters to create $2^9 = 512$ specific SEDs ($2^8 = 256$ for G11.2-0.35), and then adding 200 models by randomly selecting values within these intervals. These models span possible SEDs for these γ-ray sources under the assumption that they are similar to other PWNe already detected by the

[83] https://www.atnf.csiro.au/research/pulsar/psrcat/

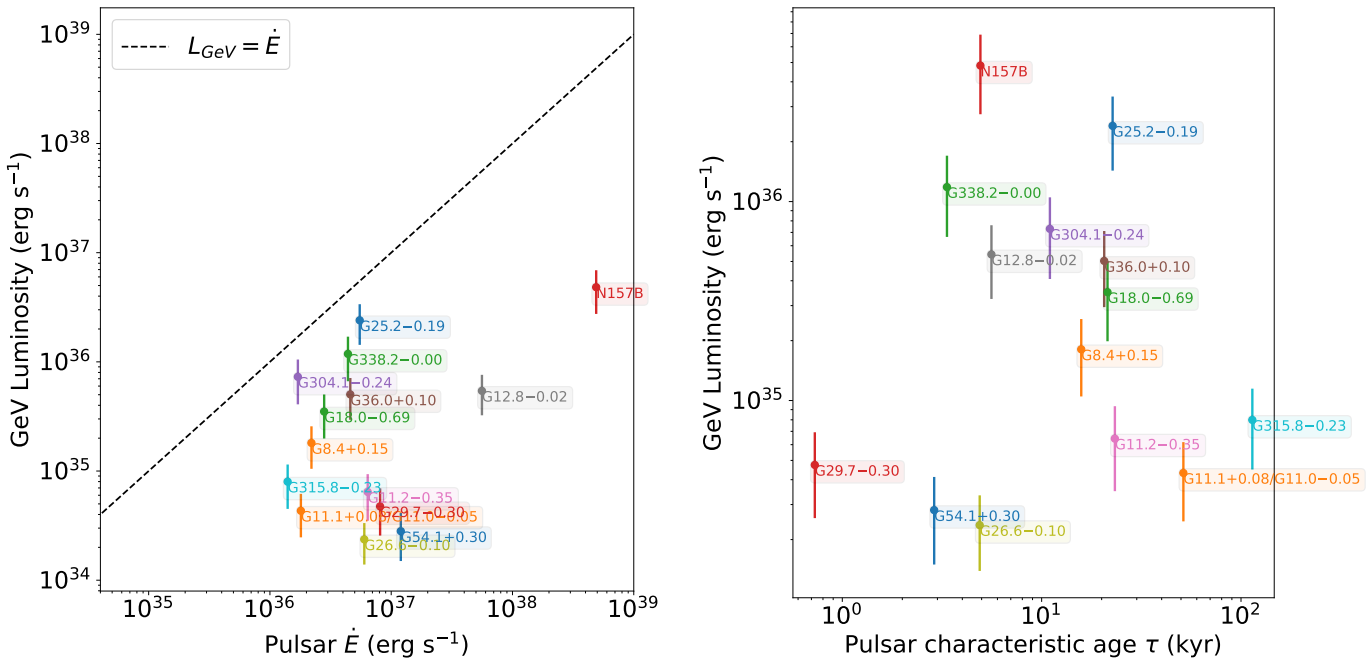

Figure 20. Left panel: 300 MeV–2 TeV luminosity of the PWNe as a function of pulsar spin-down power. Right panel: 300 MeV–2 TeV GeV luminosity as a function of pulsar characteristic age.

Table 8
Five ROIs Explored Using the Evolutionary Model in J. Martin & D. F. Torres (2022) and Their Observational Constraints

PWN Name	Type of Candidate Likely (L) or Weak (W)	$\dot{E}$ (erg s^{-1})	τ_c (kyr)	d (kpc)	PWN Size (°)	References
G11.18–0.35	W	6.4×10^{36}	29.88	3.7	0.011	K. K. Madsen et al. (2020)
	…	…	…	…	…	S. Ranasinghe & D. Leahy (2022)
G12.82–0.02	W	5.6×10^{37}	5.6	6.2	0.05	Y. C. Joshi et al. (2023)
	…	…	…	…	…	H. E. S. S. Collaboration et al. (2018)
G15.40+0.10	W	7.0×10^{36}	17	9.3	0.14	H. E. S. S. Collaboration et al. (2014)
	…	…	…	…	…	H.-Q. Su et al. (2017)
G29.70–0.30	L	8.1×10^{36}	0.723	5.8	0.0083	S. M. Straal et al. (2023)
G327.15–1.04	L	3.1×10^{36}	17.4	9	0.02	T. Temim et al. (2015)
	…	…	…	…	…	H. E. S. S. Collaboration et al. (2018)

Note. The second column identifies the type of PWN classification: (L) for likely or (W) for weak. See Section 5.1 for details. The third through fifth columns show the pulsar spin-down power, distance, age, and PWN radius. The final column lists the references for those values. For G327.15–1.04 and G15.40+0.10, the pulsar is not known, and therefore, the pulsar spin-down power, age, and distance are fixed to estimates adopted from the listed references. The spin-down power of G15.40 +0.10 is assumed as an appropriate value.

Fermi–LAT like the Crab or 3C 58. The panels of Figure 21 show that PWN models are in general in agreement with the observed fluxes, but the spectral slope is not reproduced for most of the models. This suggests that either these PWNe behave differently from the rest or the γ-ray data suffer from contamination from other members of the complex (pulsar or remnant).

5.2. Caveats

This Fermi–LAT study is limited by the complexity of the γ-ray data including the systematic uncertainties from the diffuse Galactic background and the uncertainties from the effective area. We emphasize here that while we attempt to account for these effects, the uncertainties explored here may not fully represent the range of systematics involved (see, e.g., F. Acero et al. 2016). The systematic study explored in Section 3.6 adopts the method from F. de Palma et al. (2013) and F. Acero et al. (2016). It is found that typically the systematic uncertainties on the flux dominate over the statistical uncertainties for sources that lie along the Galactic plane ($|b| < 1.^{\circ}0$) and for energies below 5 GeV. The systematic impact on source extension is on the same order as the statistical error. These findings are in agreement to prior studies (F. Acero et al. 2016; M. Ackermann et al. 2017). In general, uncertainties from the IEM model remain the most important, while consideration of the location to nearby bright sources especially those of Fermi–LAT pulsars can also be critical. Though an incomplete systematic study as mentioned above, this work is among the most detailed investigations on the systematic uncertainties for fluxes and extensions of Fermi–LAT detected PWNe.

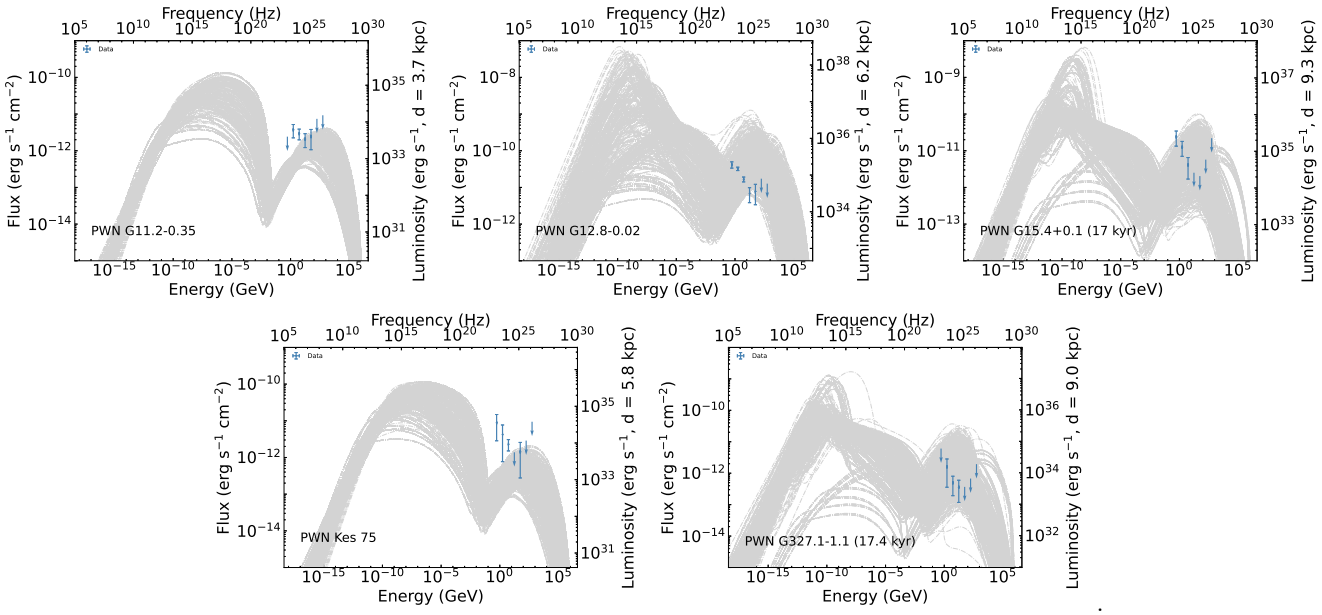

Figure 21. Shown here are 712 (456 for G11.2–0.3) predicted SEDs from an evolutionary model (J. Martin & D. F. Torres 2022) for several of the sources studied as examples. See Table 8 for relevant parameters (see also W. Zhang et al. 2024).

6. Conclusion

In summary, we have verified the characterization and classification of the six Fermi–LAT PWNe that lack any detectable γ-ray pulsar, and show that all of them, with the exception of MSH 15–56, can be characterized using radial Gaussian templates that either provide comparable fits to a radial disk template or better. We note that two likely extended Fermi–LAT PWNe, 4FGL J0836.5–0651e and 4FGL J1616.2–5054e, have more than one possible PWN counterpart identified in other wavelengths (see Section 4.3.1). Further, we analyze eight possible PWN associations from the Fermi–LAT catalogs and find that most of them (five out of eight) are likely γ-ray PWNe based on their multiwavelength properties; they are discussed in detail in Section 4.3.1. We argue that one of the associations, 4FGL J1838.9–0704e, a second extended source possibly modeling emission from the PWN HESS J1837–069, is not required. 4FGL J1836.5–0651e, when modeled as a radial Gaussian extended source, can adequately model any extended residual γ-ray emission coincident with HESS J1837–069.

4FGL J1810.3–1925e overlaps two radio PWN candidates that are plausible counterparts (Section 4.3.2 and Figure 11). In many of these less-clear cases, such as G11.03–0.05, G11.09+0.08, and G18.90–1.10, the source classification depends on the lower-energy counterparts being confirmed as PWNe rather than candidates. For the youngest systems such as G11.18–0.35 and G20.20–0.20, an additional challenge is ruling out contribution from the central pulsar and/or host SNR shell.

The nine previously unidentified γ-ray sources that are likely PWNe, if confirmed, would increase the PWN population detected by the Fermi–LAT from 12 (J. Ballet et al. 2023) to 21. An additional 21 previously unidentified γ-ray sources are considered PWN candidates. The total number of detected γ-ray sources is 36 with three extended sources that overlap with more than one lower-energy PWN counterpart, as mentioned just above. Among the 58 PWNe and PWN candidates analyzed here, 19 remain undetected. Additionally, 36/58 or 62% of the sample selection is associated with a γ-ray source. We have demonstrated that the Fermi–LAT data set probably contains a larger PWN population present than is currently known. Nevertheless, many of the source classifications are uncertain and hence require a justification from a thorough broadband analysis. A cursory study characterizing the radiative properties of a selection of PWN candidates (Section 5.1) highlights the need to include broadband information. This work represents a list of ideal targets for future X-ray and TeV observations. A subsequent search will analyze the off-pulse data of Fermi–LAT detected pulsars for the presence of a PWN and will be reported in the future.

Acknowledgments

The Fermi–LAT Collaboration acknowledges generous ongoing support from a number of agencies and institutes that have supported both the development and the operation of the LAT as well as scientific data analysis. These include the National Aeronautics and Space Administration and the Department of Energy in the United States, the Commissariat à l'Energie Atomique and the Centre National de la Recherche Scientifique / Institut National de Physique Nucléaire et de Physique des Particules in France, the Agenzia Spaziale Italiana and the Istituto Nazionale di Fisica Nucleare in Italy, the Ministry of Education, Culture, Sports, Science and Technology (MEXT), High Energy Accelerator Research Organization (KEK) and Japan Aerospace Exploration Agency (JAXA) in Japan, and the K. A. Wallenberg Foundation, the Swedish Research Council and the Swedish National Space Board in Sweden.Additional support for science analysis during the operations phase is gratefully acknowledged from the Istituto Nazionale di Astrofisica in Italy and the Centre National d'Études Spatiales in France. This work performed in part under DOE contract DE- AC02-76SF00515.This work has also been partially supported by the grant PID2021-124581OB-I00 funded by MCIN/AEI/10.13039/501100011033, 2021SGR00426, by the Spanish program Unidad de Excelencia María de Maeztu CEX2020-001058-M, and European Union NextGeneration EU funds (PRTR-C17.I1).

Software: FermiPy (v.1.0.1, M. Wood et al. 2017), Fermitools: Fermi Science Tools (v2.0.8, Fermi Science Support Development Team 2019).

Appendix A
System Checks

We reanalyze five sample ROIs considering more Fermi–LAT data and the latest comprehensive 4FGL–DR4 catalog as a system check for the results in this report. Three of the sample PWNe are considered weak candidate source detections (G11.18–0.35, G12.82–0.02, and G15.40+0.10), and two are considered likely PWN source detections (G29.70–0.30 and G327.15–1.04). We summarize the configuration details of the reanalysis results using 14 yr of Fermi–LAT data compared to the analysis using 11.5 yr in Table A1. In all five cases, the analysis and reanalysis results are consistent. We compare the SEDs reported in the main paper and those found with the updated data configuration and integration time in Figure A1.

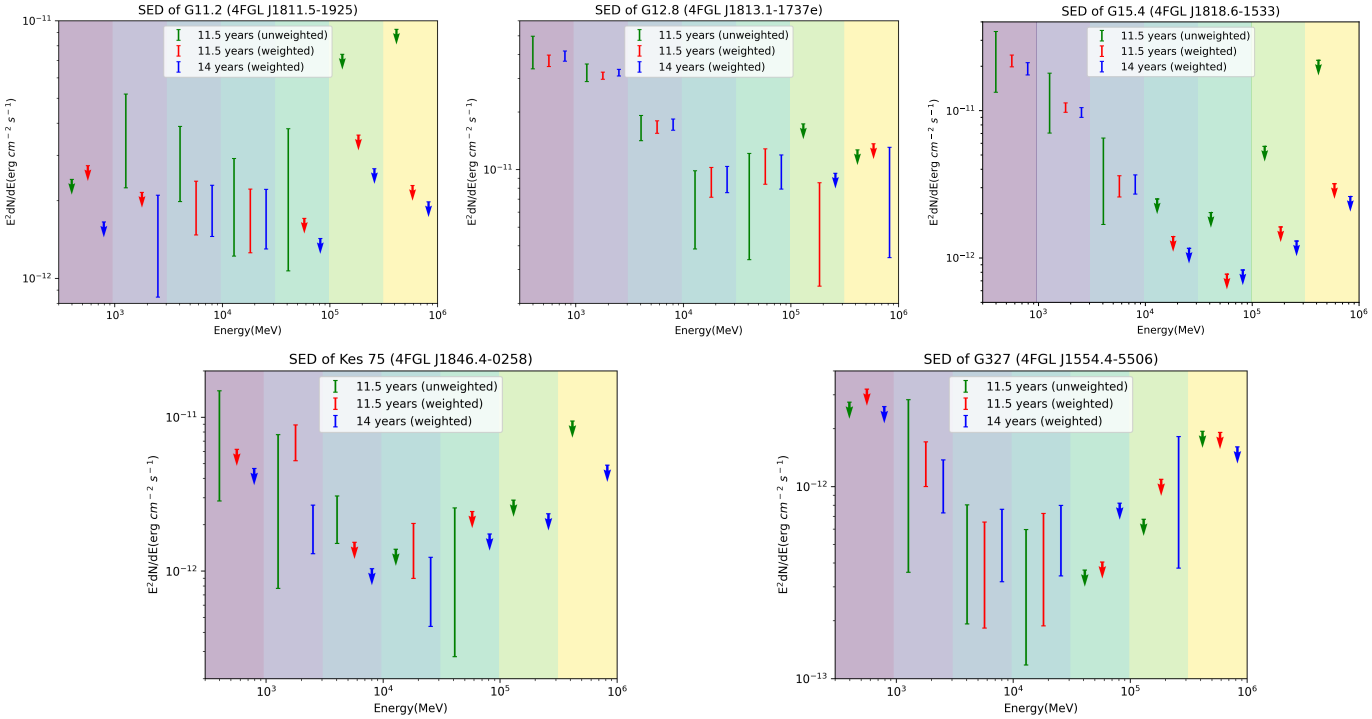

Figure A1. Comparison of SEDs under different data configurations for five sources (Table A1). The 11.5 yr (unweighted) data points correspond to the main results of this work and include both statistical and systematic errors.

Table A1
Data Configuration Details for the 11.5 yr Data Analysis of this Report Compared to a 14 yr Reanalysis Using an Updated Source Model

Fermi–LAT Data Configuration	14 yr (Weighted)	11.5 yr (Weighted)	11.5 yr (Unweighted)
Time range	2008 Aug 4–2023 Aug 15	2008 Aug 4–2020 Jan 1	2008 Aug 4–2020 Jan 1
Energy range	300 MeV–1 TeV	300 MeV–1 TeV	300 MeV–2 TeV
Catalog	4FGL–DR4	4FGL–DR2	4FGL–DR2
Event type	8/16/32 (0.3–1 GeV) 4/8/16/32 (1–1000 GeV)	8/16/32 (0.3–1 GeV) 4/8/16/32 (1–1000 GeV)	32
Zmax	[c]100° (0.3–1 GeV) 105° (1–1000 GeV)	100° (0.3–1 GeV) 105° (1–1000 GeV)	100°
Extended source template	Extended_14years	Extended_8years	Extended_8years
Weighted (Y/N)	Y	Y	N
Fermitools	2.2.0	2.2.0	2.0.8

Appendix B
Population Studies: High-energy Characteristics

For extended sources, the best-fit radius r when assuming a 2D radial disk template can be up to 1.85 times larger than σ when assuming a 2D radial Gaussian such that the r_{68} of either template is approximately the same (J. Lande et al. 2012). The plots in Figure B1, both panels, explore this behavior. In the left panel of Figure B1, we plot the best-fit r_d as a function of the best-fit $r_g = 1.51\sigma$, both measured in this work. On the whole, the extension sizes agree with one another, lying either on the 1:1 solid black line or just below it where r_d is somewhat smaller than r_g. The exception is clearly HESS J1825–137 (G18.00–0.69 in red), where we measure $r_g = 0.^{\circ}83$, compared to the radial disk fit that finds $r_d \sim 0.^{\circ}60$ (r_d is ∼1.4 times smaller than r_g). In the right panel of Figure B1, we plot the best-fit r that characterizes the extended sources in the 4FGL catalogs (J. Ballet et al. 2023) as a function of the best-fit r_g reported in this work. Sources that are fit as a disk in 4FGL–DR4 are plotted in yellow, and those fit as a Gaussian in 4FGL–DR4 are plotted in blue. Those that are fit using a disk template in DR4 (yellow) tend to have larger extensions in DR4 than found here but are still reasonably consistent with the effect explored in the left panel. One source, G304.10–0.24, is fit as a radial Gaussian in both works, though we find a slightly larger extension ($0.^{\circ}35$) than in DR4 ($0.^{\circ}24$). In Figure B2 (left panel), the TeV extension is plotted as a function of the GeV extension found here. Either consistent TeV and GeV extensions or slightly smaller TeV extensions are observed. This is in agreement with what is found in F. Acero et al. (2013b). From an energetics standpoint, this is not surprising, considering evolved PWNe may have large differences in TeV and GeV extensions due to the rapid cooling of the highest-energy particles.

We investigate the spectral trends expected of γ-ray PWNe, shown in Figure B2 (right panel), plotting the TeV spectral index as a function of GeV index. For the systems whose associated pulsars are known, we include this information in the plot. There is a broad spread, but the majority (14/19) of sources fall above the 1:1 slope plotted in black, suggesting that most have a softer (larger) TeV spectral index than GeV spectral index, which is consistent with the predicted high-energy emission characteristics from F. Acero et al. (2013b), but may have important contributions from other physical properties of the systems such as the characteristic pulsar age and(or) the distance.

We explore the ways the distance may influence the high-energy spectral properties in both panels of Figure B3. Within uncertainty, there are no strong correlations present. However, the modest positive correlation, measured by the Pearson correlation coefficient, c_P, that is derived for the GeV luminosity with pulsar distance ($c_P = 0.9 \pm 0.5$) may be indicating a selection effect, where we are biased toward detecting only the closest PWNe. The TeV luminosity with pulsar distance ($c_P = 1.0 \pm 0.5$) and the TeV spectral index as a function of pulsar distance ($c_P = 0.5 \pm 0.2$) have similar implications. In Figure B4 (left panel), the GeV index as a function of pulsar characteristic age is shown. There is a positive correlation $c_P = 0.5 \pm 0.05$, implying softer γ-ray spectra for older systems. This is an unexpected result since PWNe are expected to become γ-ray bright with age (e.g., J. D. Gelfand et al. 2009; P. Slane 2017). It is worth noting that the correlation becomes negative ($c_P = -0.4 \pm 0.05$) if G315.8–0.23 is not considered. In any case, the result may be convoluted by possible pulsar contributions; see also the right panel of Figure B4, where the hardest spectra are observed from extended sources, and the softest sources are all pointlike.

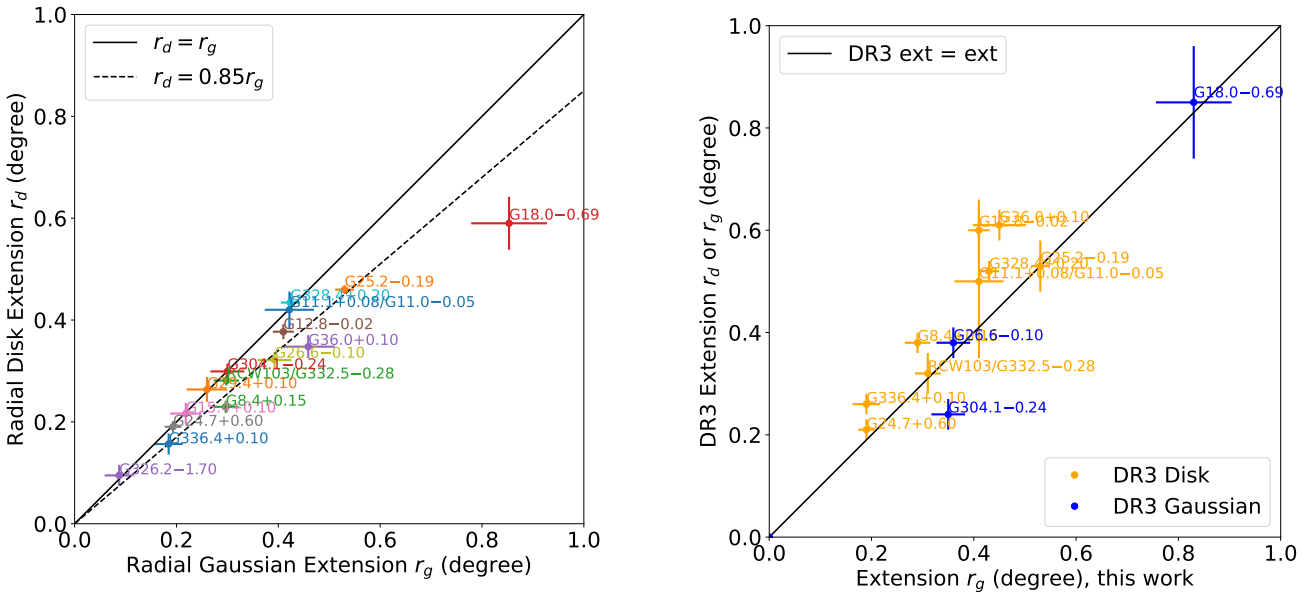

Figure B1. Left panel: best-fit radii to best-fit Gaussian extensions (68% containment) from this work. Right panel: best-fit Gaussian extensions from this work to the best-fit radius (yellow) or Gaussian radius (blue) in DR3.

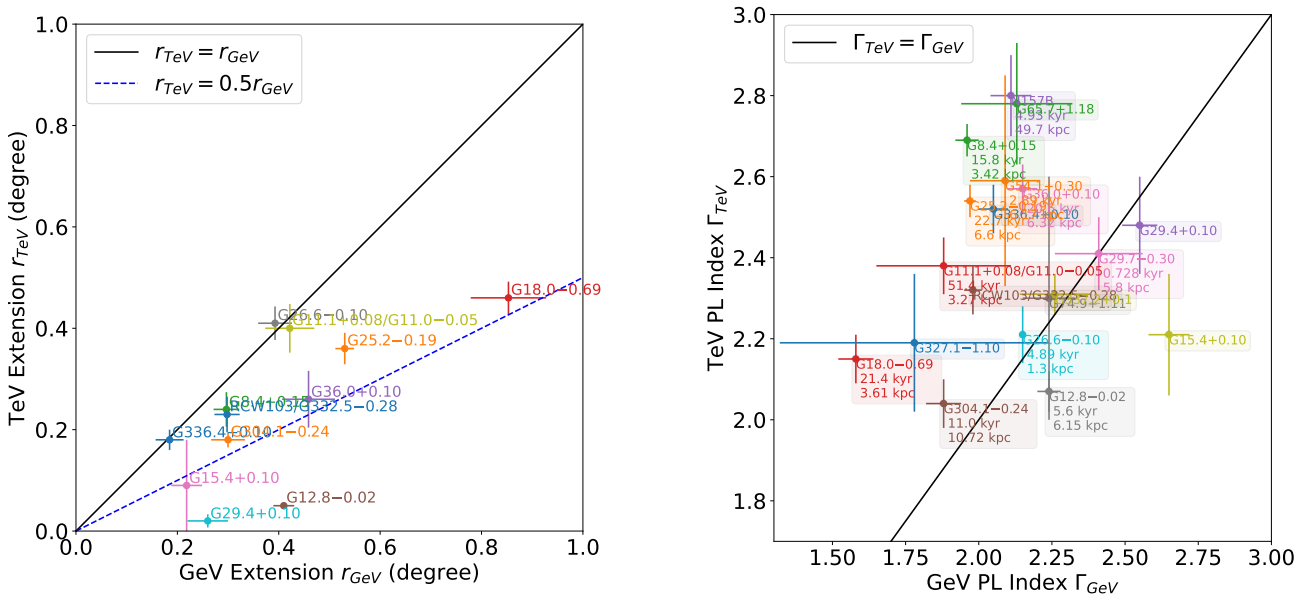

Figure B2. Left panel: best-fit TeV extensions to the best-fit GeV extensions (68% containment) found in this work. Right panel: TeV index as a function of the GeV index.

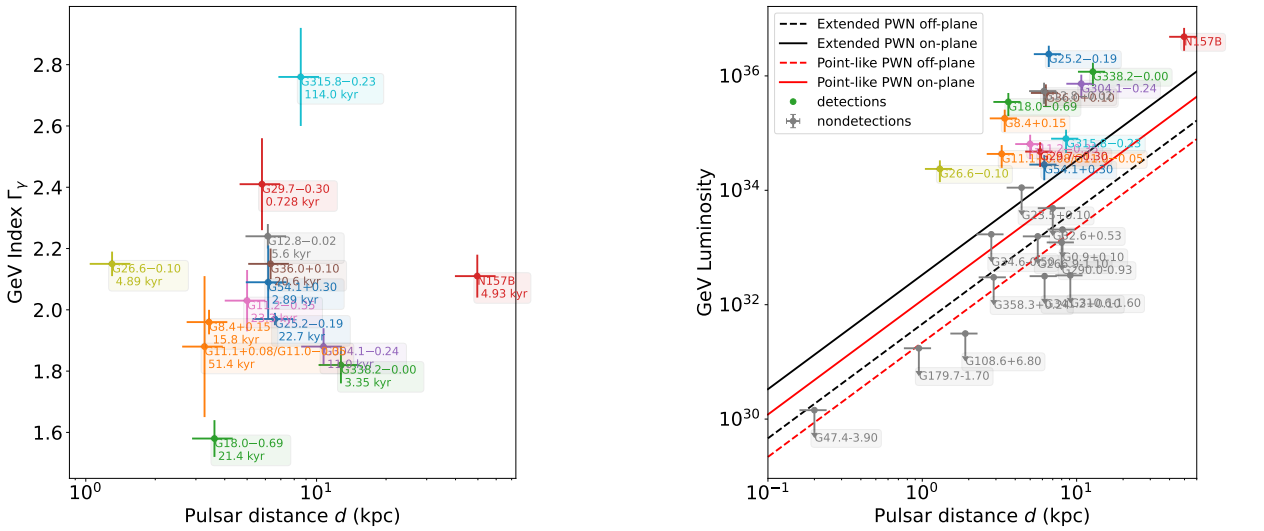

Figure B3. Left panel: GeV index as a function of pulsar distance. Right panel: 300 MeV–2 TeV luminosity as a function of pulsar distance. The sensitivity of the Fermi–LAT instrument varies based on the source sky location and source shape. We plot the sensitivity limits for four cases: pointlike (extended) source located on (off) the Galactic plane. In all cases, a power-law spectrum with $\Gamma = 2$ is assumed. The extended source shape assumes the average size of the sample $\sim 0.^{\circ}4$. For comparison, we plot the nondetected sources that have associated pulsars in gray.

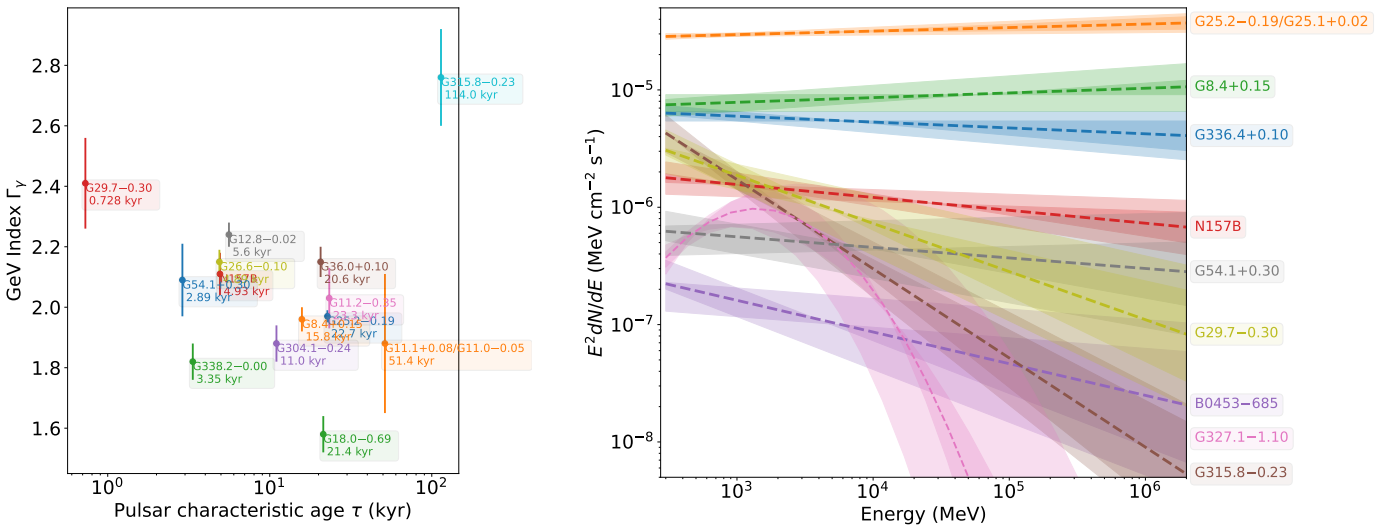

Figure B4. Left panel: GeV index as a function of pulsar characteristic age. Right panel: best-fit spectral models for the nine likely PWNe.

Table B1

Associated Pulsar Name and Relevant Properties for the Detected Sources (Top) that Have Confirmed Pulsar Associations and for Nondetected Sources (Bottom)

ROI	Galactic PWN Name	4FGL ID	Associated Pulsar	d (kpc)	τ_c (kyr)	$\dot{E}$ (10^{36} erg s^{-1})
1	G8.40+0.15	J1804.7–2144e	J1803–2137	3.42	15.8	2.2
2	G11.09+0.08	J1810.3–1925e	J1809–1917	3.27	51.4	1.8
3	G11.18–0.35	J1811.5–1925	J1811–1925	5	23.3	6.4
4	G12.82–0.02	J1813.1–1737e	J1813–1749	6.15	5.6	56
5	G18.00–0.69	J1824.5–1351e	J1826-1334	3.61	21.4	2.8
6	G25.24–0.19	J1836.5–0651e	J1838-0655	6.6	22.7	5.5
7	G26.60–0.10	J1840.9–0532e	J1838-0537	1.3	4.89	6.0
8	G29.70–0.30	J1846.4–0258 (DR4)	J1846–0258	5.8	0.728	8.10
9	G36.01+0.10	J1857.7+0246e	J1856+0245	6.32	20.6	6.4
10	G54.10+0.27	J1930.5+1853 (DR3)	J1930+1852	6.17	2.89	12
11	G279.60–31.70 (N 157B)	J0537.8–6909	J0537–6910	49.7	4.93	490
12	G304.10–0.24	J1303.0–6312e	J1301–6305	10.7	11	1.7
13	G315.78–0.23	J1435.8–6018	J1437–5959	8.54	114	1.4
14	G332.50–0.28	J1616.2–5054e	J1617–5055	4.74	8.13	16
15	G338.20–0.00	J1640.6–4632 (DR1), J1640.7–4631e (DR3)	J1640–4631	12.7	3.35	4.4
1	G0.87+0.08	⋯	J1747–2809	8.1	5.3	43.0
2	G23.50+0.10	⋯	J1833-0827	4.4	147	0.58
3	G32.64+0.53	⋯	J1849–0001	7	43.1	9.8
4	G34.56–0.50	⋯	J1856+0113	2.81	20.3	0.43
5	G47.38–3.88	⋯	J1932+1059	0.2	3100	0.004
6	G108.60+6.80	⋯	J2225+6535	1.9	1120	0.001
7	G179.72–1.69	⋯	J0538+2817	0.95	618	0.05
8	G266.97–1.00	⋯	J0855–4644	5.6	141	1.1
9	G290.00–0.93	⋯	J1101–6101	8[a]	116	1.4
10	G310.60–1.60	⋯	J1400–6325	9.1	12.7	51
11	G341.20+0.90	⋯	J1646-4346	6.2	32.5	0.36
12	G358.29+0.24	⋯	J1740–3015	2.9	20.6	0.008

Notes. The pulsar properties are from the ATNF pulsar catalog (R. N. Manchester et al. 2005).
[a] The distance estimate listed for PSR J1101–6101 comes instead from J. P. Halpern et al. (2014).

Appendix C
Spectral Flux Measurements

We provide the spectral flux value $E^2\frac{dN}{dE}$[84] per bin for seven logarithmically spaced energy bins for all 36 detected sources (Tables 2 and 4) in Table C1. We additionally provide the 95% upper limit to the spectral flux $E^2\frac{dN}{dE}$ per bin for nine logarithmically spaced energy bins for the 19 PWNe with no source detection (Table 6) in Table C2, measured by placing a point source at each PWN position assuming a power-law spectrum. All flux values are in units MeV cm^{-2} s^{-1}.

Finally, we provide the 300 MeV–1 TeV SEDs for the nine detected γ-ray sources classified as likely PWNe in Figures C1–C9. The complete figure set of all 36 SEDs is provided. The best-fit fluxes with the 1σ statistical (orange) and total systematic (black) uncertainties are plotted. The lowest-energy flux error in blue represents the factor of $\sim$3 for the statistical error (see Table C1). The dashed white line and the blue uncertainty band (1σ) represent the best-fit spectral model (Table 5).

[84] Defined as the center energy $\sqrt{E_1E_2}$ squared multiplied by the differential flux at the center energy.

Table C1

Spectral Flux $E^2\frac{dN}{dE}$ per Bin for Seven Logarithmically Spaced Energy Bins for All 36 Detected Sources (Tables 2 and 4)

PWN Name	E = 535 MeV	E = 1, 705 MeV	E = 5, 432 MeV	E = 17, 303 MeV	E = 55, 116 MeV	E = 175, 560 MeV	E = 559, 204 MeV
G8.40+0.15	8.87 ± 1.04 ± 3.12 ± 7.02	7.25 ± 1.02 ± 5.66	8.04 ± 1.27 ± 3.91	8.95 ± 1.7 ± 1.77	11.7 ± 2.75 ± 1.37	7.04 ± 3.82 ± 1.24	13.3 ± 8.33 ± 1.07
G11.03−0.05[a]	7.84 ± 1.05 ± 3.14	7.48 ± 1.06	2.59 ± 1.23	1.55 ± 1.52	3.48	4.63	15.3
G11.09+0.08	…	…	…	…	…	…	…
G11.18−0.35	2.60	2.32 ± 0.555 ± 0.732	1.83 ± 0.477 ± 0.352	1.29 ± 0.517 ± 0.114	1.52 ± 0.853 ± 0.0485	4.62	5.78
G12.82−0.02	26.0 ± 1.15 ± 3.44 ± 4.92	20.1 ± 1.22 ± 1.75	10.4 ± 1.45 ± 0.612	4.27 ± 1.83 ± 0.404	4.84 ± 2.57 ± 0.936	10.8	7.91
G15.40+0.10	14.9 ± 0.908 ± 2.72 ± 6.52	7.8 ± 0.754 ± 3.32	2.56 ± 0.725 ± 1.32	1.57	1.27	3.57	13.7
G16.73+0.08	7.37 ± 0.851 ± 2.55 ± 4.26	3.47 ± 0.592 ± 1.67	1.67 ± 0.487 ± 0.297	1.19	0.836	1.83	5.86
G18.00−0.69	6.19 ± 1.38 ± 4.15 ± 2.21	6.2 ± 1.5 ± 5.41	8.36 ± 1.93 ± 2.79	15.4 ± 2.78 ± 0.888	20.1 ± 4.4 ± 3.57	31.6 ± 8.18 ± 5.46	14.7
G18.90−1.10	2.81 ± 0.713 ± 2.14 ± 0.813	3.8 ± 0.508 ± 0.244	1.39 ± 0.414 ± 0.14	0.517	1.17	1.79	5.84
G20.20−0.20	7.19 ± 0.866 ± 2.6 ± 1.22	5.6 ± 0.647 ± 1.13	1.09 ± 0.443 ± 0.262	1.09	0.627	3.05	5.84
G24.70+0.60	6.19 ± 0.878 ± 2.63 ± 1.87	7.09 ± 0.738 ± 1.18	7.98 ± 0.876 ± 0.453	4.57 ± 1.1 ± 0.285	4.01 ± 1.71 ± 0.439	7.21 ± 3.66 ± 0.58	19.3
G25.24−0.19	28.7 ± 1.29 ± 3.88 ± 1.89	30.0 ± 1.45 ± 1.16	26.7 ± 1.97 ± 0.944	31.9 ± 2.95 ± 1.18	34.2 ± 4.77 ± 2.68	41.8 ± 8.72 ± 3.06	28.9 ± 13.2 ± 2.24
G25.10+0.02	…	…	…	…	…	…	…
G26.60−0.10	13.9 ± 1.1 ± 3.29 ± 1.81	12.1 ± 1.08 ± 0.646	8.38 ± 1.26 ± 0.352	4.98 ± 1.64 ± 0.264	11.7 ± 2.99 ± 1.65	12.6 ± 5.25 ± 2.45	6.45
G27.80+0.60	3.52 ± 0.727 ± 2.18 ± 1.57	3.38 ± 0.502 ± 0.726	2.51 ± 0.465 ± 0.166	0.582 ± 0.397 ± 0.0342	0.547	1.85	5.87
G29.40+0.10	14.0 ± 1.03 ± 3.08 ± 7.24	8.4 ± 0.894 ± 4.45	2.98 ± 0.938 ± 1.84	1.35 ± 1.17 ± 0.694	2.2 ± 1.82 ± 0.741	4.93	5.88
G29.70−0.30	5.52 ± 0.898 ± 2.7 ± 3.63	2.64 ± 0.616 ± 2.07	1.43 ± 0.488 ± 0.0184	0.864	0.889 ± 0.714 ± 0.0572	1.8	5.88
G36.01+0.10	12.0 ± 1.1 ± 3.31 ± 2.53	9.97 ± 1.09 ± 0.763	7.06 ± 1.28 ± 1.21	7.61 ± 1.8 ± 0.915	8.19 ± 2.56 ± 0.704	6.51 ± 3.96 ± 1.55	21.3
G39.22−0.32	6.09 ± 0.827 ± 2.48 ± 3.55	3.04 ± 0.578 ± 1.51	2.23 ± 0.492 ± 0.3	0.659 ± 0.437 ± 0.057	1.18	1.86	5.83
G49.2−0.30	15.8 ± 0.884 ± 2.65 ± 3.63	11.4 ± 0.821 ± 2.45	3.47 ± 0.754 ± 0.747	1.42 ± 0.728 ± 0.27	1.48	5.48	5.66
G49.2−0.70	5.37 ± 0.84 ± 2.52 ± 0.704	3.75 ± 0.754 ± 0.981	3.13 ± 0.768 ± 0.311	1.34 ± 0.708 ± 0.127	1.33 ± 0.923 ± 0.122	1.75	5.66
G54.10+0.27	1.51	0.65 ± 0.232 ± 0.226	0.393 ± 0.165 ± 0.139	0.608 ± 0.201 ± 0.0836	0.664	0.824 ± 0.645 ± 0.0903	1.65
G63.70+1.10	1.2 ± 0.361 ± 1.08 ± 0.822	1.62 ± 0.276 ± 0.358	0.932 ± 0.255 ± 0.0842	0.289 ± 0.237 ± 0.0245	0.49	1.64	5.34
G65.73+1.18	2.51 ± 0.408 ± 1.22 ± 0.427	2.01 ± 0.307 ± 0.195	0.612 ± 0.243 ± 0.0548	0.724	0.495	2.11 ± 1.69 ± 0.0782	5.33
G74.94+1.11	3.3 ± 0.562 ± 1.69 ± 1.31	2.15 ± 0.449 ± 0.511	1.82 ± 0.43 ± 0.296	1.26 ± 0.461 ± 0.142	1.16	3.45 ± 2.01 ± 0.153	5.17
G279.60−31.70	1.49 ± 0.23 ± 0.691 ± 0.111	1.76 ± 0.224 ± 0.154	1.26 ± 0.253 ± 0.141	0.636 ± 0.298 ± 0.0769	0.861 ± 0.599 ± 0.143	1.92 ± 1.51 ± 0.245	12.9
G279.80−35.80	0.366	0.17 ± 0.0568 ± 0.0461	0.153 ± 0.0577 ± 0.0146	0.103	0.11	0.348	1.23
G304.10−0.24	4.31	3.85 ± 0.603 ± 2.09	3.35 ± 0.712 ± 0.763	4.92 ± 1.06 ± 0.202	7.6 ± 1.85 ± 0.287	4.43	6.89 ± 5.31 ± 0.566
G315.78−0.23	2.62 ± 0.57 ± 1.71 ± 1.76	1.32 ± 0.371 ± 0.588	0.499 ± 0.287 ± 0.121	0.247	1.07	2.03	4.93
G318.90+0.40	0.710	1.15 ± 0.235 ± 0.214	0.591 ± 0.169 ± 0.126	$0.128 \pm 0.117 \pm 1.12 \times 10^{-6}$	0.41	0.924	1.26
G326.12−1.81	1.44	1.57 ± 0.319 ± 0.491	1.82 ± 0.396 ± 0.195	1.96 ± 0.587 ± 0.152	1.48 ± 0.728 ± 0.11	3.45	4.41
G327.15−1.04	2.26	0.995 ± 0.223 ± 0.739	0.31 ± 0.151 ± 0.115	0.223 ± 0.146 ± 0.0322	0.229	0.421	1.21
G328.40+0.20	20.9 ± 1.03 ± 3.1 ± 4.53	21.6 ± 1.13 ± 3.03	17.0 ± 1.45 ± 1.8	14.0 ± 1.95 ± 1.18	12.4 ± 2.8 ± 1.07	9.8	7.48
G332.50−0.30	12.8 ± 0.989 ± 2.97 ± 2.2	12.5 ± 0.958 ± 1.32	12.3 ± 1.19 ± 0.978	13.1 ± 1.74 ± 0.578	15.1 ± 2.83 ± 1.02	13.1 ± 4.8 ± 2.09	16.8 ± 8.52 ± 1.46
G332.50−0.28	…	…	…	…	…	…	…
G336.40+0.10	5.86 ± 0.89 ± 2.67 ± 1.79	6.63 ± 0.796 ± 0.894	4.96 ± 0.888 ± 0.621	2.31 ± 1.1 ± 0.559	7.51 ± 2.19 ± 0.551	12.1 ± 4.5 ± 0.748	13.3
G337.20+0.10	4.85	2.29 ± 0.68 ± 0.16	0.888 ± 0.505 ± 0.0871	1.1 ± 0.545 ± 0.0508	1.48	1.61	14.0
G337.50−0.10	7.13 ± 0.904 ± 2.71 ± 1.92	3.27 ± 0.658 ± 0.88	1.69 ± 0.517 ± 0.189	0.981	0.693	3.06	5.24
G338.20−0.00	4.07	2.49 ± 0.643 ± 0.668	3.19 ± 0.576 ± 0.215	2.63 ± 0.685 ± 0.0969	6.42 ± 1.57 ± 0.222	8.19 ± 3.22 ± 0.415	5.68

Notes. All flux values are in units 10^{-6} MeV cm^{-2} s^{-1}. The first quoted error is the 1σ statistical error, the second error reflects the factor ∼3 of the statistical error for the lowest energy bin, and the latter is the total systematic error. Flux values that lack quoted errors are instead the 95% upper-limit flux for that bin.

[a] Corresponds to 4FGL J1810.3–1925e, a candidate extended source in the 4FGL catalogs that is reported with three flags related to the source flux changing significantly when changing the diffuse model or analysis method. For this reason, we do not provide systematic errors, as the method becomes unreliable for this source.

Table C2

The 95% Upper Limit to the Spectral Flux $E^2\frac{dN}{dE}$ per Bin for Nine Logarithmically Spaced Energy Bins for the 19 PWNe with No Source Detection (Table 6)

PWN Name	$E = 477$ MeV	$E = 1, 205$ MeV	$E = 3, 044$ MeV	$E = 7, 690$ MeV	$E = 19, 429$ MeV	$E = 49, 086$ MeV	$E = 124, 017$ MeV	$E = 313, 325$ MeV	$E = 791, 608$ MeV
G0.87+0.08	2.84×10^{-7}	7.12×10^{-7}	1.59×10^{-6}	5.79×10^{-7}	2.44×10^{-7}	8.08×10^{-7}	1.65×10^{-6}	3.32×10^{-6}	4.33×10^{-6}
G23.50+0.10	3.89×10^{-6}	3.07×10^{-6}	1.63×10^{-6}	1.46×10^{-6}	3.93×10^{-7}	9.18×10^{-7}	1.10×10^{-6}	1.71×10^{-6}	2.71×10^{-6}
G32.64+0.53	8.87×10^{-7}	1.18×10^{-6}	7.53×10^{-7}	5.30×10^{-7}	1.16×10^{-6}	1.27×10^{-6}	4.51×10^{-7}	9.62×10^{-7}	3.79×10^{-6}
G34.56–0.50	4.31×10^{-6}	2.81×10^{-6}	2.55×10^{-6}	3.03×10^{-6}	7.56×10^{-7}	2.06×10^{-6}	1.59×10^{-6}	4.19×10^{-6}	1.09×10^{-5}
G47.38–3.88	4.60×10^{-7}	3.94×10^{-7}	4.12×10^{-7}	1.44×10^{-7}	3.95×10^{-7}	1.65×10^{-7}	4.61×10^{-7}	9.0×10^{-7}	2.45×10^{-6}
G74.00–8.50	1.13×10^{-7}	2.06×10^{-7}	2.16×10^{-7}	4.00×10^{-7}	2.43×10^{-7}	5.82×10^{-7}	1.48×10^{-6}	3.943×10^{-6}	1.02×10^{-5}
G93.3+6.90	2.85×10^{-7}	4.05×10^{-7}	2.41×10^{-7}	3.62×10^{-7}	2.57×10^{-7}	1.54×10^{-7}	8.51×10^{-7}	7.49×10^{-7}	2.03×10^{-6}
G108.60+6.80	5.80×10^{-7}	2.77×10^{-7}	8.44×10^{-8}	7.65×10^{-8}	1.29×10^{-7}	3.93×10^{-7}	2.67×10^{-7}	7.35×10^{-7}	1.82×10^{-6}
G141.2+5.00	4.40×10^{-7}	3.03×10^{-7}	5.70×10^{-8}	8.61×10^{-8}	1.55×10^{-7}	1.32×10^{-7}	3.13×10^{-7}	7.0×10^{-7}	1.84×10^{-6}
G179.72–1.69	1.27×10^{-6}	3.43×10^{-7}	1.05×10^{-7}	7.50×10^{-8}	2.35×10^{-7}	6.76×10^{-7}	4.03×10^{-7}	1.00×10^{-6}	2.53×10^{-6}
G189.10+3.00	4.68×10^{-7}	3.82×10^{-6}	1.20×10^{-6}	1.60×10^{-6}	1.95×10^{-6}	2.31×10^{-6}	1.43×10^{-6}	4.29×10^{-6}	2.70×10^{-6}
G266.97–1.00	1.18×10^{-6}	1.12×10^{-6}	2.93×10^{-7}	2.32×10^{-7}	2.60×10^{-7}	2.01×10^{-7}	9.11×10^{-7}	2.98×10^{-6}	8.93×10^{-6}
G290.00–0.93	6.49×10^{-7}	4.83×10^{-7}	4.93×10^{-7}	1.11×10^{-7}	2.44×10^{-7}	8.61×10^{-7}	3.22×10^{-7}	9.64×10^{-7}	2.24×10^{-6}
G310.60–1.60	1.28×10^{-7}	4.75×10^{-8}	5.32×10^{-8}	9.87×10^{-8}	3.30×10^{-7}	3.38×10^{-7}	1.11×10^{-6}	9.03×10^{-7}	2.13×10^{-6}
G322.50–0.10	1.95×10^{-6}	9.32×10^{-7}	5.91×10^{-7}	5.45×10^{-7}	1.53×10^{-7}	2.70×10^{-7}	3.46×10^{-7}	1.16×10^{-6}	2.20×10^{-6}
G341.20+0.90	4.44×10^{-7}	2.85×10^{-7}	1.61×10^{-7}	1.73×10^{-7}	1.62×10^{-7}	2.70×10^{-7}	8.44×10^{-7}	1.03×10^{-6}	2.43×10^{-6}
G350.20–0.80	1.90×10^{-6}	1.13×10^{-6}	8.65×10^{-7}	7.39×10^{-7}	5.73×10^{-7}	5.49×10^{-7}	6.94×10^{-7}	1.01×10^{-6}	2.40×10^{-6}
G358.29+0.24	1.01×10^{-6}	8.49×10^{-7}	6.52×10^{-7}	6.77×10^{-7}	3.69×10^{-7}	4.37×10^{-7}	8.43×10^{-7}	9.51×10^{-7}	2.58×10^{-6}
G358.60–17.20	1.02×10^{-7}	7.12×10^{-8}	5.21×10^{-8}	7.15×10^{-8}	2.11×10^{-7}	2.06×10^{-7}	3.58×10^{-7}	9.57×10^{-7}	2.48×10^{-6}

Note. All flux values are in units MeV cm^{-2} s^{-1}.

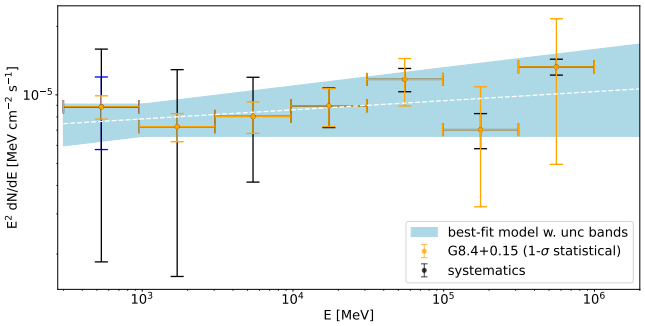

Figure C1. 300 MeV–1 TeV SED for PWN G8.40+0.15, corresponding to 4FGL J1804.7–2144e. The complete figure set of all 36 SEDs is provided in the online journal.

(The complete figure set (36 images) is available in the online article.)

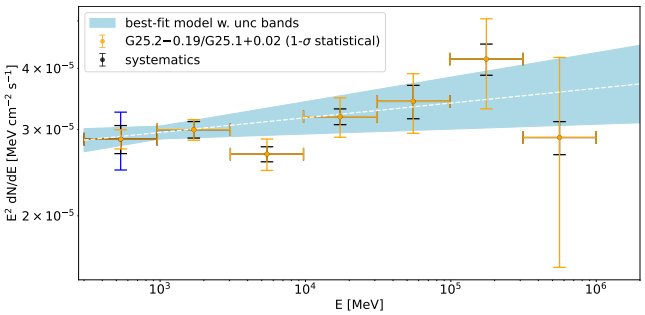

Figure C2. 300 MeV–1 TeV SED for TeV PWN HESS J1837–069, corresponding to 4FGL J1836.5–0651e. Two lower-energy PWN counterparts G25.24–0.19 and G25.10+0.02 coincide with the extended Fermi source. The complete figure set of all 36 SEDs is provided in the online journal.

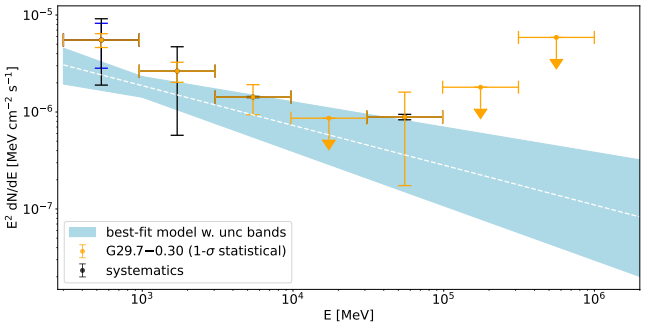

Figure C3. 300 MeV–1 TeV SED for PWN Kes 75 (G29.70–0.30). The complete figure set of all 36 SEDs is provided in the online journal.

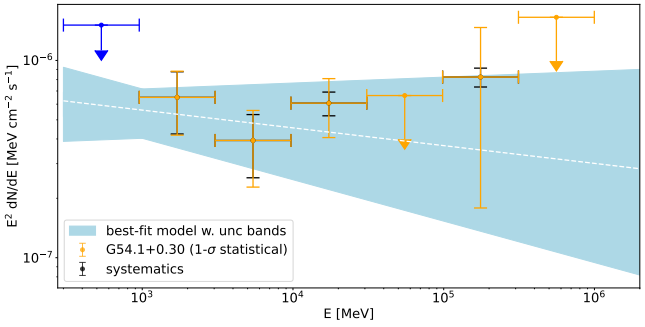

Figure C4. 300 MeV–1 TeV SED for PWN G54.10+0.27, corresponding to 4FGL J1930.5+1853 in 4FGL–DR3. The complete figure set of all 36 SEDs is provided in the online journal.

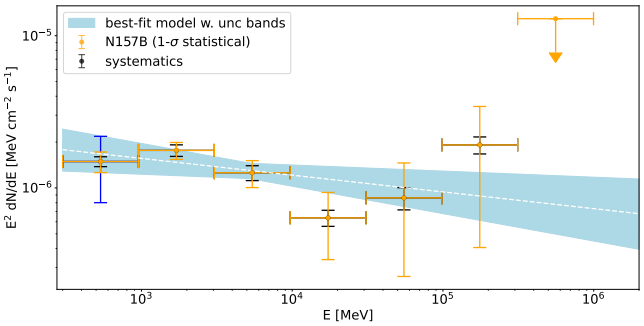

Figure C5. 300 MeV–1 TeV SED for PWN N 157B, corresponding to 4FGL J0537.8–6909. The complete figure set of all 36 SEDs is provided in the online journal.

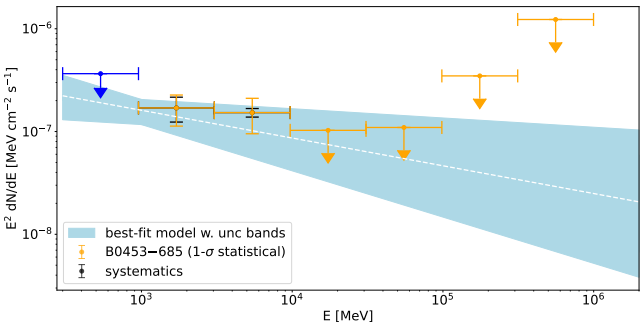

Figure C6. 300 MeV–1 TeV SED for PWN B0453–685. The complete figure set of all 36 SEDs is provided in the online journal.

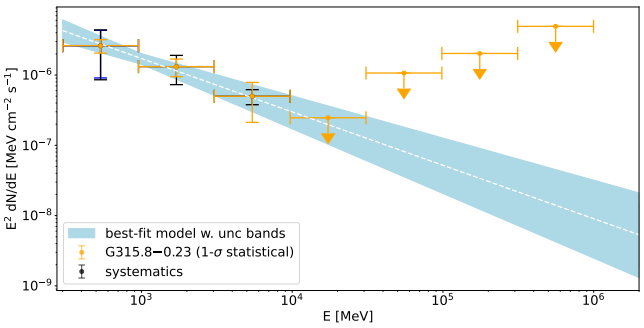

Figure C7. 300 MeV–1 TeV SED for PWN G315.78–0.23 (the Frying Pan), corresponding to 4FGL J1435.8–6018. The complete figure set of all 36 SEDs is provided in the online journal.

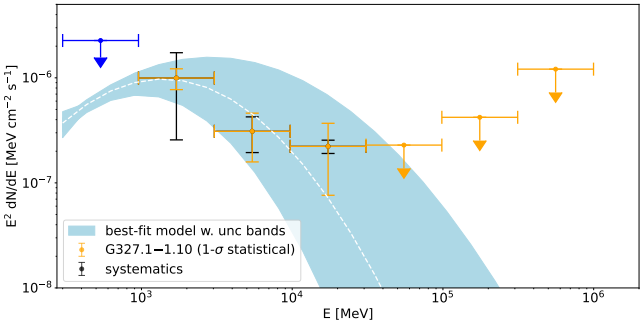

Figure C8. 300 MeV–1 TeV SED for PWN G327.15–1.04, corresponding to 4FGL J1554.4–5506 in 4FGL–DR3. The complete figure set of all 36 SEDs is provided in the online journal.

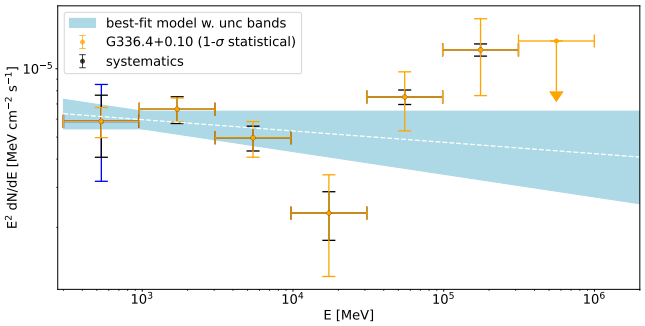

Figure C9. 300 MeV–1 TeV SED for PWN G336.40+0.10, corresponding to 4FGL J1631.6–4756e. The complete figure set of all 36 SEDs is provided in the online journal.

ORCID iDs

A. Acharyya https://orcid.org/0000-0002-2028-9230
M. Ajello https://orcid.org/0000-0002-6584-1703
L. Baldini https://orcid.org/0000-0002-9785-7726
J. Ballet https://orcid.org/0000-0002-8784-2977
C. Bartolini https://orcid.org/0000-0001-7233-9546
J. Becerra Gonzalez https://orcid.org/0000-0002-6729-9022
R. Bellazzini https://orcid.org/0000-0002-2469-7063
E. Bissaldi https://orcid.org/0000-0001-9935-8106
R. Bonino https://orcid.org/0000-0002-4264-1215
P. Bruel https://orcid.org/0000-0002-9032-7941
R. A. Cameron https://orcid.org/0000-0003-0942-2747
P. A. Caraveo https://orcid.org/0000-0003-2478-8018
F. Casaburo https://orcid.org/0000-0002-2260-9322
D. Castro https://orcid.org/0000-0002-0394-3173
E. Cavazzuti https://orcid.org/0000-0001-7150-9638
S. Ciprini https://orcid.org/0000-0002-0712-2479
G. Cozzolongo https://orcid.org/0009-0001-3324-0292
P. Cristarella Orestano https://orcid.org/0000-0003-3219-608X
S. Cutini https://orcid.org/0000-0002-1271-2924
F. D'Ammando https://orcid.org/0000-0001-7618-7527
N. Di Lalla https://orcid.org/0000-0002-7574-1298
L. Di Venere https://orcid.org/0000-0003-0703-824X
A. Domínguez https://orcid.org/0000-0002-3433-4610
J. Eagle https://orcid.org/0000-0001-9633-3165
A. Fiori https://orcid.org/0000-0003-3174-0688
Y. Fukazawa https://orcid.org/0000-0002-0921-8837
S. Funk https://orcid.org/0000-0002-2012-0080
P. Fusco https://orcid.org/0000-0002-9383-2425
F. Gargano https://orcid.org/0000-0002-5055-6395
C. Gasbarra https://orcid.org/0000-0001-8335-9614
D. Gasparrini https://orcid.org/0000-0002-5064-9495
S. Germani https://orcid.org/0000-0002-2233-6811
F. Giacchino https://orcid.org/0000-0002-0247-6884
N. Giglietto https://orcid.org/0000-0002-9021-2888
M. Giliberti https://orcid.org/0009-0007-2835-2963
F. Giordano https://orcid.org/0000-0002-8651-2394
M. Giroletti https://orcid.org/0000-0002-8657-8852
D. Green https://orcid.org/0000-0003-0768-2203
I. A. Grenier https://orcid.org/0000-0003-3274-674X
M.-H. Grondin https://orcid.org/0000-0002-8383-251X
S. Guiriec https://orcid.org/0000-0001-5780-8770
R. Gupta https://orcid.org/0000-0003-4905-7801
M. Hashizume https://orcid.org/0009-0003-4534-9361
E. Hays https://orcid.org/0000-0002-8172-593X
J. W. Hewitt https://orcid.org/0000-0002-4064-6346
D. Horan https://orcid.org/0000-0001-5574-2579
X. Hou https://orcid.org/0000-0003-0933-6101
T. Kayanoki https://orcid.org/0000-0002-6960-9274
M. Kuss https://orcid.org/0000-0003-1212-9998
A. Laviron https://orcid.org/0000-0003-1521-7950
M. Lemoine-Goumard https://orcid.org/0000-0002-4462-3686
A. Liguori https://orcid.org/0009-0001-4240-6362
J. Li https://orcid.org/0000-0003-1720-9727
I. Liodakis https://orcid.org/0000-0001-9200-4006
P. Loizzo https://orcid.org/0000-0002-2404-760X
F. Longo https://orcid.org/0000-0003-2501-2270
F. Loparco https://orcid.org/0000-0002-1173-5673
L. Lorusso https://orcid.org/0000-0002-2549-4401
M. N. Lovellette https://orcid.org/0000-0002-0332-5113
P. Lubrano https://orcid.org/0000-0003-0221-4806
S. Maldera https://orcid.org/0000-0002-0698-4421
D. Malyshev https://orcid.org/0000-0002-9102-4854
G. Martí-Devesa https://orcid.org/0000-0003-0766-6473
M. N. Mazziotta https://orcid.org/0000-0001-9325-4672
I. Mereu https://orcid.org/0000-0003-0219-4534
P. F. Michelson https://orcid.org/0000-0002-1321-5620
N. Mirabal https://orcid.org/0000-0002-7021-5838
T. Mizuno https://orcid.org/0000-0001-7263-0296
P. Monti-Guarnieri https://orcid.org/0000-0002-1434-1282
M. E. Monzani https://orcid.org/0000-0002-8254-5308
A. Morselli https://orcid.org/0000-0002-7704-9553
I. V. Moskalenko https://orcid.org/0000-0001-6141-458X
N. Omodei https://orcid.org/0000-0002-5448-7577
E. Orlando https://orcid.org/0000-0001-6406-9910
D. Paneque https://orcid.org/0000-0002-2830-0502
G. Panzarini https://orcid.org/0000-0002-2586-1021
M. Persic https://orcid.org/0000-0003-1853-4900
M. Pesce-Rollins https://orcid.org/0000-0003-1790-8018
R. Pillera https://orcid.org/0000-0003-3808-963X
T. A. Porter https://orcid.org/0000-0002-2621-4440
G. Principe https://orcid.org/0000-0003-0406-7387
S. Rainò https://orcid.org/0000-0002-9181-0345
R. Rando https://orcid.org/0000-0001-6992-818X
M. Razzano https://orcid.org/0000-0003-4825-1629
A. Reimer https://orcid.org/0000-0001-8604-7077
O. Reimer https://orcid.org/0000-0001-6953-1385
M. Sánchez-Conde https://orcid.org/0000-0002-3849-9164
P. M. Saz Parkinson https://orcid.org/0000-0001-6566-1246
D. Serini https://orcid.org/0000-0002-9754-6530
C. Sgrò https://orcid.org/0000-0001-5676-6214
E. J. Siskind https://orcid.org/0000-0002-2872-2553
G. Spandre https://orcid.org/0000-0003-0802-3453
P. Spinelli https://orcid.org/0000-0001-6688-8864
A. W. Strong https://orcid.org/0000-0003-3799-5489
H. Tajima https://orcid.org/0000-0002-1721-7252
J. B. Thayer https://orcid.org/0000-0002-9051-1677
L. Tibaldo https://orcid.org/0000-0001-7523-570X
D. F. Torres https://orcid.org/0000-0002-1522-9065
J. Valverde https://orcid.org/0000-0002-8090-6528
K. Wood https://orcid.org/0000-0002-7376-3151
G. Zaharijas https://orcid.org/0000-0001-8484-7791
W. Zhang https://orcid.org/0000-0003-2839-1325

References

Abdo, A. A., Ackermann, M., Ajello, M., et al. 2009, ApJL, 706, L1
Abdo, A. A., Ajello, M., Allafort, A., et al. 2013, ApJS, 208, 17
Abdollahi, S., Acero, F., Ackermann, M., et al. 2020, ApJS, 247, 33
Abdollahi, S., Acero, F., Baldini, L., et al. 2022, ApJS, 260, 53
Abeysekara, A. U., Albert, A., Alfaro, R., et al. 2017, ApJ, 843, 40
Abeysekara, A. U., Archer, A., Benbow, W., et al. 2018, ApJ, 866, 24
Acero, F., Gallant, Y., Ballet, J., Renaud, M., & Terrier, R. 2013a, A&A, 551, A7
Acero, F., Ackermann, M., Ajello, M., et al. 2013b, ApJ, 773, 77
Acero, F., Ackermann, M., Ajello, M., et al. 2016, ApJS, 224, 8
Ackermann, M., Ajello, M., Baldini, L., et al. 2011, ApJ, 726, 35
Ackermann, M., Ajello, M., Baldini, L., et al. 2017, ApJ, 843, 139
Ackermann, M., Albert, A., Atwood, W. B., et al. 2016, A&A, 586, A71
Aharonian, F., Akhperjanian, A. G., Aye, K. M., et al. 2005, Sci, 307, 1938
Aharonian, F., Akhperjanian, A. G., Bazer-Bachi, A. R., et al. 2006, ApJ, 636, 777
Aharonian, F., Akhperjanian, A. G., Barres de Almeida, U., et al. 2008, A&A, 477, 353
Aleksić, J., Alvarez, E. A., Antonelli, L. A., et al. 2012, A&A, 541, A13
Aliu, E., Aune, T., Behera, B., et al. 2014, ApJ, 788, 78
Araya, M. 2018, ApJ, 859, 69
Arribas, M. P., Schwanke, U., Sushch, I., et al. 2012, ICRC (Beijing), 7, 140
Atwood, W. B., Baldini, L., Bregeon, J., et al. 2013, ApJ, 774, 76
Balbo, M., Saouter, P., Walter, R., et al. 2010, A&A, 520, A111
Ballet, J., Bruel, P., Burnett, T. H., Lott, B. & The Fermi-LAT collaboration 2023, arXiv:2307.12546
Ballet, J., Burnett, T. H., Digel, S. W., & Lott, B. 2020, arXiv:2005.11208
Bandiera, R., Bucciantini, N., Martín, J., Olmi, B., & Torres, D. F. 2023a, MNRAS, 520, 2451
Bandiera, R., Bucciantini, N., Olmi, B., & Torres, D. F. 2023b, MNRAS, 525, 2839
Becker, R. H., & Helfand, D. J. 1985, ApJL, 297, L25
Becker, R. H., & Helfand, D. J. 1987, ApJ, 316, 660
Blondin, J. M., Chevalier, R. A., & Frierson, D. M. 2001, ApJ, 563, 806
Brogan, C. L., Devine, K. E., Lazio, T. J., et al. 2004, AJ, 127, 355
Brogan, C. L., Gaensler, B. M., Gelfand, J. D., et al. 2005, ApJL, 629, L105
Bruel, P., Burnett, T. H., Digel, S. W., et al. 2018, arXiv:1810.11394
Camilo, F., Lorimer, D. R., Bhat, N. D. R., et al. 2002, ApJL, 574, L71
Cao, Z., Aharonian, F., An, Q., et al. 2024, ApJS, 271, 25
Chen, Y., Wang, Q. D., Gotthelf, E. V., et al. 2006, ApJ, 651, 237
Clark, D. H., McCrea, W. H., & Stephenson, F. R. 1977, Natur, 265, 318
Coerver, A., Wilcox, P., Zhang, H., et al. 2019, ApJ, 878, 126
Combi, J. A., Albacete Colombo, J. F., Romero, G. E., & Benaglia, P. 2006, ApJL, 653, L41
de Palma, F., Brandt, T. J., Johannesson, G., & Tibaldo, L. 2013, arXiv:1304.1395
Devin, J., Acero, F., Ballet, J., & Schmid, J. 2018, A&A, 617, A5
Donath, A., Siemiginowska, A., Kashyap, V. L., van Dyk, D. A., & Burke, D. 2024, AJ, 168, 182
Dormody, M., Johnson, R. P., Atwood, W. B., et al. 2011, ApJ, 742, 126
Eagle, J., Castro, D., Mahhov, P., et al. 2023, ApJ, 945, 4
Eagle, J., Castro, D., Temim, T., et al. 2022, ApJ, 940, 143
Feinstein, F., Fiasson, A., Gallant, Y., et al. 2009, in AIP Conf. Ser. 1112, Science with the New Generation of High Energy Gamma-ray Experiments, ed. D. Bastieri & R. Rando (Melville, NY: AIP), 54
Fermi Science Support Development Team, 2019 Fermitools: Fermi Science Tools, Astrophysics Source Code Library, ascl:1905.011
Ferrand, G., & Safi-Harb, S. 2012, AdSpR, 49, 1313
Frank, K. A., Burrows, D. N., & Park, S. 2015, ApJ, 810, 113
Fujita, Y., Nakanishi, H., Muller, E., et al. 2014, PASJ, 66, 19
Gaensler, B. M., Dickel, J. R., & Green, A. J. 2000, ApJ, 542, 380
Gaensler, B. M., Hendrick, S. P., Reynolds, S. P., & Borkowski, K. J. 2003, ApJL, 594, L111
Gaensler, B. M., & Slane, P. O. 2006, ARA&A, 44, 17
Gelfand, J. D., Gaensler, B. M., Slane, P. O., et al. 2007, ApJ, 663, 468
Gelfand, J. D., Slane, P. O., & Temim, T. 2015, ApJ, 807, 30
Gelfand, J. D., Slane, P. O., & Zhang, W. 2009, ApJ, 703, 2051
Gotthelf, E. V., & Halpern, J. P. 2008, ApJ, 681, 515
Green, D. A. 2019, JApA, 40, 36
Grondin, M. H., Funk, S., Lemoine-Goumard, M., et al. 2011, ApJ, 738, 42
Guest, B., Safi-Harb, S., MacMaster, A., et al. 2020, MNRAS, 491, 3013
H. E. S. S. Collaboration, Abdalla, H., Abramowski, A., et al. 2018, A&A, 612, A1
H. E. S. S. Collaboration, Abramowski, A., Acero, F., et al. 2012a, A&A, 548, A46
H. E. S. S. Collaboration, Abramowski, A., Acero, F., et al. 2012b, A&A, 545, L2
H. E. S. S. Collaboration, Abramowski, A., Aharonian, F., et al. 2014, A&A, 562, A40
Halpern, J. P., Tomsick, J. A., Gotthelf, E. V., et al. 2014, ApJL, 795, L27
Jakobsen, S. J., Tomsick, J. A., Watson, D., Gotthelf, E. V., & Kaspi, V. M. 2014, ApJ, 787, 129
Jogler, T., & Funk, S. 2016, ApJ, 816, 100
Joshi, Y. C., Maurya, J., John, A. A., et al. 2023, yCat, 492, 3602
Kargaltsev, O., Pavlov, G. G., & Garmire, G. P. 2007, ApJ, 670, 643
Kargaltsev, O., Pavlov, G. G., & Wong, J. A. 2009, ApJ, 690, 891
Kargaltsev, O., Rangelov, B., & Pavlov, G. G. 2013, in The Universe Evolution: Astrophysical and Nuclear Aspects, ed. I. Strakovsky & L. Blokhintsev (New York: Nova Science Publishers)
Kargaltsev, O., Schmitt, B. M., Pavlov, G. G., & Misanovic, Z. 2012, ApJ, 745, 99
Katagiri, H., Tibaldo, L., Ballet, J., et al. 2011, ApJ, 741, 44
Katsuta, J., Uchiyama, Y., & Funk, S. 2017, ApJ, 839, 129
Kennel, C. F., & Coroniti, F. V. 1984, ApJ, 283, 710
Koo, B.-C., Lee, J.-J., Seward, F. D., & Moon, D.-S. 2005, ApJ, 633, 946
Kuiper, L., Hermsen, W., & Dekker, A. 2018, MNRAS, 475, 1238
Lande, J., Ackermann, M., Allafort, A., et al. 2012, ApJ, 756, 5
Leahy, D. A. 2004, AJ, 127, 2277
Li, J., Torres, D. F., Lin, T. T., et al. 2018, ApJ, 858, 84
Linden, T., Auchettl, K., Bramante, J., et al. 2017, PhRvD, 96, 103016
Liu, B., Yang, R.-z., Sun, X.-n., Aharonian, F., & Chen, Y. 2019, ApJ, 881, 94
Liu, Q.-C., Chen, Y., Chen, B.-Q., et al. 2018, ApJ, 859, 173
Liu, Q.-C., Zhong, W.-J., Chen, Y., et al. 2024, MNRAS, 528, 6761
Livingstone, M. A., Ng, C. Y., Kaspi, V. M., Gavriil, F. P., & Gotthelf, E. V. 2011, ApJ, 730, 66
Madsen, K. K., Fryer, C. L., Grefenstette, B. W., et al. 2020, ApJ, 889, 23
MAGIC Collaboration, Acciari, V. A., Ansoldi, S., et al. 2019, MNRAS, 483, 4578
Malyshev, D., Cholis, I., & Gelfand, J. 2009, PhRvD, 80, 063005
Manchester, R. N., Hobbs, G. B., Teoh, A., & Hobbs, M. 2005, AJ, 129, 1993
Marchesi, S., Eagle, J., Ajello, M., et al. 2024, ApJ, 964, 132
Mares, A., Lemoine-Goumard, M., Acero, F., et al. 2021, ApJ, 912, 158
Marshall, F. E., Gotthelf, E. V., Middleditch, J., Wang, Q. D., & Zhang, W. 2004, ApJ, 603, 682
Martin, J., & Torres, D. F. 2022, JHEAp, 36, 128
Martín, J., Torres, D. F., & Rea, N. 2012, MNRAS, 427, 415
Matheson, H., Safi-Harb, S., & Kothes, R. 2016, ApJ, 825, 134
Mattana, F., Falanga, M., Götz, D., et al. 2009, ApJ, 694, 12
Mattox, J. R., Bertsch, D. L., Chiang, J., et al. 1996, ApJ, 461, 396
Ng, C. Y., Bucciantini, N., Gaensler, B. M., et al. 2012, ApJ, 746, 105
Nolan, P. L., Abdo, A. A., Ackermann, M., et al. 2012, ApJS, 199, 31
Petriella, A. 2019, A&A, 626, A65
Petriella, A., Paron, S. A., & Giacani, E. B. 2013, A&A, 554, A73
Principe, G., Mitchell, A. M. W., Caroff, S., et al. 2020, A&A, 640, A76
Ranasinghe, S., & Leahy, D. 2022, ApJ, 940, 63
Rees, M. J., & Gunn, J. E. 1974, MNRAS, 167, 1
Renaud, M. 2009, arXiv:0905.1287
Reynolds, S. P., Borkowski, K. J., & Gwynne, P. H. 2018, ApJ, 856, 133
Reynolds, S. P., & Chevalier, R. A. 1984, ApJ, 278, 630
Roberts, M. S. E. 2004, The Pulsar Wind Nebula Catalog (March 2005 version) (Quebec: McGill Univ.)
Saito, S., Khangulyan, D., Hagiwara, K., & Uchiyama, Y. 2017, in AIP Conf. Ser. 1792, 6th Int. Symp. High Energy Gamma-Ray Astronomy (Melville, NY: AIP), 040013
Sasaki, M., Heinitz, C., Warth, G., & Pühlhofer, G. 2014, A&A, 563, A9
Slane, P. 2017, in Handbook of Supernovae, ed. A. W. Alsabti & P. Murdin (Berlin: Springer), 2159
Smith, D. A., Abdollahi, S., Ajello, M., et al. 2023, ApJ, 958, 191
Straal, S. M., Gelfand, J. D., & Eagle, J. L. 2023, ApJ, 942, 103
Su, H.-Q., Zhang, M.-F., Zhu, H., & Wu, D. 2017, RAA, 17, 109
Supan, L., Castelletti, G., Joshi, B. C., Surnis, M. P., & Supanitsky, D. 2015, A&A, 576, A81
Temim, T., Slane, P., Kolb, C., et al. 2015, ApJ, 808, 100
Temim, T., Slane, P., Reynolds, S. P., Raymond, J. C., & Borkowski, K. J. 2010, ApJ, 710, 309
Tibaldo, L., Zanin, R., Faggioli, G., et al. 2018, A&A, 617, A78
Torres, D. 2017, ASSL, 446
Torres, D. F., Cillis, A., Martìn, J., & de Oña Wilhelmi, E. 2014, JHEAp, 1, 31

Tüllmann, R., Plucinsky, P. P., Gaetz, T. J., et al. 2010, ApJ, 720, 848
Tutone, A., Ballet, J., Acero, F., D'Aì, A., & Cusumano, G. 2021, A&A, 656, A139
van der Swaluw, E., Downes, T. P., & Keegan, R. 2004, A&A, 420, 937
Wach, T., Mitchell, A. M. W., Joshi, V., & Funk, S. 2023, arXiv:2308.16717
Wakely, S. P., & Horan, D. 2008, ICRC (Yucatán), 3, 1341
Wood, M., Caputo, R., Charles, E., et al. 2017, ICRC (Busan), 35, 824
Xiang, Y., Xing, Y., & Jiang, Z. 2021, ApJ, 912, 117
Zhang, S., Tang, X., Zhang, X., et al. 2018, ApJ, 859, 141
Zhang, W., Torres, D. F., Garcìa, C. R., Li, J., & Mestre, E. 2024, A&A, 691, A332
Zheng, D., Wang, Z., Zhang, X., Chen, Y., & Xing, Y. 2023, ApJ, 952, 158